

# Brillouin scattering in high-power narrow-linewidth fiber amplifiers

Von der Fakultät für Mathematik und Physik  
der Gottfried Wilhelm Leibniz Universität Hannover  
zur Erlangung des Grades

**Doktor der Naturwissenschaften**

– Dr. rer. nat. –

genehmigte Dissertation

von

**M.Sc., Dipl.-Ing. (FH) Matthias Hildebrandt**

geboren am 19.05.1977 in Hannover

2009

Referent: Prof. Dr. Uwe Morgner, Leibniz Universität Hannover

Korreferent: Prof. Dr. Boris N. Chichkov, Leibniz Universität Hannover

Tag der Promotion: 26.06.2009

# Kurzfassung

Laserquellen mit Ytterbium dotierten Fasern als aktivem Medium zählen zu den effizientesten und leistungsstärksten Systemen in der heutigen Lasertechnik. Durch die große Oberfläche und Länge der Fasern und den Betrieb mit geringen Quantendefekten werden leistungslimitierende thermale Effekte minimiert und hohe Ausgangsleistungen mit beugungsbegrenzter Strahlqualität erreicht. Hohe Strahlintensitäten im Kern der Faser ermöglichen einen effizienten Laserbetrieb mit hohen Verstärkungsfaktoren. Relativ kleine Kerndurchmesser und große Längen der Fasern haben jedoch zur Folge, dass nichtlineare Effekte auftreten. Bei der Verstärkung schmalbandiger Laserquellen ist die stimulierte Brillouin-Streuung (SBS) der wesentliche limitierende Prozess. Für die Skalierung der Ausgangsleistung und der damit notwendigen Unterdrückung von SBS wurden in dieser Arbeit experimentelle und theoretische Untersuchungen zur Entwicklung von Brillouin-Streuung in faserbasierten Hochleistungsverstärkern durchgeführt.

In verschiedenen Verstärkerexperimenten wurde Brillouin-Streuung und die Einflüsse auf den Verstärkerbetrieb in Ytterbium dotierten Fasern untersucht. Als Signalquelle diente ein nicht-planarer Ring-Oszillator (NPRO), der schmalbandiges Licht bei einer Wellenlänge von 1064 nm mit 2 W Ausgangsleistung emittiert. Nach der Verstärkung durch aktive Fasern wurden Ausgangsleistungen bis 148 W bei nahezu beugungsbegrenzter Strahlqualität und linearer Polarisation erreicht. Dabei wurde neben einer herkömmlichen Stufenindexfaser erstmalig eine photonische Kristallfaser (PCF) für diese Anwendung untersucht.

Aufgrund der schmalbandigen Emission der Brillouin Streuung von nur einigen MHz Bandbreite, wurden für die spektrale Untersuchung zwei hochauflösende Messverfahren verwendet. Damit konnten erstmals neben der aus stimulierter Streuung und Verstärkung resultierenden spektralen Veränderung andere Einflüsse wie Temperatur und Spannung in Faserverstärkern mit hoher Ausgangsleistung charakterisiert werden. Der Einfluss thermischer Gradienten auf das Brillouin Spektrum stellt in Verstärkern mit hoher Ausgangsleistung einen wichtigen Effekt dar und wird zur aktiven Unterdrückung der SBS eingesetzt. Die in den experimentellen Untersuchungen gewonnenen Erkenntnisse wurden zur Optimierung eines auf Ratengleichungen basierenden, numerischen Modells eingesetzt.

Mit dem numerischen Modell wurden die experimentellen Daten der optischen Leistung und spektralen Entwicklung der Brillouin Streuung rekonstruiert und seine Gültigkeit in verschiedenen Verstärkerkonfigurationen verifiziert. Damit ist eine Vorhersage der Schwelle für SBS und die Konzeption vergleichbarer Verstärkersysteme weit höherer Ausgangsleistung für schmalbandige Laserquellen möglich.

**Schlagwörter:** Laser, Faserverstärker, Brillouin Streuung



# Abstract

At present ytterbium doped fibers are one of the most efficient high-power laser gain media. The large surface and fiber length and low quantum defect operation minimize thermal effects that limit power scaling and high output power operation with diffraction limited beam qualities can be obtained. High signal intensities in the fiber core enable an efficient, saturated operation. Such high intensities and long fiber length result in nonlinear optical effects that limit the system power handling capacity. In narrow-bandwidth laser systems stimulated Brillouin scattering (SBS) is the most stringent process. In order to increase the optical power and hence mitigate SBS, experimental and theoretical investigations on the evolution of Brillouin scattering in high-power fiber amplifiers have been carried out in this work.

In different amplifier experiments with ytterbium doped fibers Brillouin scattering and its influences on the amplifier operation were investigated. A nonplanar ring-oscillator (NPRO) with a narrow-linewidth output power of 2 W at 1064 nm is amplified up to 148 W with nearly diffraction limited beam quality and linear polarization. Besides a conventional step-index fiber, for the first time a photonic crystal fiber (PCF) was utilized for this application.

Owing to the narrow bandwidth emission of Brillouin scattering of only a few MHz, two high-resolution detection methods have been developed. In this way gain narrowing processes as well as external influences on the spectral shape, such as temperature and strain, can be investigated. Thermal gradients can have a strong effect on the Brillouin gain spectrum in high-power amplifier systems and are applied to suppress SBS. The experimental data obtained from these investigations have been incorporated in a numerical model based on coupled rate-equations.

The numerical model is used to reproduce the experimentally observed optical power and spectral evolution of the fiber amplifier signals and Brillouin scattering and its validity is verified in different amplifier configurations. With this model a prediction of the SBS threshold can be made and design concepts for narrow-linewidth fiber amplifier systems with higher output power can be developed.

**Key words:** Laser, Fiber amplifier, Brillouin scattering



# Contents

<b>1</b>	<b>Introduction</b>	<b>9</b>
<b>2</b>	<b>Technical background</b>	<b>13</b>
2.1	Narrow-linewidth fiber amplifiers . . . . .	13
2.2	Detection of Brillouin scattering spectra . . . . .	16
<b>3</b>	<b>Theory</b>	<b>19</b>
3.1	Stimulated Brillouin scattering . . . . .	19
3.2	Numerical model . . . . .	27
<b>4</b>	<b>Fiber amplifier setup</b>	<b>35</b>
<b>5</b>	<b>Fiber amplifier characteristics</b>	<b>41</b>
5.1	Output power and efficiency . . . . .	41
5.2	Polarization . . . . .	44
5.3	Beam quality . . . . .	46
5.4	Optical spectrum . . . . .	49
5.4.1	Seed saturation . . . . .	50
5.4.2	ASE suppression . . . . .	51

---

<b>6 Brillouin scattering detection</b>	<b>55</b>
6.1 Pump-and-probe measurements . . . . .	55
6.2 Backscattered power . . . . .	60
6.3 Intensity noise . . . . .	64
6.4 Optical spectrum . . . . .	67
6.5 Heterodyne detection . . . . .	69
<b>7 SBS suppression</b>	<b>79</b>
7.1 Strain . . . . .	80
7.2 Temperature . . . . .	83
7.3 Glass composition and fiber design . . . . .	87
7.4 Large-core fibers . . . . .	88
<b>8 Summary</b>	<b>93</b>
<b>Bibliography</b>	<b>97</b>



# 1. Introduction

Narrow-linewidth laser sources have become more and more important in various fields of application. Most prominent applications are optical fiber communication networks [1], strain and temperature fiber-optic sensors [2, 3] and scientific areas of research such as cooling and trapping of atoms [4].

Stable narrow-linewidth laser emission is obtained from distributed feedback or external-cavity semiconductor lasers [5], ytterbium or erbium doped fiber lasers [6] and solid-state micro-chip [7] or non-planar ring oscillators (NPRO) [8]. Single-frequency operation with only one resonant longitudinal laser mode and a minimization of external and internal noise sources enables a laser operation with a linewidth of only a few kHz in free-running operation and even sub-Hz linewidth with active stabilization to high-finesse Fabry-Pérot reference cavities [9–11].

Some applications such as interferometers for gravitational-wave detection [12] or the formation of artificial guide-stars for telescopic imaging systems in astronomy science [13] require a large output power of several ten to hundreds of watts. Future generations of gravitational-wave detectors even aim for 1 kW of laser output power with nearly diffraction limited beam quality and linear polarization. These power levels with a stable single-frequency, low noise operation cannot be obtained directly from aforementioned laser oscillators [14]. Therefore, different amplification concepts have been developed in the past to scale the available output power while maintaining the required laser beam characteristics. These laser systems most commonly comprise solid-state lasers injection-locked to a narrow-linewidth master-oscillator [15]. Although high output power of up to 195 W have been demonstrated, such solid-state laser setups are quite complicated and inefficient. Further power scaling is difficult due to thermo-optical effects inducing aberrations and depolarization.

An alternative amplification scheme for narrow-linewidth laser sources using rare-earth doped fused silica fibers has been demonstrated with more than 400 W of output power [16]. In recent years these potentially compact and robust systems have gained much attention in the research field of coherent beam combining of several laser sources by an active phase control to reach output power levels with multiple kilowatts needed for heavy industry and military applications [17]. In fiber laser systems thermal limitations are greatly reduced owing to large fiber lengths and surface areas. However, long interaction lengths and small mode-field areas enhance nonlinear effects that prohibit scaling to larger output power. For narrow-linewidth signal amplification stimulated Brillouin scattering (SBS) becomes the dominant limitation. To some extent SBS can be suppressed by increasing the fiber core size and decreasing fiber length using highly doped large mode-area (LMA) fibers. Broadening of the Brillouin scattering spectrum by temperature and strain gradients or varying doping distributions along the fiber can further reduce the effective Brillouin gain. In high-power fiber amplifier systems particularly temperature gradients induced by absorbed pump light play an important role for the spectral evolution of Brillouin scattering spectra. Understanding and modeling spectral broadening mechanisms of Brillouin scattering is therefore essential for further increasing the output power of narrow-linewidth fiber amplifier systems.

Although great progress has been made to mitigate optical nonlinearities in optical fibers, SBS still represents the most stringent limitation in narrow-linewidth high-power fiber amplifier systems. For this reason this work is focused on the investigation of Brillouin scattering and its effect on the fiber amplifier operation. In different high-power ytterbium doped fiber amplifier configurations operated with up to 148 W of output power the evolution of the Brillouin scattering power and spectra is experimentally detected and theoretically described with a numerical model.

### **Organization of the thesis**

The outline of this thesis is as follows. Chapter 2 provides a general overview over the concept of high-power fiber amplifiers and shortly reviews research group activities in the field of narrow-linewidth fiber amplifier systems and detection techniques for Brillouin scattering. In Chapter 3 the theoretical background for Brillouin scattering in passive and active fibers is introduced with a numerical model based on coupled rate-equations describing the amplifier signal and pump light distributions including the growth of Brillouin scattering.

---

louis scattering. In Chapter 4 the fiber amplifier setup is presented. Chapters 5 and 6 describe results obtained from a high-power fiber amplifier operated with an ytterbium doped step-index and a photonic crystal fiber (PCF) in different amplifier pump configurations. In Chapter 5 general amplifier characteristics are addressed with the spectral, power, polarization and beam quality properties of the amplified signals. Chapter 6 contains the investigation of Brillouin scattering and its influences and limitations on the fiber amplifier operation. Brillouin scattering power and the spectral evolution is experimentally detected and compared with results obtained from numerical modeling including the thermally induced distortion of the Brillouin scattering spectra. In Chapter 7 different approaches for the suppression of SBS are presented and in some parts investigated with the developed experimental and theoretical tools giving directions for future work. Finally, Chapter 8 contains the summary and conclusion of the thesis.



## 2. Technical background

### 2.1 Narrow-linewidth fiber amplifiers

In the last decade rare-earth doped large mode-area (LMA) fibers have become an alternative to conventional solid-state laser crystals offering extremely efficient, high-power laser operation. These fibers are typically several meters long and consist of a fused silica cladding with diameters of a few hundred micrometers to guide pump light from low-brightness laser diodes and a doped core with typically  $10\text{-}30\ \mu\text{m}$  diameter to guide the laser radiation. Light guidance is obtained by total internal reflection with increasing coating, cladding and core refractive indices  $n_{\text{coa}} < n_{\text{cl}} < n_{\text{co}}$  (Fig. 2.1).

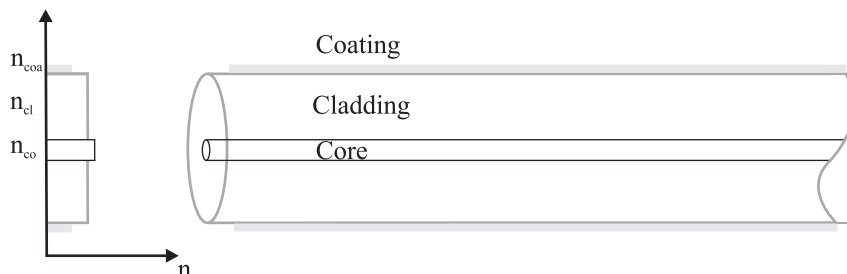


**Figure 2.1:** Large mode-area fiber design with refractive index profile.

This design allows for an efficient absorption of pump radiation, low heat generation and excellent laser beam quality. Most fiber lasers and amplifiers are doped with rare-earth ions such as erbium or erbium/ytterbium for telecommunication applications with emission wavelengths around 1300 nm and 1550 nm. For high-power laser systems preferably ytterbium doped fibers are being used owing to an operation with small quantum defects and consequently an efficient laser operation with low thermal loads. Of great importance is also the availability of high-power laser diodes in the wavelength range of ytterbium absorption bands at 915 nm and 975 nm. Laser emission from ytterbium doped fibers has

been demonstrated over a wide wavelength range from 1-1.2  $\mu\text{m}$  [18]. At present a record power of 3 kW with nearly diffraction limited beam quality from an ytterbium doped fiber laser system was reported from IPG Photonics [19] in 2007. In single-pass amplifier configuration gain values of several ten dB in the range of 1020-1080 nm allow for a very simple signal amplification to high output power levels [20].

Narrow-linewidth signal amplification with LMA fibers was first demonstrated by Zawischa et al. [21] in 1999 with a neodymium doped step-index fiber. A non-planar ring-oscillator (NPRO) seed source with 800 mW of output power and an emission linewidth of approximately 1 kHz at 1064 nm was amplified up to 5.5 W. The maximum output power was limited by the onset of stimulated Brillouin scattering (SBS), owing to a small core diameter of 11  $\mu\text{m}$  and a large fiber length of 30 m. A limitation that was already well known from passive fiber optical systems for telecommunication applications [22]. High signal intensities and large interaction lengths in optical fibers enhance optical nonlinear effects such as SBS and stimulated Raman scattering (SRS) that limit the maximum achievable output power.

With shorter ytterbium doped step-index fibers of only 9 m length and larger core diameters of up to 30  $\mu\text{m}$  the SBS threshold could be substantially increased first up to 20 W by Höfer et al. [23] in 2001 and later up to 100 W of output power by Liem et al. [24] in 2003. These amplifiers used a NPRO seed source at 1064 nm. Despite their large core sizes the fibers could be operated with nearly diffraction limited beam quality by coiling the fibers and introducing large propagation losses for higher-order modes [25].

The strong absorption of ytterbium doped silica glass at 975 nm and a small ratio between pump cladding and signal core area allow for an efficient pump light absorption, helping to reduce fiber length and mitigate optical nonlinearities. A further increased fiber core diameter would certainly result in an even higher SBS threshold power, but the aforementioned coiling technique gets less efficient and the beam quality of step-index fibers with core diameters larger than 30  $\mu\text{m}$  is typically degraded. The doping concentration of ytterbium doped silica fibers is limited by the formation of ion clusters at high doping levels resulting in severe transmission losses through lifetime quenching and photodarkening [26, 27]. In this respect increasing the doping concentration does only to some extent help to reduce the absorption length of the active fibers.

Two alternative SBS suppression schemes have been successfully applied in high-power narrow-linewidth fiber amplifiers. Strong temperature gradients induced by the absorption

of pump radiation result in a frequency shift of the Brillouin gain profile, which broadens the Brillouin spectrum and lowers the effective Brillouin gain for each frequency component generated along the fiber. This approach was followed by Jeong et al. [28] first in 2005 with 264 W of output power. Later in 2007 a maximum output power of 402 W was demonstrated with a polarization extinction ratio of 16 dB and nearly diffraction-limited beam quality ( $M^2 < 1.1$ ) [16]. The polarization maintaining (PM) ytterbium doped fiber had core and pump cladding diameters of  $25 \mu\text{m}$  and  $380 \mu\text{m}$  and a total length of 6.5 m. At present this result represents the highest narrow-linewidth signal power demonstrated with a diffraction-limited beam quality in PM operation. Almost 500 W were obtained with a non-polarized output and a beam propagation parameter  $M^2$  of 1.6 from a 9 m long fiber with  $42 \mu\text{m}$  core and  $650 \mu\text{m}$  cladding size. These experiments have been carried out with a 60 kHz linewidth distributed feedback laser diode, pre-amplified with three fiber amplifier stages from 80 mW up to 3.5 W.

A different suppression scheme was developed by Gray et al. [29] also in 2007. The fiber core refractive index profile was modified for a reduced overlap between optical and acoustic modes that drive the Brillouin scattering process. Similar output power up to 502 W were demonstrated, non-polarized and with a beam propagation factor  $M^2$  of 1.4. The authors used a fiber laser seed source with an emission linewidth of 3 kHz and 100 mW of output power, pre-amplified up to 5 W. The main amplifier comprised an 8.5 m long ytterbium doped SBS suppressed fiber with a core and cladding diameter of  $40 \mu\text{m}$  and  $400 \mu\text{m}$ , respectively. This fiber was bi-directionally pumped, indicating that an SBS suppression through pump induced thermal gradients could be neglected.

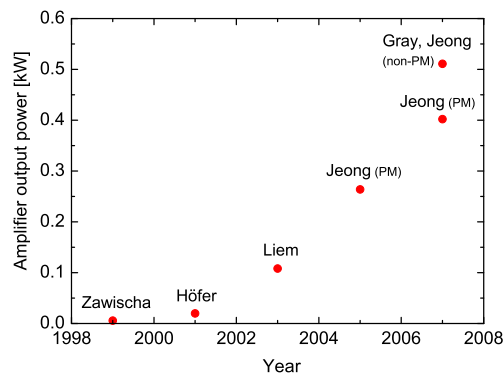


**Figure 2.2:** Historical review of narrow-linewidth master-oscillator fiber amplifier power levels published in recent years by different authors.

Different output power that have been demonstrated in recent years from narrow-linewidth master-oscillator fiber amplifier systems are summarized in Fig. 2.2.

At the time of this work only standard ytterbium doped LMA step-index fibers and alternatively photonic crystal fibers (PCF) were commercially available, both without special designs for an SBS suppression. One of each kind was chosen with similar fiber core sizes and used for the amplification of a narrow-linewidth laser source.

## 2.2 Detection of Brillouin scattering spectra

Although the deformation of the Brillouin scattering spectrum during amplifier operation and the manipulation of the fiber intrinsic Brillouin gain spectrum play a key role for the suppression of SBS in high-power LMA fiber amplifiers, only little attention has been paid to the experimental detection of these spectra in the past. More surprisingly, as various detection methods have been developed for the investigation of SBS in bulk optical glasses and passive single-mode fibers.

Early studies on Brillouin scattering spectra in bulk quartz and fused silica glass were already carried out in 1968 by Durand et al. [30] using a Fabry-Pérot interferometer. This approach was later applied for optical fibers in 1972 by Ippen et al. [31].

Nowadays, a widely used detection technique is the pump-and-probe measurement [32]. It is based on two separate narrow-linewidth laser signals. One for pumping the medium and excite a Brillouin gain spectrum and the second to provide a frequency tunable probe beam. The Brillouin spectrum is obtained by measuring the amplification of the probe beam while frequency tuned over the range of Brillouin gain. This highly accurate detection method is particularly suitable for a determination of the intrinsic Brillouin gain profile of the fiber at low signal or pump intensities.

Another commonly used detection scheme is the heterodyne detection, where Brillouin scattered light is mixed with a fraction of signal light acting as a reference wave or local oscillator [33]. The mixer is typically a photo-detector with an output proportional to the square of the input amplitude. In this way the detected photocurrent can be expressed with the electric fields  $E_s$  and  $E_{bs}$  of the signal and Brillouin scattered light as

$$I_{\text{phot}} = S (E_s^2 + E_{bs}^2 + 2E_s E_{bs} \cos((\omega_s - \omega_{bs})t + \Delta\varphi) \cos \phi) \quad (2.1)$$

Here,  $S$  is the detector efficiency,  $\Delta\varphi$  the phase difference and  $\phi$  the polarization angle



---

between both light beams. Consequently, the heterodyne detection scheme generates an electronic signal at the intermediate beat frequency  $\omega_s - \omega_{bs}$ . The amplitude of this signal is directly proportional to the amplitude of the local oscillator and therefore allows for a sensitive detection of Brillouin signals.

In this work the pump-and-probe and heterodyne detection methods have been modified and applied for the investigation of Brillouin scattering spectra in ytterbium doped LMA fibers. The intrinsic Brillouin gain spectrum was detected using pump-and-probe measurements, whereas the evolution of Brillouin spectra during high-power amplifier operation was determined with heterodyne detection.



## 3. Theory

### 3.1 Stimulated Brillouin scattering

In optical fibers light scattering can take the form of Raman, Brillouin, Rayleigh and Rayleigh-wing scattering with their Stokes and anti-Stokes components at lower and higher frequencies with respect to the signal frequency  $\nu_s$  (Fig. 3.1). Light scattering occurs as a consequence of fluctuations in the optical properties of the traversed medium.

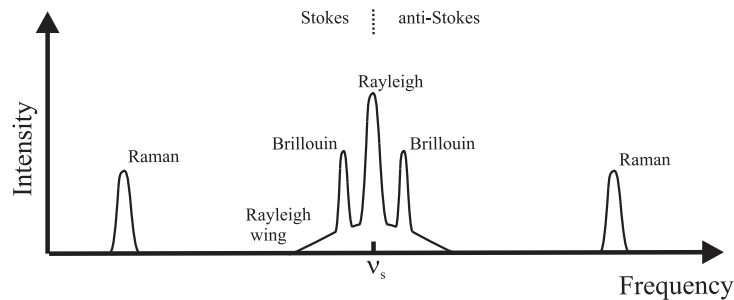


**Figure 3.1:** Typical light scattering spectrum [34].

Rayleigh scattering is the scattering from non-propagating density fluctuations and is known as quasi-elastic scattering because it induces no frequency shift.

Rayleigh wing scattering results from fluctuations in the orientation of anisotropic molecules. Since the molecular reorientation process is very rapid, Rayleigh wing scattering is spectrally very broad.

Although Raman scattering and Brillouin scattering are quite similar in their origin, different dispersion relations for the involved optical and acoustic phonons result in different Stokes shifts and emission bandwidth. Raman scattering results from vibrational modes

of the molecules and can be described as scattering from optical phonons. In fused silica fibers the frequency shift of the main scattered components from the incident signal is in the range of 13 THz and shows a widespread spectrum that can extend over 20-30 THz [35].

Brillouin scattering is the scattering of light from propagating density and pressure waves. It can also be considered as scattering from acoustic phonons. The Brillouin scattering frequency shift is very small with 10-20 GHz and the spectral width is very narrow with typically less than 200 MHz [34].

Since for narrow-linewidth laser sources the effect of Raman and Rayleigh scattering is orders of magnitude smaller than Brillouin scattering, this section will focus on the description of spontaneous and stimulated Brillouin scattering (SBS). A detailed description of different scattering processes in optical fibers can be found in books from Boyd [34] and Agrawal [36].

The inelastic scattering of light induced by acoustic phonons was first described by Léon Brillouin [37] in 1922 and four years later independently by Leonid Isaakovich Mandelstam [38]. For this reason it is mostly referred to as Brillouin scattering or sometimes Brillouin-Mandelstam scattering. Experimentally the spontaneous scattering process was first observed in bulk quartz in 1950 by Krishnan [39]. The first observation of SBS was made by Chiao et al. [40] in 1964.

At low signal intensities spontaneous Brillouin scattering results from thermal density fluctuations and is a random, statistical process (Fig. 3.2 a). For sufficiently intense signals this scattering process can undergo a transition from spontaneous to stimulated Brillouin scattering. In this case the incident and scattered light fields can interfere and give rise to density variations by means of electrostriction and generates an acoustic pressure wave that propagates along the fiber in the direction of the incident signal (Fig. 3.2 b).

The tendency of materials to become compressed in the presence of an electric field is called electrostriction. Each molecule in a field  $E$  develops a dipole moment  $p = \alpha E$ , where  $\alpha$  is the molecular polarizability, and is pulled into the region of increasing field strength [34]. The increase in density of the material by  $\Delta\rho$  changes its dielectric constant from  $\epsilon_0$  to the value  $\epsilon_0 + \Delta\epsilon$ , where

$$\Delta\epsilon = \left( \frac{\delta\epsilon}{\delta\rho} \right) \Delta\rho \quad (3.1)$$

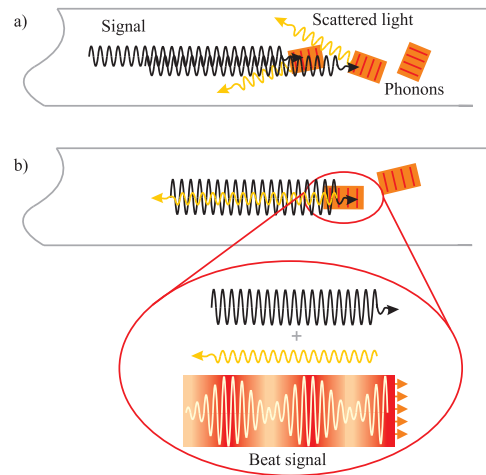


**Figure 3.2:** Schematic representation of a) spontaneous and b) stimulated Brillouin scattering.

Another mechanism by which the interference of the laser and Stokes wave can drive a pressure or acoustic wave is optical absorption. In material regions of high optical intensity the absorptive heat load tends to expand the material and excites density waves. This effect can only occur in lossy optical media and is therefore less common in fiber optical systems.

Incident light being scattered off refractive index variations induced by electrostriction will have the Stokes frequency and add constructively with the Stokes radiation. The Stokes frequency shift and direction of scattering can be understood by considering the conservation of momentum (Fig. 3.3). Assuming that the acoustic wave is driven by the

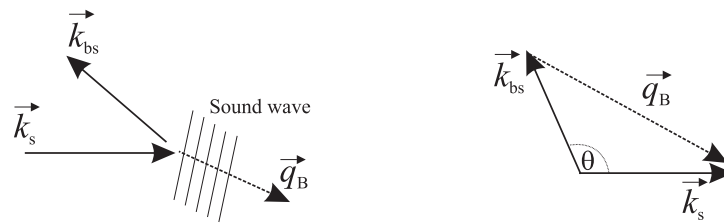


**Figure 3.3:** Wave vector of the stimulated Brillouin scattering process.

beating of the laser signal and Stokes field the wave vectors of the incident signal  $\vec{k}_s$ , Brillouin scattered light  $\vec{k}_{bs}$  and acoustic sound wave  $\vec{q}_B$  satisfy the following relation

$$\vec{k}_s - \vec{k}_{bs} = \vec{q}_B \quad (3.2)$$

Energy conservation can be expressed with the respective signal  $\omega_s$ , Brillouin scattered light  $\omega_{bs}$  and acoustic wave  $\Omega_B$  frequencies. The acoustic wave frequency represents the

Brillouin scattering induced frequency shift and is commonly called the Brillouin frequency.

$$\omega_s - \omega_{\text{bs}} = \Omega_B \quad (3.3)$$

The acoustic frequency  $\Omega_B$  and the wave vector  $\vec{q}_B$  satisfy the dispersion relation

$$\Omega_B = v_a |\vec{q}_B| \approx 2v_a \left| \vec{k}_s \right| \sin(\theta/2) \quad (3.4)$$

with the speed of sound  $v_a$  and the scattering angle  $\theta$ . For a medium with small changes of refractive index  $n$  in the wavelength range of the incident signal the absolute optical wave vectors almost coincide  $|\vec{k}_{\text{bs}}| \approx |\vec{k}_s| = n\omega_s/c$ , if the optical frequencies are almost equal  $\omega_{\text{bs}} \approx \omega_s$ . These approximations are well applicable for Brillouin scattering in fused silica fibers and a signal wavelength in the range of  $\lambda_s = 1\text{-}1.55 \mu\text{m}$ . For this reason, SBS does in principle only occur in the backward direction with the Brillouin frequency shift given by

$$\nu_B = \Omega_B/2\pi = 2nv_a/\lambda_s \quad (3.5)$$

The following equations describe the nonlinear coupling among the optical and acoustic fields. These equations were taken from Boyd [34]. The electric field in the Brillouin medium is represented as

$$\tilde{E}(z, t) = \tilde{E}_s(z, t) + \tilde{E}_{\text{bs}}(z, t) \quad (3.6)$$

with the signal field  $\tilde{E}_s(z, t)$  propagating in positive and the Brillouin scattered light field  $\tilde{E}_{\text{bs}}(z, t)$  in negative direction.

$$\tilde{E}_s(z, t) = A_s(z, t) e^{i(k_s z - \omega_s t)} + c.c. \quad (3.7)$$

$$\tilde{E}_{\text{bs}}(z, t) = A_{\text{bs}}(z, t) e^{i(-k_{\text{bs}} z - \omega_{\text{bs}} t)} + c.c. \quad (3.8)$$

The acoustic field is described in terms of the material density distribution

$$\tilde{\rho}(z, t) = \rho_0 + [\rho(z, t) e^{i(qz - \Omega t)} + c.c.] \quad (3.9)$$

where  $\rho_0$  is the mean density and  $q = 2k_s$ . Here,  $\Omega$  can be different from the Brillouin frequency  $\Omega_B$  in Eq. (3.4). In order to obtain the amplitude of the nonlinear perturbation induced in the medium an electrostrictive force is introduced and the material density is assumed to obey the following acoustic wave equation

$$\frac{\partial^2 \tilde{\rho}}{\partial t^2} = -\Gamma' \nabla^2 \frac{\partial \tilde{\rho}}{\partial t} - v_a^2 \nabla^2 \tilde{\rho} = \nabla \cdot f \quad (3.10)$$

with the electrostrictive constant  $\gamma_e = \rho (\partial\varepsilon/\partial\rho)$ , a damping parameter  $\Gamma'$  and a source term

$$\nabla \cdot f = \frac{\gamma_e q^2}{4\pi} [A_s A_{bs}^* e^{i(qz - \Omega t)} + c.c.] \quad (3.11)$$

The slowly varying amplitude approximation, which assumes that the amplitude varies slowly compared with an optical wavelength or optical period, allows to neglect second order derivatives with respect to space propagation and time. Under this assumption these equations lead to the result

$$-2i\Omega \frac{\partial \rho}{\partial t} + (\Omega_B^2 + \Omega^2 - i\Omega\Gamma_B) \rho - 2iqv_a^2 \frac{\partial \rho}{\partial z} = \frac{\gamma_e q^2}{4\pi} A_s A_{bs}^* \quad (3.12)$$

with the Brillouin linewidth  $\Gamma_B = q^2 \Gamma'$ . Its reciprocal  $\tau_p = \Gamma_B^{-1}$  gives the phonon lifetime.

Under approximation that the phonon propagation distance with a few micrometer can be neglected compared to the optical field propagation length of several meters and under steady-state condition the spatial and time derivatives in this expression vanish and the acoustic amplitude is given by

$$\rho(z, t) = \frac{\gamma_e q^2}{4\pi} \frac{A_s A_{bs}^*}{\Omega_B^2 + \Omega^2 - i\Omega\Gamma_B} \quad (3.13)$$

The spatial evolution of the optical fields is described by the wave equation

$$\frac{\partial^2 \tilde{E}_{s,bs}}{\partial z^2} - \frac{1}{(c/n)^2} \frac{\partial^2 \tilde{E}_{s,bs}}{\partial t^2} = \frac{4\pi}{c^2} \frac{\partial^2 \tilde{P}_{s,bs}}{\partial t^2} \quad (3.14)$$

with the nonlinear polarization acting as a source term in this equation. The contributions that can act as phase-matched source terms for the laser and Stokes fields are

$$\tilde{P}_s = \frac{\gamma_e}{4\pi\rho_0} \rho A_{bs} e^{i(k_s z - \omega_s t)} + c.c. \quad (3.15)$$

$$\tilde{P}_{bs} = \frac{\gamma_e}{4\pi\rho_0} \rho^* A_s e^{i(k_{bs} z - \omega_{bs} t)} + c.c. \quad (3.16)$$

With the optical field and wave equations and the nonlinear polarization source terms the following equations can be obtained under slowly-varying amplitude approximation.

$$\frac{\partial A_s}{\partial z} + \frac{1}{c/n} \frac{\partial A_s}{\partial t} = \frac{i\omega\gamma_e}{2nc\rho_0} \rho A_{bs} \quad (3.17)$$

$$-\frac{\partial A_{bs}}{\partial z} + \frac{1}{c/n} \frac{\partial A_{bs}}{\partial t} = \frac{i\omega\gamma_e}{2nc\rho_0} \rho^* A_s \quad (3.18)$$

In these equations it is assumed that  $\omega = \omega_s \cong \omega_{\text{bs}}$ . Considering again steady-state conditions, the time derivatives vanish and the coupled-amplitude equations become

$$\frac{\partial A_s}{\partial z} = \frac{i\omega q^2 \gamma_e^2}{8\pi n c \rho_0} \frac{|A_{\text{bs}}|^2 A_s}{\Omega_{\text{B}}^2 - \Omega^2 - i\Omega \Gamma_{\text{B}}} \quad (3.19)$$

$$\frac{\partial A_{\text{bs}}}{\partial z} = \frac{-i\omega q^2 \gamma_e^2}{8\pi n c \rho_0} \frac{|A_s|^2 A_{\text{bs}}}{\Omega_{\text{B}}^2 - \Omega^2 + i\Omega \Gamma_{\text{B}}} \quad (3.20)$$

These equations show that the SBS process is automatically phase-matched and is a pure gain process. For this reason, coupled intensity equations of the two interacting optical waves can be introduced [34]. The background loss coefficient of the optical fiber  $\alpha$  is equal for signal  $I_s$  and Brillouin scattered light intensity  $I_{\text{bs}}$ . Signal and Brillouin scattered light propagate in forward and backward z-direction with a positive and negative sign, respectively.

$$\frac{dI_s}{dz} = -g_{\text{B}} I_s I_{\text{bs}} - \alpha I_s \quad (3.21)$$

$$\frac{dI_{\text{bs}}}{dz} = -g_{\text{B}} I_s I_{\text{bs}} + \alpha I_{\text{bs}} \quad (3.22)$$

The SBS gain factor  $g_{\text{B}}$  is given to good approximation by a Lorentzian function [34]

$$g_{\text{B}}(\Omega) = g_{\text{B}_0} \frac{(\Gamma_{\text{B}}/2)^2}{(\Omega_{\text{B}} - \Omega)^2 + (\Gamma_{\text{B}}/2)^2} \quad (3.23)$$

with the Brillouin gain spectral width at full width half maximum (FWHM)  $\Delta\nu_{\text{B}} = \Gamma_{\text{B}}/2\pi$  and the peak gain factor at  $\Omega = \Omega_{\text{B}}$

$$g_{\text{B}_0} = \frac{\gamma_e^2 \omega^2}{n v_{\text{a}} c^3 \rho_0 \Gamma_{\text{B}}} \quad (3.24)$$

These equations assume that both optical waves are linearly polarized along the same axis and maintain their states of polarization along the fiber. This is the case in polarization-maintaining (PM) fibers [41]. In the fiber amplifier rate-equation model that is introduced in the following section the coupling between the narrow-linewidth signal and Brillouin scattered light is based on these two coupled intensity equations.

Assuming signal and Stokes waves with a linear polarization along the same axis maintained over the entire fiber length a solution for the coupled intensity equations (Eqs. 3.21 and 3.22) is found. For an estimate of the Brillouin threshold in passive fibers, pump depletion can be neglected so that  $I_s = I_s(0)e^{-\alpha z}$  and a solution for the Stokes intensity is given by

$$I_{\text{bs}}(0) = I_{\text{bs}}(L)e^{(g_{\text{B}} I_s(0) L_{\text{eff}} - \alpha L)} \quad (3.25)$$



where  $L$  is the fiber length and  $L_{\text{eff}} = (1 - \exp(-\alpha L))/\alpha$  is the effective interaction length. In this expression the Stokes intensity grows exponentially with distance as it propagates in the  $-z$ -direction from an initial value at  $z = L$ .

Defining the SBS threshold, where the Brillouin scattered light power equals the signal power at the fiber input ( $z = 0$ ), an estimate for the threshold input power  $P_{\text{th}}$  was given by Smith [22] from Eq. (3.25) for typical single-mode fiber parameters as

$$P_{\text{th}} = \frac{21K A_{\text{eff}}}{g_{\text{B}_0} L_{\text{eff}}} \quad (3.26)$$

with the effective mode area  $A_{\text{eff}}$  and a factor  $K$  for the signal polarization state later introduced by van Deventer et al. [41].  $K = 1$  for a maintained linear polarization along the fiber and 1.5 for a completely scrambled polarization.

Typical values for fused silica fibers are an electrostrictive constant  $\gamma_e \approx 0.902$ , a mean density  $\rho_0 \approx 2210 \text{ kg/m}^3$ , a speed of sound  $v_a \approx 5960 \text{ m/s}$  and an optical refractive index  $n = 1.45$  [36]. The phonon lifetime  $\tau_p$  is typically less than 10 ns with a width of the Brillouin gain spectrum of 10-200 MHz. With these values the approximate Brillouin frequency shift  $\nu_B$  for a narrow-linewidth laser signal at 1064 nm is 16.2 GHz. Typical peak Brillouin gain values of fused silica fibers are in the range of  $1\text{-}3 \cdot 10^{-11} \text{ m/W}$  [42]. A Lorentzian shaped Brillouin gain profile with a spectral width of 50 MHz is plotted in Fig. 3.4 normalized to the peak gain value  $g_{\text{B}_0}$ .

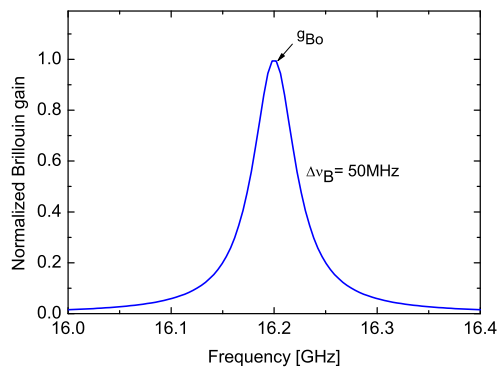


**Figure 3.4:** Calculated Brillouin scattering gain profile.

Approximate SBS threshold power calculated with Eq. (3.26) for different typical LMA fiber core diameters are plotted with respect to the fiber length in Fig. 3.5. The Brillouin gain was assumed to be  $2.5 \cdot 10^{-11} \text{ m/W}$ , attenuation  $\alpha = 0.01 \text{ m}^{-1}$  and the polarization

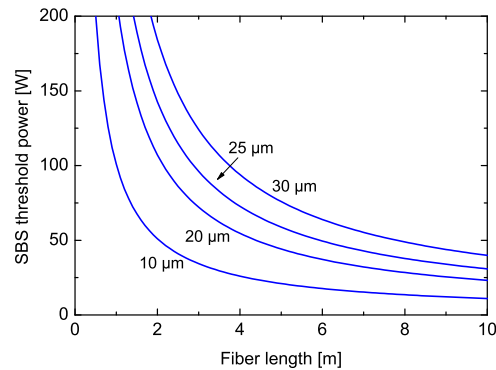


**Figure 3.5:** Estimate of SBS threshold power for different LMA fiber cores and lengths.

factor was set to  $K = 1$  for a linearly polarized signal in a PM fiber [41]. According to this approximation the maximum power transmitted through passive LMA fibers with core diameters of less than  $30 \mu\text{m}$  is below 100 W for fibers longer than 4 m (Fig. 3.5).

In high-power fiber amplifiers the signal power shows a substantially different distribution along the active fiber compared to the nearly constant power distribution in passive fibers with only a small attenuation by background losses, as assumed in Eq. (3.26). The threshold power in LMA fiber amplifiers can thus be expected to be larger than these results. For instance an output power of 100 W was demonstrated by Liem et al. [24] with a  $28 \mu\text{m}$  core diameter and a fiber length of 9.4 m, which is more than twice the threshold SBS power that is expected from Eq. (3.26). To account for gain and signal distributions along active amplifier fibers a more comprehensive model is therefore needed.

The Brillouin gain is maximum for continuous-wave (CW) or quasi-CW signals, with a spectral width  $\Delta\nu_s$  significantly smaller than  $\Delta\nu_B$ . For pulses shorter than the phonon lifetime ( $\tau_p < 1 \text{ ns}$ ) the Brillouin gain can even be reduced below the Raman gain and stimulated Raman scattering becomes the dominant nonlinear effect [36]. Even for a CW signal, the Brillouin gain is reduced considerably if the spectral linewidth exceeds the Brillouin spectral width. This happens for multi-mode lasers or for single-mode lasers with rapid phase variations. In this case the Brillouin gain depends on the relative magnitudes of signal-coherence length and the SBS interaction length with a phonon propagation distance typically in the range of  $10 \mu\text{m}$ . The peak gain value was found to be reduced by a factor  $\Delta\nu_B/(\Delta\nu_s + \Delta\nu_B)$  by Lichtman et al. [43].

In Fig. 3.6 this dependence is plotted for a Brillouin spectral width of 50 MHz. A signal

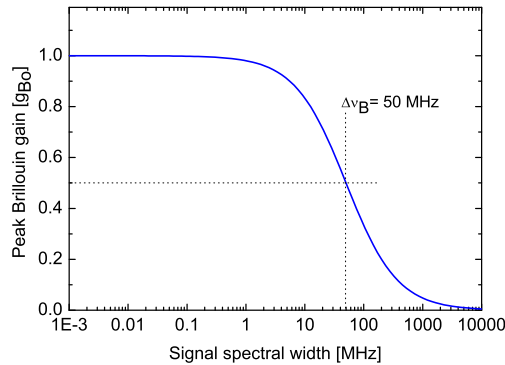


**Figure 3.6:** Calculated dependence of the peak Brillouin gain value  $g_{B_0}$  on the spectral width of the incident signal  $\Delta\nu_s$  for a Brillouin spectral width of  $\Delta\nu_B = 50$  MHz [43].

modulation producing frequency sidebands or a broadband seed source with multiple longitudinal modes does therefore effectively suppress SBS in fiber optical systems [44].

## 3.2 Numerical model

In this section the numerical model is introduced that was developed to simulate the signal amplification and evolution of Brillouin scattering in ytterbium doped fiber amplifiers.

The numerical model is based on coupled rate- or intensity equations for the contributing signals. Similar models have been used to describe seed signal, amplified spontaneous emission (ASE) and pump light evolution in erbium doped single-mode fiber amplifiers by Desurvire and Giles et al. [1, 45] and later adapted by Hardy et al. [46] for ytterbium and neodymium doped double-clad fibers. Combining coupled intensity equations for the signal and Brillouin scattering (Eq. (3.21 and (3.22)) with such amplifier rate-equations, numerical models for the growth of Brillouin scattering in fiber amplifiers were introduced by Pannell et al. [47] for erbium and later by Brilliant [48] for ytterbium doped fibers. The latter rate-equation model comprised only a single spectral line to describe the first order Brillouin Stokes power. In order to account for the spectral shape and deformation of Brillouin scattering during high-power amplifier operation different models have been developed by Kovalev et al. [49] and Liu [50].

The involved signals and propagation directions described by the present numerical model are illustrated in Fig. 3.7. Seed, pump, amplified spontaneous emission (ASE) and Bril-

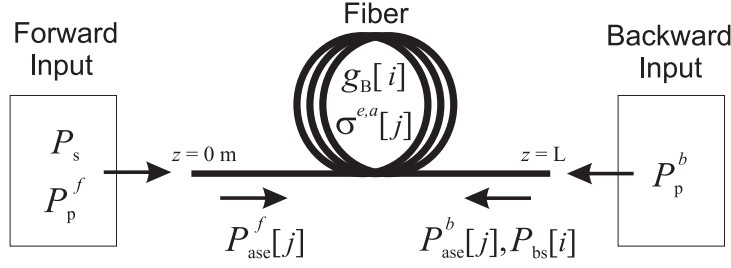


**Figure 3.7:** Schematic fiber amplifier setup.

loun scattering signal power ( $P_s, P_p, P_{ase}$  and  $P_{bs}$ ) were calculated propagating along the fiber in the forward direction in positive and in backward direction in negative  $z$ -direction. The corresponding set of differential equations was solved numerically using a Runge-Kutta algorithm and a shooting method.

$$\frac{dP_s}{dz} = \Gamma_s P_s (N_2 \sigma_s^e - N_1 \sigma_s^a) - \alpha_s P_s - P_s \sum_i g_{B_i} (P_{bs_i} + P_{ni}) / A_{\text{eff}} \quad (3.27)$$

$$\pm \frac{dP_p^{f,b}}{dz} = \Gamma_p P_p^{f,b} (N_2 \sigma_p^e - N_1 \sigma_p^a) - \alpha_p P_p^{f,b} \quad (3.28)$$

$$\pm \frac{dP_{ase_j}^{f,b}}{dz} = \Gamma_s P_{ase_j}^{f,b} (N_2 \sigma_{ase_j}^e - N_1 \sigma_{ase_j}^a) - \alpha_s P_{ase_j}^{f,b} + \Gamma_s N_2 \sigma_{ase_j}^e P_{0_j} \quad (3.29)$$

$$\frac{dP_{bs_i}}{dz} = -\Gamma_s P_{bs_i} (N_2 \sigma_{bs_i}^e - N_1 \sigma_{bs_i}^a) + \alpha_s P_{bs_i} - P_s \sum_i g_{B_i} (P_{bs_i} + P_{ni}) / A_{\text{eff}} \quad (3.30)$$

$$N_2 = N_0 \frac{W_{12}}{W_{12} + W_{21} + 1/\tau} \quad (3.31)$$

$N_2$  is the excited ion density which results from the stimulated emission  $W_{21}$  and absorption  $W_{12}$  rates of all contributing signals in the doped fiber core area  $A_{\text{co}}$  and the spontaneous decay rate with the inverse ion fluorescence lifetime of  $1/\tau$ . The amplifier model was solved under steady-state approximation, where the time derivative of the inversion density  $dN_2/dt$  equals zero.

$$W_{21} = (\Gamma_s \sigma_s^e P_s \lambda_s + \Gamma_p \sigma_p^e P_p \lambda_p + \Gamma_s \sum_j \sigma_{ase_j}^e P_{ase_j}^{f,b} \lambda_{ase_j} + \Gamma_s \sum_i \sigma_{bs_i}^e P_{bs_i} \lambda_{bs_i}) / hc A_{\text{co}} \quad (3.32)$$

$$W_{12} = (\Gamma_s \sigma_s^a P_s \lambda_s + \Gamma_p \sigma_p^a P_p \lambda_p + \Gamma_s \sum_j \sigma_{ase_j}^a P_{ase_j}^{f,b} \lambda_{ase_j} + \Gamma_s \sum_i \sigma_{bs_i}^a P_{bs_i} \lambda_{bs_i}) / hc A_{\text{co}} \quad (3.33)$$

The doping concentration of the ytterbium ions  $N_0$  is assumed to be equal to the sum of ion densities in the upper  $N_2$  and lower  $N_1$  energy levels ( $N_0 = N_1 + N_2$ ).

In order to account for the transversal overlap of the guided fundamental  $LP_{01}$  mode with the doped fiber core region and the double-clad fiber pumping configuration the filling or

overlap factors  $\Gamma_s$  and  $\Gamma_p$  are introduced for the seed and pump radiation. The overlap integral for the signal intensity distribution  $I(r, \phi)$  with the ion density in the ground state  $N_1(r, \phi)$  is [45]

$$\Gamma_s = \frac{\int_0^{2\pi} \int_0^\infty I(r, \phi) N_1(r, \phi) r dr d\phi}{\overline{N_1}} \quad (3.34)$$

where  $\overline{N_1}$  is the mean doping density over the core area. For a Gaussian beam approximation to the optical mode profile and a uniform doping distribution the overlap factor simplifies to

$$\Gamma_s = 1 - \exp\left(-\frac{r_{co}}{w_s}\right)^2 \quad (3.35)$$

where  $w_s$  is the mode radius defined at  $1/e^2$  of the Gaussian intensity profile. According to Giles et al. [45] the ion population density over the core cross-section is independent on the optical power for ratios of  $r_{co}/w_s$  smaller or close to one and can thus be neglected. For a confined transverse mode with a large evanescent field outside the core area ( $w_s \gg r_{co}$ ) this approximation would not be valid.

The pump overlap factor is in general defined by the ratio of fiber core and cladding area  $A_{cl}$ . Depending on the cladding geometry (circular, D-shaped, hexagonal, octagonal,...) pump light modes may be differently scrambled and absorbed in the doped core region [51]. In circular fiber cladding designs helical modes can occur that do not pass through the fiber core and hence are not absorbed. By coiling the fiber in a kidney-shape this effect can be reduced. To accommodate for these characteristics a factor  $S$  is introduced. For fiber pump cladding geometries optimized for a well scrambled pump light propagation  $S$  is typically close to one [51].

$$\Gamma_p = \frac{A_{co}}{A_{cl}} S \quad (3.36)$$

Background losses for the signal and pump induced by fiber imperfections and scattering are  $\alpha_s$  and  $\alpha_p$ . For simplicity the overlap factor and background loss, as well as the effective mode field area  $A_{eff}$  for the seed signal were assumed to be equal for ASE and Brillouin scattering. The effective mode field diameter MFD is approximated from the fiber V-parameter being defined by the core radius  $r_{co}$ , numerical aperture NA and signal wavelength  $\lambda_s$  [52].

$$V = \frac{2\pi r_{co} NA}{\lambda_s} \quad (3.37)$$

$$MFD = 2r_{co} (0.65 + 1.619 \cdot V^{-1.5} + 2.879 \cdot V^{-6}) \quad (3.38)$$

Emission and absorption cross-sections of the ytterbium doped fiber are  $\sigma^e$  and  $\sigma^a$ . An absorption spectrum provided by Nufern [53] was scaled to match the peak absorption cross-section value at 975 nm published by Pask et al. [18]. The emission cross-sections were calculated with the McCumber formalism [54] using the energy level diagram of ytterbium doped fused silica glass also published in Ref. [18] (Fig. 3.8 and 3.9). The energy

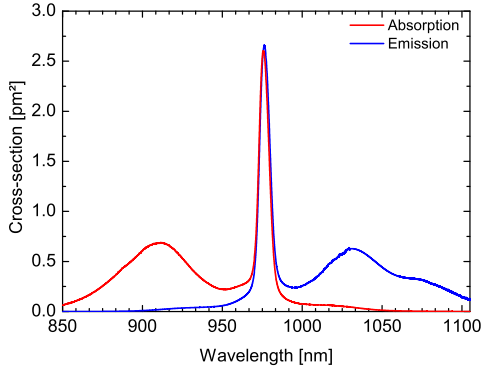


**Figure 3.8:** Emission- and absorption cross-sections of an ytterbium doped fiber [18, 53].

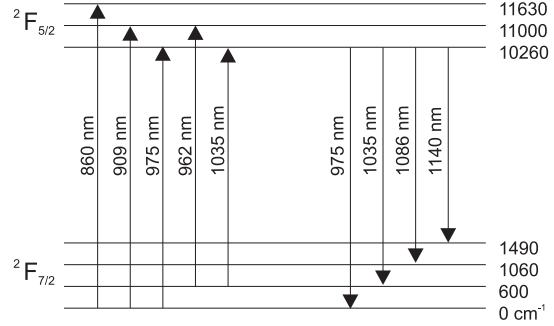


**Figure 3.9:** Energy level diagram of ytterbium doped fused silica glass [18].

distribution results from the electric field induced Stark effect and splitting of the energy levels. The very simple electronic level structure with only one excited state leads to low quantum defects with reduced thermal effects and excludes parasitic effects such as excited-state absorption and quenching [20]. However, the lower laser level is so close to the ground state that it can easily be thermally populated leading to increased laser thresholds and re-absorption losses in the emission wavelength range around 1035 nm. For this reason it is mostly called a quasi-three level system.

The upper state lifetime was estimated from the emission cross-section spectrum according to the Füchtbauer-Ladenburg method. Under assumption that the quantum efficiency of a laser transition is near unity, the upper-state lifetime is close to the radiative lifetime, which can be determined by the emission cross-section.

$$\frac{1}{\tau} = 8\pi cn^2 \int \frac{\sigma^e(\lambda)}{\lambda^4} d\lambda \quad (3.39)$$

Temperature influences on the absorption and emission cross-sections and the fluorescence lifetime characteristics were not included in the present model.

Broadband emission of backward ( $P_{ase_j}^b$ ) and forward ( $P_{ase_j}^f$ ) propagating ASE is described by a discrete number  $j$  of spectral lines. Each line at its wavelength  $\lambda_{ase}$  is initiated by a

noise photon power  $P_0 = 2hc/\lambda_{\text{ase}} \cdot \Delta\nu_{\text{ase}}$  within the calculated linewidth  $\Delta\nu_{\text{ase}}$ , where  $h$  is Planck's-constant and  $c$  the speed of light. The factor of 2 is introduced to account for two possible orthogonal polarization states for ASE in the active fiber core [1]. For the mathematical model  $P_0$  represents the boundary conditions for the backward and forward propagating ASE at the respective fiber ends  $P_0 = P_{\text{ase}_j}^f(0) = P_{\text{ase}_j}^b(L)$ .

A similar description was used for the backward propagating Brillouin scattered radiation with a discrete number  $i$  of spectral lines separated by a linewidth  $\Delta\nu_{\text{bs}}$ . These lines were calculated in the frequency range of Brillouin gain, which is described by the following Lorentzian shaped profile with peak gain value  $g_{\text{B}_0}$  and a bandwidth of  $\Delta\nu_{\text{B}}$ .

$$g_{\text{B}}(\nu_i) = g_{\text{B}_0} \frac{((\Delta\nu_{\text{B}} + c_{\text{b}}\Delta T)/2)^2}{(\nu_{\text{B}} - \nu_i + c_{\text{f}}\Delta T)^2 + ((\Delta\nu_{\text{B}} + c_{\text{b}}\Delta T)/2)^2} \quad (3.40)$$

Temperature gradients  $\Delta T$  along the fiber induced by absorbed pump radiation or externally applied heat cause a linear shift  $c_{\text{f}}$  of the center frequency and a linewidth change  $c_{\text{b}}$  of the Brillouin gain profile [42]. In contrast to Eq. (3.23) these influences of the amplifier fiber temperature on the Brillouin scattering with temperature changes along the fiber and the resulting Brillouin frequency dependencies were included in Eq. (3.40).

An estimate for the radial heat distribution in rare-earth doped fibers was found by Brown et al. [55]. This model includes convective and neglects radiative heat transfer. The deposited heat density  $Q$  results from the fraction of absorbed pump light over a certain fiber length and the quantum defect of the laser process  $\eta = (\lambda_{\text{s}} - \lambda_{\text{p}}) / \lambda_{\text{s}}$  determined by the pump and signal photon emission wavelength.

The center temperature  $T_{\text{co}}$  in a step-index fiber is related to the coolant temperature  $T_0$  by the following equations [55]

$$T_{\text{co}} = T_{\text{e}} + \frac{Q}{4} \left( \frac{1}{2k_{\text{sil}}} + \frac{1}{k_{\text{sil}}} \ln \left( \frac{r_{\text{cl}}}{r_{\text{co}}} \right) + \frac{1}{k_{\text{pol}}} \ln \left( \frac{r_{\text{pol}}}{r_{\text{cl}}} \right) \right) \quad (3.41)$$

where the fiber surface temperature

$$T_{\text{e}} = T_0 + \frac{Q}{2\pi r_{\text{pol}} h_{\text{c}}} \quad (3.42)$$

with the convective heat transfer coefficient  $h_{\text{c}}$ . The fiber surrounding polymer layer with radius  $r_{\text{pol}}$  was added to the formula published by Brown et al. [55]. In order to account for the fact that sections of the active fibers were coiled on a metal spool ( $h_{\text{sp}}$ ) or cooled in a special copper holder ( $h_{\text{cop}}$ ) the heat transfer coefficient was increased to match the respective conductive cooling conditions. In most thermal simulations of high-power fiber

laser systems only convective heat transfer between air and the fiber surface is considered [55, 56]. The radial heat transfer inside the fiber is given by the core, cladding and polymer radii with the respective material specific heat conductivities  $k_{\text{sil}}$  for fused silica glass and  $k_{\text{pol}}$  for the polymer coating.

In photonic crystal fibers the air-hole structure might increase the thermal resistance between the active core and the fiber surface. Especially rings of air-holes surrounding the inner micro-structure that form a cladding for pump light guidance can cause heat accumulation. Analytical and finite-element modeling of different PCF structures published by Limpert et al. [57] have revealed that a minimized width and length of the fused silica bridges between these air-holes still allow for an efficient heat removal comparable to standard step-index fibers. The specified bridge length of the PCF used during this work was  $6.5 \mu\text{m}$ . A bridge width was not specified. Simulations of a fiber with  $20 \mu\text{m}$  bridge length carried out by Limpert et al. [57] showed no significant temperature increase compared to a standard step-index fiber. For this reason thermal simulations of the PCF were performed using Eq. (3.41) neglecting additional terms for a possibly increased heat resistance due to the air-hole structure.

Various models have been published to describe the initiation of Brillouin scattering in active or passive fiber optical systems. In the so called localized, non-fluctuating source model the initiation of Brillouin scattering is described by a Brillouin photon scattered off a thermally excited phonon at the rear of the fiber [50, 58]. More complicated distributed or localized time-resolved fluctuating source models have been used to account for a stochastic noise initiation. A comparison of various SBS initiation models for passive fibers was made by Boyd et al. [59] and showed that in the range of the SBS threshold and below a non-fluctuating source is a good approximation. In the present numerical model a distributed, non-fluctuating source model that was introduced by Pannell et al. [47] with spontaneously generated Brillouin noise power at different positions along the amplifier fiber was implemented.

$$P_{n_i} = \frac{4h\nu_i\Delta\nu_{\text{bs}}}{(1 + (2(\nu_{\text{B}} - \nu_i)/\Delta\nu_{\text{B}})^2 (\exp(h\nu_{\text{B}}/kT) - 1))} \quad (3.43)$$

This equation describes the probability of occupation of a Brillouin state with a noise photon power once created distributed over a Lorentzian profile. The Brillouin power at the end of the fiber is described by the boundary condition  $P_{n_i} = P_{\text{bs}_i}(L)$ .

Alternatively a constant factor  $f \approx 10^{-12}$  was proposed by Boyd et al. [59] which describes the fraction of signal intensity that is being spontaneously backscattered to form a



Stokes seed for a single spectral line. Another description of the Brillouin scattering noise initiation was used by Brilliant [48] with a similar noise photon power  $P_n = h\nu\Delta\nu_{\text{bs}}$  that is being used for the ASE initiation. This value is several orders of magnitude smaller than the ones used by Boyd et al. [59] and Pannell et al. [47].

The numerical model comprised various input parameters that were not at all or only vaguely specified by the fiber manufacturers. In the following Table 3.1 the parameters are summarized that have been used for all the simulations presented in this work. Some of the parameters, if not exactly specified in the literature or by the manufacturers, were adjusted to match the experimentally observed results. For this reason, different amplifier configurations and active fibers with different amplifier characteristics and temperature distributions were investigated to gain a better understanding of the theoretical model and the physical processes of fiber amplification and Brillouin scattering. A detection of Brillouin scattering spectra during amplifier operation provides a deeper insight into the fiber temperature and signal power distributions. The parameters of the active fibers are summarized in the next chapter together with the experimental setup.

**Table 3.1:** Parameters included in the numerical simulations.

Parameter	Symbol	Value	Source
Pump overlap factor coefficient	$S$	0.9	Set
Fluorescence lifetime	$\tau$	950 $\mu\text{s}$	Calculated
Brillouin peak gain	$g_{\text{B}_0}$	2.4 m/W	Set
Cooling temperature	$T_0$	297 K	Set
Heat transfer coefficient - Fiber spool	$h_{\text{sp}}$	100 W/m <sup>2</sup> K	Set
Heat transfer coefficient - Copper holder	$h_{\text{cop}}$	500 W/m <sup>2</sup> K	Set
Thermal conductivity - Fused silica	$k_{\text{sil}}$	1.38 W/mK	[57]
Thermal conductivity - Polymer coating	$k_{\text{pol}}$	0.2 W/mK	[57]
Brillouin temperature frequency shift	$c_{\text{f}}$	2.25 MHz/K	Measured
Brillouin temperature linewidth change	$c_{\text{b}}$	-0.2 MHz/K	Set [42, 60]



## 4. Fiber amplifier setup

The amplifier experimental setup was based on the master-oscillator fiber amplifier (MOFA) scheme, where a low power seed source is amplified in one or more fiber amplifier stages. A non-planar ring oscillator (NPRO) served as the master-oscillator seed source. This laser was a commercially available system named Mephisto 2000N from Innolight GmbH [61]. It provided 2 W of output power in single-frequency continuous-wave (cw) operation with nearly diffraction limited beam quality (beam propagation factor  $M^2 < 1.1$ ). The spectral emission characteristic at 1064 nm is specified with a linewidth of 1 kHz (measured over 100 ms) and a long term stability of 1 MHz/min.

In a single-stage amplifier two different ytterbium doped large mode-area (LMA) fibers have been investigated with a step-index and a photonic crystal fiber with similar core, but different pump cladding diameters and different fiber lengths.

### Step-index fiber

The step-index fiber was a polarization-maintaining (PM) PANDA fiber (PLMA-YDF-20/400, Nufern [53]) with an ytterbium doped silica core and a surrounding silica pump cladding (Fig. 4.1) a. The fiber core is co-doped with germanium to adjust the low refractive index variation ( $n_{\text{co}} - n_{\text{cl}} \approx 10^{-4}$ ) between core and cladding and obtain low numerical apertures (NA) in the range of 0.06. Two boron doped stress-rods next to the fiber core induce a birefringence of  $3.78 \cdot 10^{-4}$  and form two constant principle axes (slow- and fast-axis). After the drawing process during cooling of the fiber mechanical strain is induced owing to the different thermal expansion coefficients of the boron rods and the surrounding silica glass. Light being linearly polarized parallel to one of these axis propagates with a maintained polarization. A low index ( $n_{\text{po}} \approx 1.37$ ) polymer coating provides light guidance by total internal reflection for the pump radiation with a high NA of 0.46 and forms an outer protection layer. Both fiber ends have been polished with an angle

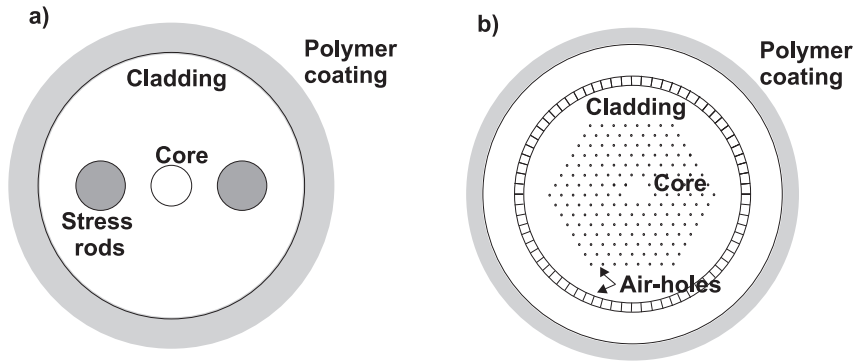


**Figure 4.1:** Schematic fiber structure of a) step-index fiber and b) photonic crystal fiber.

of  $8^\circ$  to avoid Fresnel reflections back into the fiber core and the resulting parasitic laser oscillations. The specified fiber parameters are summarized in Table 4.1.

**Table 4.1:** Specified fiber parameters of step-index and photonic crystal fiber.

	Nufern PLMA-YDF-20/400	Crystal Fibre DC-225-22-Yb
Core diameter	$19.8 \mu\text{m}$	$22 \mu\text{m}$
Core NA	0.055	0.04
Core background loss at 1300 nm	$0.001\text{-}0.01 \text{ m}^{-1}$	-
Inner cladding diameter	$400 \mu\text{m}$	$225 \mu\text{m}$
Inner cladding NA	0.46	0.62
Inner cladding background loss at 1300 nm	$0.002 \text{ m}^{-1}$	$< 0.011 \text{ m}^{-1}$
Outer cladding diameter	-	$471 \mu\text{m}$
Polymer diameter	$550 \mu\text{m}$	$552 \mu\text{m}$
Doping concentration $\text{Yb}_2\text{O}_3$	0.8 wt.%	0.6 wt.%
Absorption at 975 nm	1.7 dB/m	3.5 dB/m

### Photonic crystal fiber

The photonic crystal fiber (PCF) was a non-PM fiber fabricated by Crystal Fibre (DC-225-22-Yb) [62]. In such fibers a photonic crystal structure provides light guidance for the laser radiation by total internal reflection. This hexagonal structure is formed by air-holes having diameters of  $0.22 \mu\text{m}$  and a pitch, the distance between each other, of  $\Lambda$  of  $11 \mu\text{m}$ . Three central air-holes are replaced by ytterbium doped silica and form the triangular shaped active fiber core. The refractive index of the photonic crystal structure

is effectively lowered by the presence of the air-holes and light is confined in the core region similar to conventional fibers. Pump light is guided in a ring of air-holes surrounding the inner structure. In this fiber design a polymer coating is only needed for the mechanical protection of the fiber surface.

At both ends of the fiber the air-holes have been thermally collapsed over a distance of approximately 0.5 mm with a fusion splicer and afterwards polished with an angle of  $8^\circ$ . In this way the air-holes are being protected against dust and abrasives. Additionally the laser mode expands over the distance of this core-less end cap which reduces the beam intensity on the end facet of the fiber. A schematic picture of the fiber structure is shown in Fig. 4.1 b and the specified fiber parameters are summarized in Table 4.1.

External feedback can induce perturbations to the seed ring-oscillator and prevent low noise single-frequency operation. For this reason a Faraday isolator ( $> 35$  dB isolation) was placed between seed source and the fiber amplifier. The elliptically polarized seed radiation was linearized with a quarter- ( $\lambda/4$ ) and a half-wave plate ( $\lambda/2$ ) and adjusted for maximum transmission through the polarization-dependent isolator. With an additional half-wave plate the polarization plane in front of the active fiber could be adjusted. In order to optimize the signal coupling efficiency the focus size and NA was matched to the fiber core parameters with a lens system consisting of one plano-convex lens (focal length  $f=200$  mm) for beam collimation and another plano-convex ( $f=100$  mm) and an aspheric lens ( $f=8$  mm) for focusing into the active fiber core. A schematic representation of the complete fiber amplifier system is shown in Fig. 4.2. The active fibers were

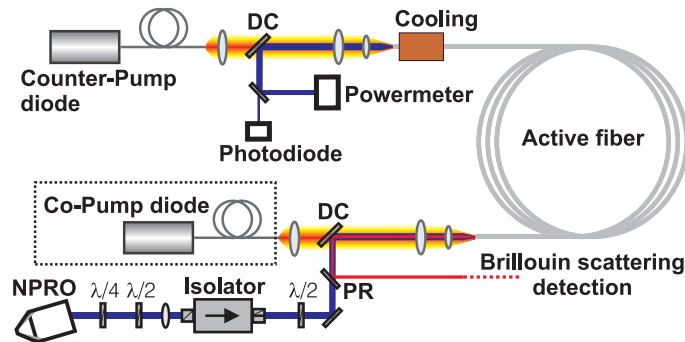


**Figure 4.2:** Experimental setup of the master-oscillator fiber amplifier. DC dichroic mirror, PR partially reflecting mirror.

pumped with a fiber coupled laser diode module from Laserline (LDM 200-200) [63]. For subsequent experimental and theoretical investigations on different fiber amplifier sys-

tems the fiber coupled diode pump module was characterized with respect to its optical power and emission spectrum. The pump fiber had a diameter of  $300\ \mu\text{m}$  and a NA of 0.22. At maximum control voltage of 5 V a pump power of 212 W behind all pump optics incident on the active fiber was measured (Fig. 4.3). The diode module was equipped with

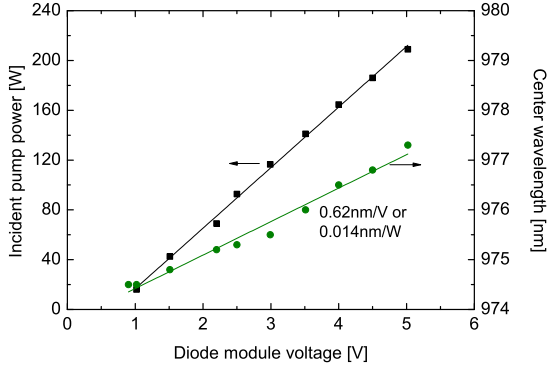


**Figure 4.3:** Pump power incident on active fibers and corresponding center emission wavelength.

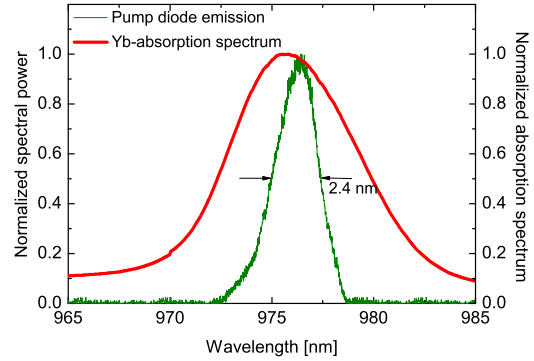


**Figure 4.4:** Normalized emission spectrum of the diode module and ytterbium absorption spectrum.

an automatic temperature control for stabilization of the center emission wavelength to 975 nm. However, the diode emission still showed a wavelength shift with respect to the pump power of  $0.014\ \text{nm/W}$  (Fig. 4.3). In the theoretical model this wavelength shift of the pump light was considered. With an emission bandwidth of 2.4 nm (full width at half maximum, FWHM) the diode emission was well below the ytterbium absorption peak width (Fig. 4.4). For this reason the spectral width and shape of the pump light was neglected in the presented simulations.

Slightly different lens systems were used to couple the pump light into the two different active fibers. In both cases the pump beam from the laser diode module was passed through a dichroic mirror (DC) high-reflective for 1020-1100 nm and highly transmissive around 975 nm to separate pump and signal radiation. The collimated pump beam (collimation focal length  $f=40\ \text{mm}$ ) was then focused through a plano-convex lens ( $f=100\ \text{mm}$ ) after a propagation distance of 150 mm. With a plano-convex lens ( $f=40\ \text{mm}$ ) placed in 40 mm distance to the first focusing lens a coupling efficiency of 85% into the active step-index fiber ( $400\ \mu\text{m}$  diameter) was achieved. In the case of the PCF a Gradium lens ( $f=10\ \text{mm}$ ) from LightPath [64] was placed after 70 mm instead of the last focussing plano-convex lens for an optimized imaging into the pump cladding ( $225\ \mu\text{m}$  diameter). Gradium lenses exhibit an axial refractive index variation which results in a reduction of spherical aber-

rations and optimized imaging quality. Compared to aspheric lenses with similar imaging characteristics the damage threshold of Gradium lenses is higher. With this pump imaging system a coupling efficiency into the PCF similar to the one obtained with the step-index fiber was achieved.

Both pump light imaging systems were simulated with the ray-tracing program Zemax [65] revealing theoretical coupling efficiencies similar to the experimental results in the range of 87-90% including Fresnel reflection losses at the fiber surface and imperfect anti-reflection coatings of the lenses.

In this work pump configurations with co- and counter-propagating pump and signal radiation have been investigated. The highest pump power was applied in counter-pumped configuration with more than 150 W. At these pump power levels cooling of the active fiber was required. To avoid damage induced by high absorptive heat load from the doped core, the fiber was placed from top and bottom in V-grooves milled along two 15 cm long water cooled copper plates. A refractive index matching gel ( $n_g=1.6$ ) surrounding the fiber prevented guidance of uncoupled pump light through total internal reflection inside the polymer coating. Pump light being guided in the coating material gets absorbed and gradually damages the fiber.





# 5. Fiber amplifier characteristics

In this chapter a general characterization of the amplified output obtained from the step-index and the photonic crystal fiber (PCF) is presented. The amplifier output power and efficiency, the optical spectra, polarization state and beam quality have been investigated. Experimental data of the amplifier output power and optical spectra are compared with results from the numerical rate-equation model. Whereas step-index fiber amplifiers have been characterized and presented in the past in various publications, some parameters of PCF high-power amplifiers have not been studied and will therefore be analyzed in more detail in this chapter.

## 5.1 Output power and efficiency

### Step-index fiber

The step-index fiber amplifier system was operated with pump light counter- and co-propagating to the seed signal radiation in order to investigate possible influences on the amplifier performance and the evolution of Brillouin scattering. A maximum output power of 92 W in counter- and 38 W in co-pumped configuration was obtained with nearly identical slope efficiencies of 76% measured with respect to the launched pump power (Fig. 5.1). For both pump configurations the maximum amplifier output power was limited by the onset of stimulated Brillouin scattering (SBS). Although the amplifier did not show a degradation of the amplifier output power, SBS was identified with different detection methods. A detailed investigation on the SBS threshold and its influences on the step-index fiber amplifier operation are presented in Chapter 6.

With a seed signal power of 1.25 W coupled into the active fiber core gain values of 19 dB and 15.5 dB were obtained at maximum output power. The optical-to-optical efficiencies at

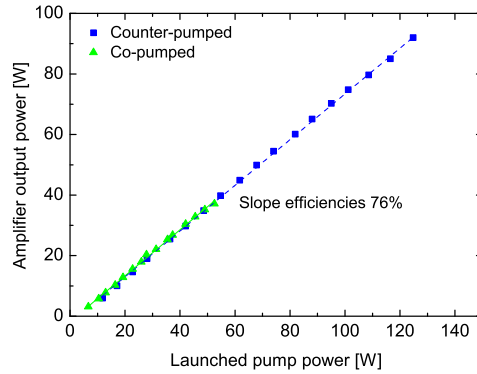


**Figure 5.1:** Experimental output power characteristic of the step-index fiber amplifier in co- and counter-pumped configuration.

maximum output power were in the range of 65%. During amplifier operation 5-10% of the launched pump power was transmitted through the 8 m long fiber with a slight variation originating from power dependent pump diode wavelength shifts that were described in Chapter 4.

In order to compare the amplifier performance coupled rate-equations (Eqs. (3.27)) have been solve numerically for the pump and signal power and the inversion along the active fiber are shown in Figs. 5.2 and 5.3 with an equivalent launched pump power of 52 W for both pump configurations. For the counter-pumped amplifier the inversion level stays

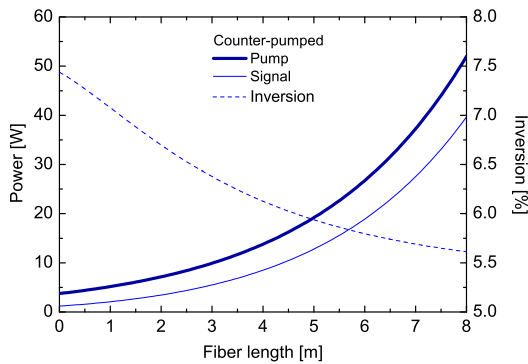


**Figure 5.2:** Simulation of signal, pump and inversion along step-index fiber length for counter-pumped amplifier.

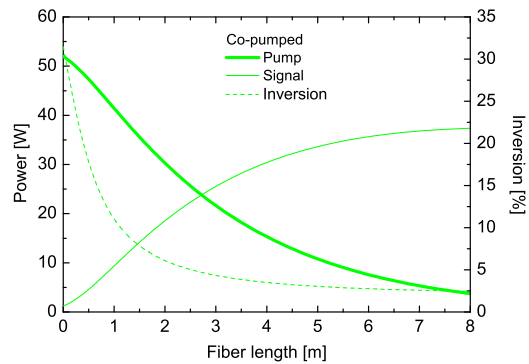


**Figure 5.3:** Simulation of signal, pump and inversion along step-index fiber length for co-pumped amplifier.

nearly constant between 5.5-7.5% owing to a pump and signal intensity ratio along the fiber that allows for a homogeneous power extraction. In co-pumped configuration the

inversion level rises up to 25% of excited ions at  $z = 0$  m due to large pump and low signal intensities. As a consequence, a fiber amplifier in counter-pumped configuration exhibits slightly better conversion efficiencies. The signal output power was calculated to be 38 W in counter- and lower in co-pumped configuration with 36 W. This difference might be reduced for a slightly longer fiber length. The reason that this characteristic was not observed experimentally was mainly attributed to an inaccurate detection of the pump power launched into the fiber cladding. These values were obtained by measuring the transmitted pump light through a few cm length of the step-index fiber. However, with a specified absorption of 1.7 dB/m, pump radiation gets considerably absorbed already over a short fiber length of a few cm. A cut-back method, where transmission values are determined at different fiber lengths, can be applied to identify absorption losses and minimize this error. This technique was not applied owing to the large costs of LMA step-index fibers. Additionally, Fresnel reflections at the fiber end facets need to be estimated and considered. An accuracy of  $\pm 1\%$  was estimated for experimental values of the launched pump power.

### Photonic crystal fiber

The master-oscillator PCF amplifier was only operated in counter-pumped configuration for an optimized amplifier efficiency and SBS suppression. With respect to the launched pump power a slope efficiency of 77% was achieved (Fig. 5.4). This result is basically equivalent to the one observed from the step-index fiber amplifier. At maximum available

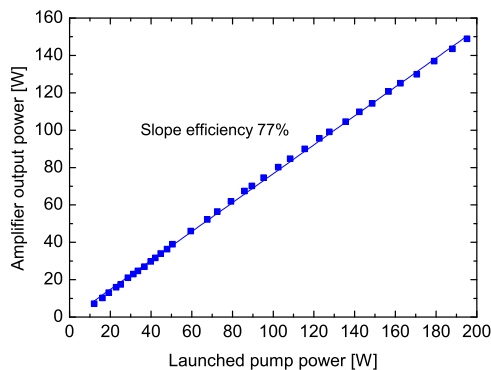


**Figure 5.4:** Experimental output power characteristic of the PCF amplifier.

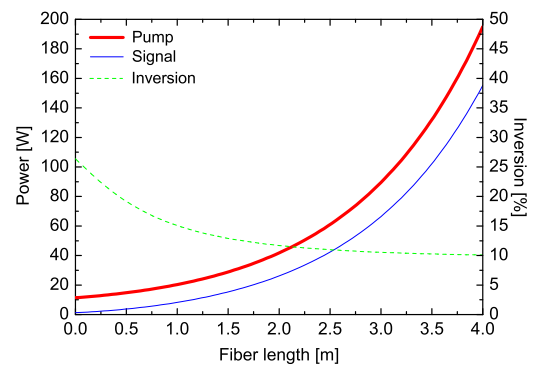


**Figure 5.5:** Simulation of signal, pump and inversion along PCF length at 148 W of amplifier output power.

pump power of 212 W incident and approximately 195 W launched into the fiber an amplifier output power of 148 W was achieved corresponding to an optical-to-optical conversion efficiency of 70%. The transmitted pump power was less than 5% of the launched pump power over the whole amplifier power range. Simulations of the signal, pump and inversion distribution at maximum pump power are plotted in Fig. 5.5. Similar to the step-index fiber amplifier in co-pumped configuration the inversion is significantly increased up to 26% at  $z = 0$  m. For the PCF this effect is even more pronounced owing to larger pump intensities and a shorter absorption length compared to the step-index fiber, resulting from the small ratio of pump cladding and signal core area.

## 5.2 Polarization

### Step-index fiber

Independent of the amplifier output power and pump configuration the linear polarized amplifier output from the step-index fiber showed a polarization extinction ratio (PER =  $10 \cdot \log(P_{\max}/P_{\min})$ ) in the range of 18-20 dB determined with a half-wave plate rotated for maximum and minimum transmission of the amplified beam through a polarizing beam splitter.

### Photonic crystal fiber

Although the PCF was not intentionally designed for a polarization maintaining (PM) operation the fiber amplifier output showed a remarkable PER of up to 28 dB at maximum output power. These results are close to the maximum extinction ratio of the polarizing beam splitter used for the PER measurement that was specified with 30 dB. Birefringence in PCF has been attributed to imperfections in the air-hole structure such as inaccurate air-hole size and position by Bjarklev et al. [66].

In Fig. 5.6 the measured PER of the PCF amplifier is plotted with respect to the angle of the linear seed polarization incident on the active fiber at 148 W of amplifier output power. A maximum PER was observed every 90° rotation. Separated by approximately 40° from this maximum a second maximum with a slightly lower PER of 23 dB was observed. Although the degree of linear polarization was basically constant at different amplifier pump power, the rotation angle of the seed polarization for an optimized PER had to be

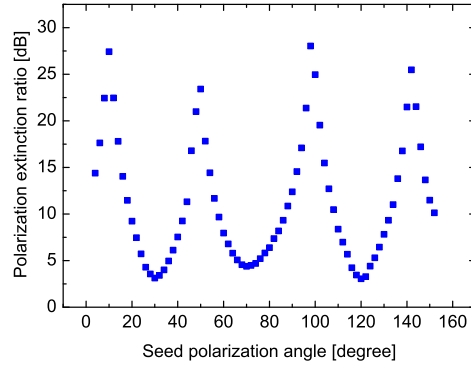


**Figure 5.6:** Polarization extinction ratio of the PCF amplifier output at 148 W of output power with respect to the seed polarization angle.

readjusted by some degrees, owing to apparent changes in pump light induced thermal stress birefringence along the active fiber.

A strong effect on the PER was observed for different fiber coiling diameters. As expected, a tight coiling of the PCF is additionally accompanied by increased macro-bending losses and hence decreases the amplifier extraction efficiency [67]. In order to achieve efficient amplifier operation with optimized power conversion efficiency and PER, the influence of fiber coiling was investigated with respect to these parameters (Table 5.1).

**Table 5.1:** Slope efficiency and polarization extinction ratio at different PCF coiling diameters.

Fiber coiling diameter	Slope efficiency	Polarization extinction ratio
15 cm	65%	5 dB
20 cm	72%	22 dB
25 cm	77%	28 dB
30 cm	77%	28 dB

Four different fiber spools were used with diameters of 15 cm, 20 cm, 25 cm and 30 cm. At coiling diameters of 15 cm and 20 cm a significant amplifier performance degradation was observed with PER of 5-22 dB and slope efficiencies of 65-72%. For 25 cm and 30 cm coiling diameter the best results were obtained with 77% slope efficiency and a maximum PER of 28 dB. The PCF amplifier was therefore operated with a coiling diameter of 25 cm.

## 5.3 Beam quality

### Step-index fiber

The beam quality of the step-index fiber was characterized with a CCD-camera and a determination of the beam propagation factor  $M^2$ , which is a measure of the deviation from a fundamental  $TEM_{00}$  Gaussian beam (Figs. 5.7 and 5.8).

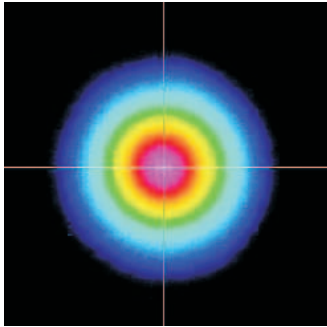


**Figure 5.7:** CCD-camera beam profile of the step-index fiber amplifier output beam.

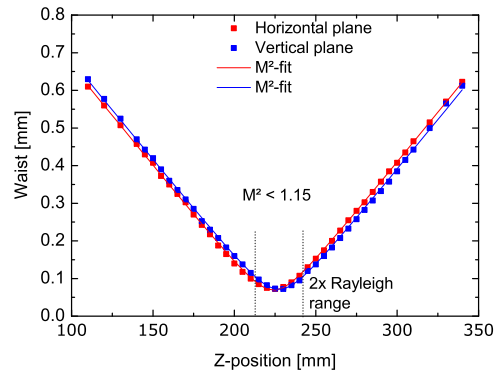


**Figure 5.8:** Beam propagation factor  $M^2$  of the step-index fiber amplifier measured at 90 W of output power.

In principle in the step-index fiber core approximately five transversal modes are confined with a  $V$ -parameter of 3.5 determined with Eq. (3.37). However, with a fiber coiling diameter of 16 cm the introduced macro-bending losses sufficiently suppressed higher order modes, while propagation losses for the fundamental mode still allowed for an efficient amplifier operation [25]. At maximum output power of 92 W in counter-pumped configuration  $M^2$  values better than 1.15 for the vertical and horizontal plane were determined with a knife-edge technique, where beam radii were determined at different positions along the focused beam [68]. The CCD-camera intensity profile showed a nearly perfect Gaussian beam profile with no significant aberrations.

### Photonic crystal fiber

Intensity distributions of the electro-magnetic field in a PCF with a triangular shaped core have been investigated by Limpert et al. [69]. In spite of the triangular shaped mode a laser operation of such a PCF with 80 W of output power was demonstrated with  $M^2$

values of  $1.2 \pm 0.1$ . Theoretical considerations on  $M^2$  factors of different PCF reported in Ref. [70] predict similar values in the range of 1.22 for fundamental transverse-mode operation of this type of fiber.

In order to obtain a detailed characterization of the PCF amplifier beam quality different experimental approaches were applied. Measuring the caustic of the focused amplified beam with a CCD-camera,  $M^2$  values in the range of  $1.12 \pm 0.05$  to  $1.17 \pm 0.05$  were determined, depending on the measuring axis and output power. A plot of an  $M^2$  measurement at maximum output power of 148 W is shown in Fig. 5.10 with the measuring planes X and Y set to the triangular output beam geometry as illustrated in the CCD-camera picture in Fig. 5.9. The beam waist was defined by the second moment diameter [71]. At relatively

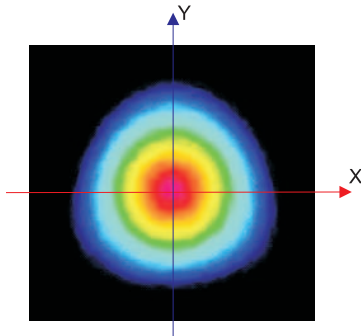


**Figure 5.9:** CCD-camera far-field beam profile of the PCF amplifier output beam.

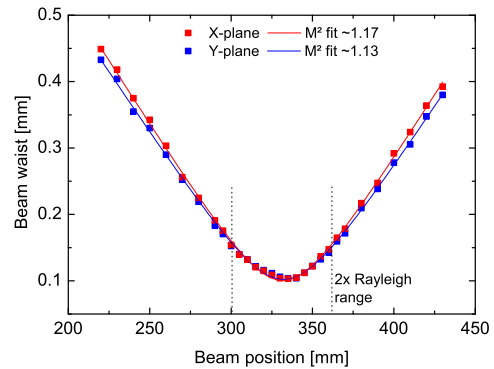


**Figure 5.10:**  $M^2$  measurement of the PCF amplifier at 148 W of output power.

low output power around 28 W the beam propagation factor only slightly improved with  $M^2$  of  $1.14 \pm 0.05$  and  $1.12 \pm 0.05$  in the X and Y plane, respectively.

To investigate the real overlap of the PCF transverse-mode with a Gaussian fundamental mode, sensitive beam quality measurements were carried out with a Fabry-Pérot ring-cavity, also referred to as premode cleaner (Figs. 5.11) [72]. The ring-cavity is formed by three mirrors with one curved mirror ( $R \approx 1$  m) installed on a piezo-electric transducer to scan over the free spectral range (FSR=714 MHz). The finesse of this cavity was in the range of 200 for the p-polarization that was used for the beam quality measurements. By scanning the length of the ring-cavity over a FSR, the relative power of the higher order transverse-modes can be obtained with respect to the Gaussian  $TEM_{00}$  mode. The ring cavity decomposes the beam into an expansion of Hermite-Gaussian modes. A program for an automatic analysis of the resulting mode scan has been developed by Kwee et

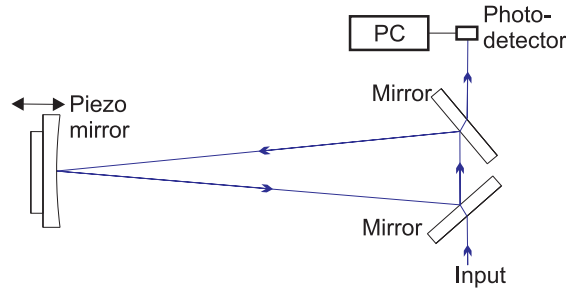


**Figure 5.11:** Schematic experimental setup of the Fabry-Pérot ring-cavity premode cleaner (FSR=714 MHz, Finesse  $\approx 200$ ).

al. [73] and the fundamental mode power can be determined. The PCF amplifier beam was analyzed with the ring-cavity. Scans over one FSR of the ring-cavity are plotted with normalized intensity and frequency axis for 28 W and 148 W of output power in Figs. 5.12 and 5.13, respectively. In both cases, the analyzed beam was attenuated to about

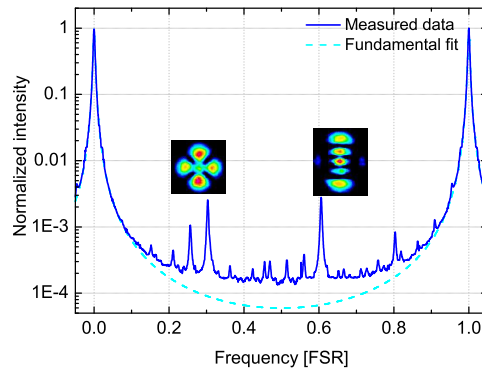


**Figure 5.12:** Normalized transmitted power through Fabry-Pérot ring cavity of the PCF amplifier at 28 W of output power.

200 mW to avoid damage of the ring-cavity. At an amplifier output power of 28 W the overlap with the fundamental Gaussian transverse-mode (dashed line) was measured to be 98%. These results coincide with premode cleaner beam quality measurements carried out with single-frequency amplifiers at 10 W of output power using different ytterbium doped standard step-index LMA fibers performed by Weßels et al. [74]. Insets of Fig. 5.12 show two transmitted higher-order modes that contribute both around 0.25% to the higher-order mode power. These beam profiles were taken with a CCD-camera in transmission to the premode cleaner while slowly scanning over the FSR of the ring-cavity.



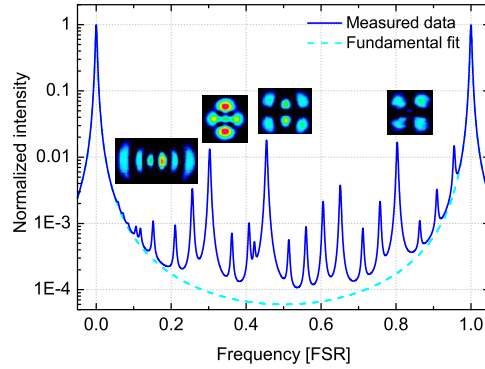


**Figure 5.13:** Normalized transmitted power through Fabry-Pérot ring cavity of the PCF amplifier at 148 W of output power.

As the fiber coiling diameter of 25 cm and therefore the propagation losses for higher-order modes were not changed during these experiments, the higher-order mode power with respect to the fundamental mode power of the amplifier output beam is ideally expected to stay the same when increasing the pump power. However, the increased thermal load inside the PCF gives rise to transversal mode profile deformations and hence changes the higher order mode content [75]. This can be seen in Fig. 5.13, showing a premode cleaner scan at 148 W of amplified output power. Besides the higher-order modes at the normalized length of 0.3 FSR and 0.6 FSR, already observed at lower output power (insets of Fig. 5.12), several more pronounced modes arise at higher output power illustrated by the insets of Fig. 5.13. These modes individually carry up to 1.8% of the total output power. However, the overlap with the fundamental Gaussian transverse-mode was still 92.6%.

## 5.4 Optical spectrum

In large gain amplifiers such as ytterbium doped fibers spontaneous emission can be amplified to high power levels. This unwanted process typically limits the available gain and produces amplifier excess noise. The power contribution of amplified spontaneous emission (ASE) is determined by the saturation level of the active fiber core by the signal intensity.

### 5.4.1 Seed saturation

#### Step-index fiber

In order to estimate the seed power needed for a saturated operation of the step-index fiber, the amplifier output power was simulated and measured for different seed power at a fixed pump power of 35 W (Fig. 5.14). At a maximum available seed power of 1.25 W coupled into the step-index fiber the amplifier was still operated below the fiber saturation level. For simulated seed power larger than 1.5 W a linear dependence of the amplifier output power on the injected seed power was observed, representing a fully saturated amplifier operation. The saturation level of a fiber amplifier slightly varies at increased pump power as higher inversion and gain levels may lead to an increased ASE power. However, operating the step-index fiber amplifier at higher output power with low seed power can easily damage the fiber through chaotic self-lasing.

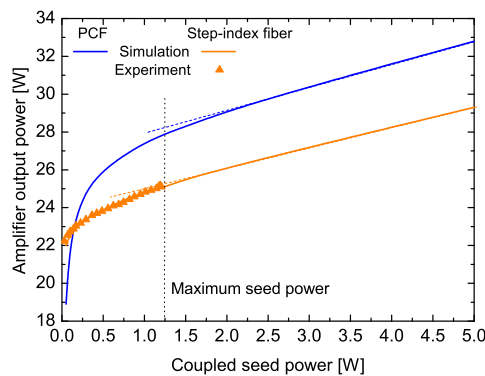


**Figure 5.14:** Experimental and simulated amplifier output power as function of the coupled seed power of step-index fiber and PCF amplifier.

#### Photonic crystal fiber

For the PCF amplifier the same simulations were performed at a launched pump power of 36 W. As a result of the larger mode field diameter and hence lower signal intensity, complete amplifier saturation was estimated to be obtained at seed power larger than 2 W (Fig. 5.14). Experimentally the seed saturation characteristic of the PCF amplifier was not investigated, to avoid damages of the fiber.

## 5.4.2 ASE suppression

### Step-index fiber

Optical spectra of the step-index fiber amplifier output were measured with an optical spectrum analyzer. Although the fiber was not fully saturated the optical spectra showed a well suppressed ASE with 42 dB in counter- and 43 dB in co-pumped configuration, corresponding to integrated ASE power of 2.2 mW and 1.8 mW, respectively (Fig. 5.15). For comparison these spectra were recorded at an output power of 35 W for both pump configurations.

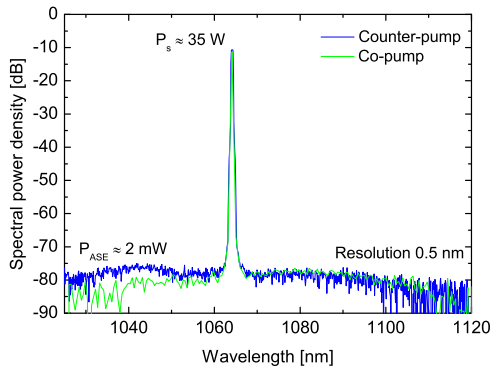


**Figure 5.15:** Optical spectra of the step-index fiber amplifier output recorded at 35 W amplifier power.

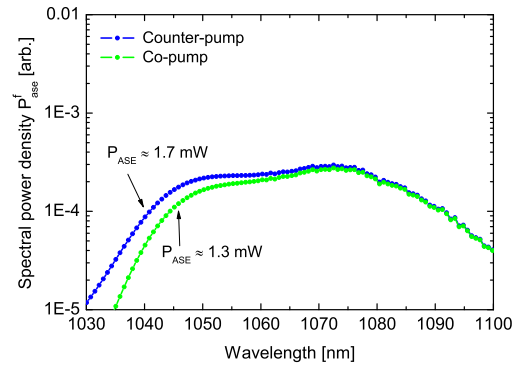


**Figure 5.16:** Simulation of ASE spectra from counter- and co-pumped step-index fiber amplifier at 35 W output power.

The ASE suppression was calculated by integrating over the measured optical spectra and comparing the total ASE power with respect to the signal peak at 1064 nm taking into account the optical spectrum analyzer (OSA) effective resolution bandwidth of  $\Delta\lambda_{\text{osa}} = 0.55$  nm. The resolution can be determined from a sample spectrum of the seed signal peak, as the nonplanar ring-oscillator (NPRO) emission linewidth is significantly smaller compared to the OSA resolution bandwidth.

Suppression of ASE close to the signal wavelength was approximately 70 dB. These ASE contributions dominate the low frequency amplifier excess noise as a result of the ASE-signal beat noise.

Concerning the shape and width of the simulated forward propagating ASE spectra and the integrated ASE power

$$P_{\text{ase}}^f = \sum_j P_{\text{ase}_j}^f \cdot \Delta\lambda_{\text{ase}} \quad (5.1)$$

a good agreement between theoretical and experimental results was found with a slightly better suppression of 43-44 dB (Fig. 5.16). The simulations of the ASE were performed with a number  $j = 100$  of spectral lines distributed from 1030-1100 nm, corresponding to a model spectral resolution of  $\Delta\lambda_{\text{ase}} = 0.7$  nm. Integrated forward ASE power ( $P_{\text{ase}}^f$ ) of 1.7 mW and 1.3 mW were calculated at amplifier output power of 35 W in counter- and co-pumped configuration, respectively. At maximum output power of 92 W in counter-pumped configuration the integrated ASE was measured and simulated to be still well suppressed with 42 dB and 44 dB.

### Photonic crystal fiber

As a consequence of the high inversion levels along the PCF (Fig. 5.5), reabsorption losses in the wavelength range below 1040 nm are reduced and the maximum amplifier gain is shifted towards shorter wavelengths. For this reason the ASE spectrum detected from the PCF amplifier showed a maximum spectral intensity at a wavelength around 1035 nm (Fig. 5.17).

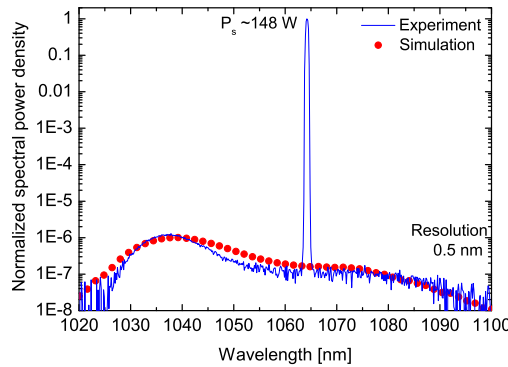


**Figure 5.17:** Simulated and measured optical spectra of the PCF amplifier output recorded at 148 W of amplifier output power.

The suppression of ASE was slightly lower compared to the one observed from the step-index fiber amplifier with 40 dB, due to the larger core diameter and the corresponding seed power required for a saturated amplifier operation. At maximum amplifier output power of 148 W an integrated ASE power of 15 mW was estimated.

---

Simulations of the ASE spectrum were performed from 1020-1100 nm with a number  $j = 50$  of spectral lines giving a calculation resolution of 1.6 nm (Fig. 5.17). The simulated ASE power of 20 mW and a corresponding ASE suppression of 39-40 dB at an amplifier output power of 148 W was nearly identical to the experimental results with a similar shape of the ASE spectrum.



## 6. Brillouin scattering detection

A variety of experimental methods can be applied to detect stimulated Brillouin scattering (SBS) and its influences in fiber optical systems. In this chapter a detection of some of these influences on the step-index and photonic crystal fiber amplifier is presented with measurements of backscattered light power, optical spectra and the amplifier relative intensity noise. Spontaneous Brillouin scattering gain spectra at low signal intensities are investigated with a pump-and-probe technique, whereas the Brillouin spectral evolution during amplifier operation is determined with a heterodyne detection scheme. The experimental results together with a numerical modeling of the power and spectral evolution will be employed to explain the growth of Brillouin scattering in different high-power fiber amplifier configurations.

### 6.1 Pump-and-probe measurements

Important parameters for the investigation and modeling of SBS in optical fibers are the shape, width and peak value of the spontaneous Brillouin scattering gain spectra. These spectra are generated at very low signal intensities with no pump light launched into the active fibers. Brillouin gain profiles from passive single-mode fibers have been detected with Fabry-Pérot spectrum analyzers [76] or pump-and-probe spectroscopy techniques [32, 42]. In order to obtain most accurate spectral parameters a pump-and-probe measurement similar to the one presented by Shibata et al. [32] was performed.

The NPRO seed source was coupled into the active fiber as described previously in Chapter 4 providing the pump beam to generate a Brillouin gain profile along the fiber under test (Fig. 6.1). A second NPRO providing the probe beam was coupled into the fiber counter-directionally to the seed beam. The linear polarization of both NPROs behind their respective isolators was oriented parallel for maximum Brillouin gain using half-

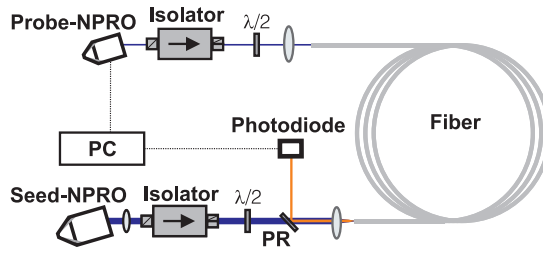


**Figure 6.1:** Pump-and-probe setup for measurement of spontaneous Brillouin gain spectra. PR partial reflecting mirror ( $R=10\%$ ).

wave plates. While scanning the probe laser frequency over the range of Brillouin gain the transmitted probe intensity was monitored with a photodetector, which was connected to a PC with an analog-digital converter. Frequency tuning of the probe NPRO was done by slowly modulating the Nd:YAG crystal temperature. The NPRO laser was equipped with a temperature modulation input specified with  $1\text{ K/V}$  and  $-3\text{ GHz/K}$ .

Controlled by a PC with a digital-analog converter a voltage span from  $0\text{ V}$  to  $0.2\text{ V}$  was scanned. The corresponding frequencies were determined by detecting beat signals of the seed and probe beams with a fast photodetector and an electronic spectrum analyzer (Fig. 6.2). A frequency span of approximately  $745\text{ MHz}$  was scanned with a sweep time

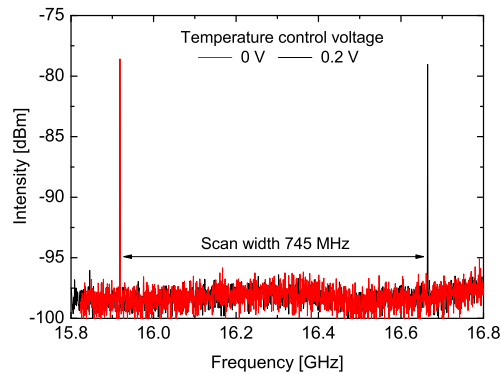


**Figure 6.2:** Calibration of pump-and-probe measurement with signal and probe beat signals at  $0\text{-}0.2\text{ V}$  modulation voltage.

of  $50\text{ s}$ . The spectral resolution was limited by the 12 bit resolution of the digital-analog and analog-digital converters that have been used for temperature modulation and data acquisition. A minimum step size of  $0.3\text{ mV}$  could be applied corresponding to an uncertainty of approximately  $1\text{ MHz}$  for each frequency scan step. Depending on the generated Brillouin gain and the resulting probe profile intensity a deviation of  $1\text{-}3\text{ MHz}$  on the



spectral width of the detected Brillouin spectra was estimated. With a frequency drift of 1 MHz/min the error contribution of the NPRs could be neglected.

### Step-index fiber

For the determination of the step-index fiber Brillouin scattering gain spectrum the described pump-and-probe technique was applied. Although the spectral shape and width of Brillouin gain spectra can be accurately determined with this approach, a careful investigation of experimental influences on the spectral shape is necessary. Intense pump and probe beams might distort the detected spectra through pump light depletion and spectral gain narrowing.

As has been reported by Niklès et al. [42] a depletion of pump radiation induced by the probe beam may result in distortion of the detected Brillouin spectra. The depletion is larger around the maximum of the gain spectrum, which decreases the residual Brillouin gain for these frequencies and effectively flattens the detected spectra. In order to eliminate possible errors induced by large probe beam intensities, the Brillouin spectral width was determined for different probe power from 5 mW to 12 mW at a constant seed power of 25 mW. The spectral width showed no significant broadening for increased probe intensities (Fig. 6.3). Subsequent pump-and-probe experiments have been carried out with a probe power of 10 mW coupled into the fiber core.

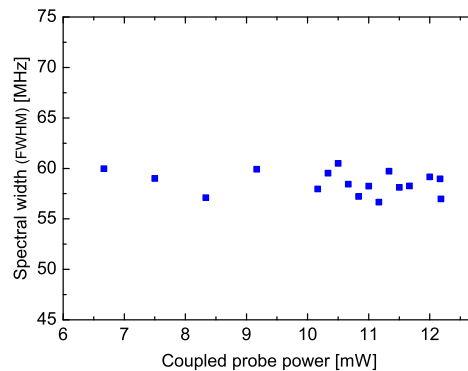


**Figure 6.3:** Brillouin spectral width of the step-index fiber for different probe power.

At a larger seed power of 1.25 W coupled into the fiber core a Lorentzian shaped Brillouin spectrum with a significantly smaller bandwidth of 50 MHz (FWHM) was determined (Fig. 6.4). Large pump beam intensities can induce a stimulated Brillouin scattering pro-

cess and results in gain narrowing of the detected Brillouin spectra. Decreasing the coupled seed power resulted in broadening of the spectral width up to 59 MHz detected at 25 mW (Fig. 6.5). At seed power lower than 100 mW the process of spectral narrowing showed saturation. With an exponential fit of the obtained data the step-index fiber spontaneous Brillouin gain bandwidth at zero seed power was estimated with  $\Delta\nu_B = 59 \pm 1$  MHz.

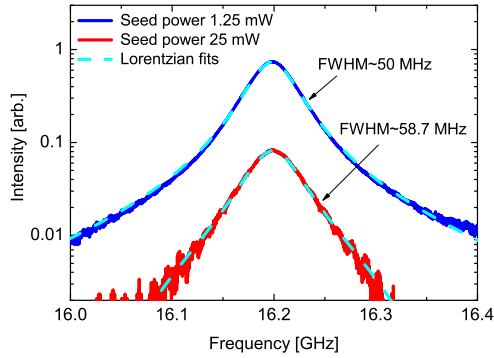


**Figure 6.4:** Brillouin gain profiles of the step-index fiber measured with the pump-and-probe technique.

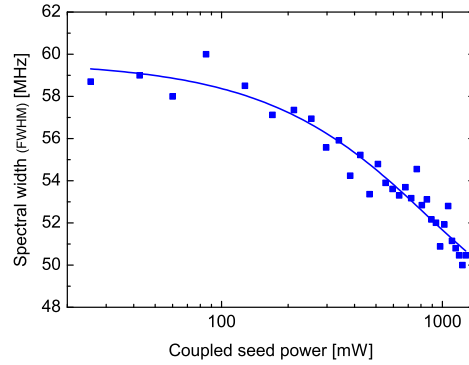


**Figure 6.5:** Spectral width of the step-index fiber Brillouin gain profiles with respect to the coupled seed power.

The Brillouin gain spectra were recorded with a signal and probe polarization oriented to the same birefringent axis of the polarization maintaining (PM) fiber. For a fixed signal and a rotating probe polarization the Brillouin gain decreased to zero for perpendicular ( $90^\circ$  rotation) probe polarization (Fig. 6.6).

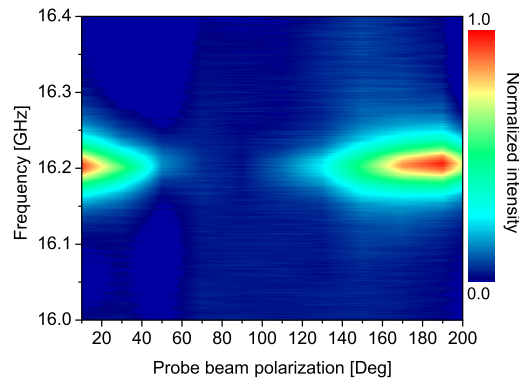


**Figure 6.6:** Brillouin scattering gain profiles of step-index fiber measured with fixed signal and rotating probe polarization.

These results are consistent with theoretical evaluations on polarization properties of Brillouin scattering in passive single-mode fibers published by van Deventer et al. [41]. For this reason, Brillouin scattering generated in a PM fiber amplifier is mostly polarized parallel to the signal polarization.

Theoretically, the data obtained from the pump-and-probe experiment would allow for a determination of the Brillouin gain value  $g_{B_0}$  with Eq. (3.25) solved for  $g_B(\nu_B)$ . However, high transmission losses strongly effect the detected probe intensity and prevented a reliable evaluation. Transmission losses for the seed and probe beams through the active fiber were in the range of 2.2 dB, mainly attributed to absorption by ytterbium ions. In the presence of an intense signal beam the transmitted probe power was almost doubled even detuned from the Brillouin gain maximum. This can be explained by a bleaching effect of the ytterbium ions by absorption of the signal radiation and amplification of the probe beam.

### Photonic crystal fiber

The pump-and-probe setup was also utilized to investigate the Brillouin gain spectrum of the ytterbium doped PCF. Similar to the spectrum observed from the step-index fiber a Lorentzian shaped profile was detected from the PCF around 16 GHz with a spectral width (FWHM) of approximately 56 MHz (Fig. 6.7). A second weaker Brillouin gain peak was

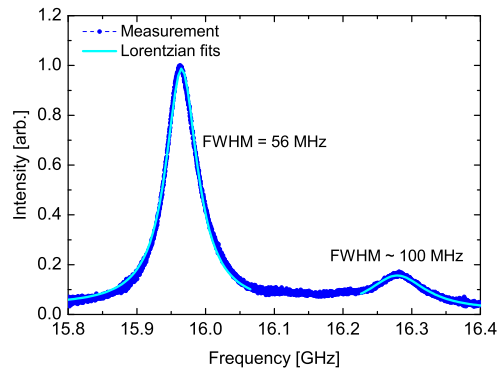


**Figure 6.7:** Brillouin gain profile of the PCF measured with the pump-and-probe technique at 1.25 W coupled seed power.

detected with a spectral width of  $\approx 100$  MHz separated by 320 MHz from the main peak. Similar observation have been made by Zou et al. [77] in pump-and-probe experiments performed on a germanium doped passive PCF, where several higher order longitudinal acoustic modes were discovered besides the main lowest order fiber core acoustic mode.

In order to make sure that no spectral narrowing was induced by large signal (pump) intensities, as has been observed for the step-index fiber, Brillouin gain spectra were recorded at different signal power and the spectral width of the main Brillouin peak was determined (Fig. 6.8). The Brillouin spectral width was nearly constant with respect to

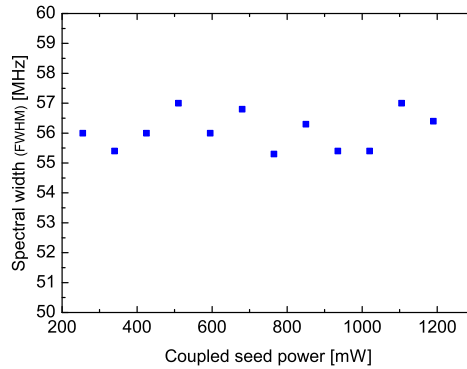


**Figure 6.8:** Spectral width of the main PCF Brillouin gain peak at different coupled seed power.

the injected pump power. The average spectral width of the PCF spontaneous Brillouin gain profile was estimated to be  $56 \pm 1$  MHz. During these measurements the injected probe power was kept at approximately 10 mW. Changing the probe beam power did not induce any distortions to the detected Brillouin gain spectra.

## 6.2 Backscattered power

The most common way for the detection of SBS is performed by measuring the scattered light power propagating in the backward direction with respect to the signal radiation. Depletion of signal power through SBS limits the maximum power in narrow-linewidth fiber systems. The SBS threshold in passive fibers has been variously defined as the input power at which the backscattered power equals the input power [22], the backscattered power equals the transmitted power [78] or the backscattered power equals 1% of the input power [79]. For fiber amplifier systems the threshold is mostly defined as the output power at which the backscattered power begins to increase rapidly or, equivalently, the signal wave begins to be significantly depleted [80]. During fiber amplification the backward propagating light being reflected from a partially reflecting mirror (PR) with  $R=10\%$  at 1064 nm was detected with a power meter.

### Step-index fiber

A nonlinear increase of the backward propagating light from the step-index fiber amplifier was observed at 85 W in counter- and 32 W of output power in co-pumped configuration (Fig. 6.9). This Brillouin power increase ultimately limited the maximum output power of the step-index fiber amplifier system. At further increased pump power chaotic SBS damaged the fiber cores at both ends.

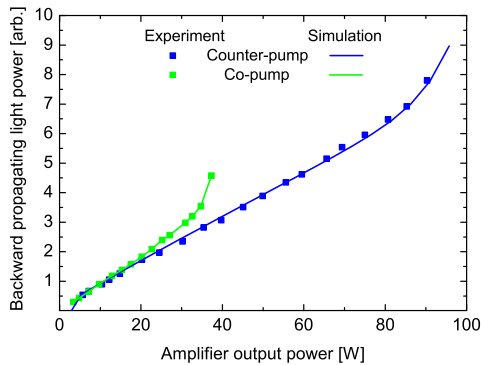


**Figure 6.9:** Experimental and theoretical backward light power with respect to step-index fiber amplifier output power.

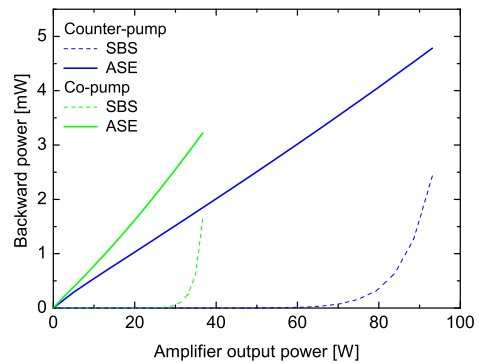


**Figure 6.10:** Simulated ASE and SBS power at different step-index fiber amplifier output power.

In order to obtain conformity between experimental and theoretical results for the evolution of backward SBS and ASE power the Brillouin gain value  $g_{B_0}$  needed to be set to  $2.4 \cdot 10^{-11}$  m/W which is in range of typical values reported for passive fused silica fibers [42]. For active large mode-area fibers no values have been found in the literature and a determination with the pump-and-probe measurement was not possible. With this value simulations of the SBS thresholds for the step-index fiber amplifier in counter- and co-pumped configuration showed an excellent agreement with the experimental data (Fig. 6.9). In principle, Brillouin scattering shows an exponential power increase over the whole amplifier power range. Once its contribution is in the range of the backward propagating ASE power ( $P_{ase}^b$ ), it is recognized as SBS (Fig. 6.10). Therefore an accurate simulation of the ASE power is necessary to compare the experimentally and theoretically determined SBS thresholds. A more comprehensive model would also involve Rayleigh backscattering. Due to the relatively weak contribution to the backward power compared to ASE, Rayleigh scattering was not considered in the present numerical model [81].

The threshold dependence on the amplifier pump configuration results from different gain, signal and temperature distributions along the active fiber (Fig. 6.11). In co-pumped configuration the seed signal experiences high amplifier gain in the first half of the active fiber, which rapidly increases the signal power to a critical level to generate SBS. A counter-pumped amplifier shows maximum gain in the rear part and the signal power smoothly grows with an exponential progression. For the step-index fiber amplifier operated at 52 W of launched pump power this characteristic results in a two times higher signal power density integrated over the amplifier fiber length for a co- (183 W·m) compared to a counter-pumped (88 W·m) amplifier. Laser gain in the first part of the fiber additionally amplifies Brillouin scattered radiation.

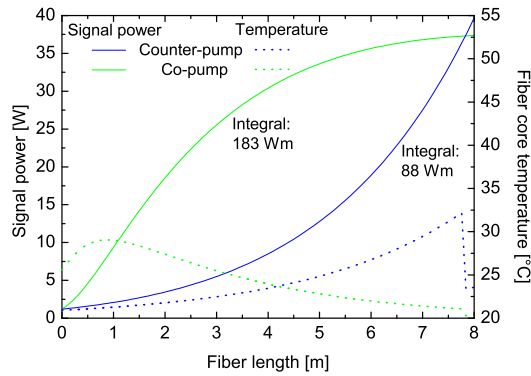


**Figure 6.11:** Simulated signal power and temperature distribution along step-index fiber amplifier at 52 W of pump power.

Another reason for the different SBS thresholds are pump light induced temperature gradients  $\Delta T$  in the rear part of the active fiber, where most of the SBS is generated owing to high signal intensities (Fig. 6.11). In co-pumped configuration most of the pump light is absorbed in the first part and only small temperature gradients are present in the back. As a result the temperature induced Brillouin frequency shift is comparably small over the last two meters of the fiber with  $\Delta T \approx 1\text{-}2^\circ\text{C}$  corresponding to a frequency shift of 2-4 MHz with a Brillouin temperature shift coefficient  $c_f$  in the range of 2 MHz/K. The counter-pumped amplifier exhibits a  $\Delta T > 5^\circ\text{C}$  resulting from high pump power in the rear fiber section. The corresponding Brillouin frequency shift of more than 10 MHz decreases the effective Brillouin gain. An additional temperature change is induced by the active cooling of the fiber that was applied from  $z = 7.85\text{-}8\text{ m}$  with a V-grooved copper holder.

Notably, the temperature distribution in co-pumped configuration shows an increase of the temperature in the first part of the fiber at  $z = 0-0.5$  m. In this section high inversion levels of up to 30% excited ions reduce the pump light absorption and consequently the fiber core temperature being proportional to the absorbed pump light is decreased as well (Fig. 5.3).

Simulations of the Brillouin scattering power with respect to the amplifier fiber length reveal the strong dependence of the amplifier pump configuration on the Brillouin scattering power distribution (Fig. 6.12). The Brillouin power is plotted for maximum amplifier output power of 35 W in co- and 92 W in counter-pumped configuration. In counter-pumped

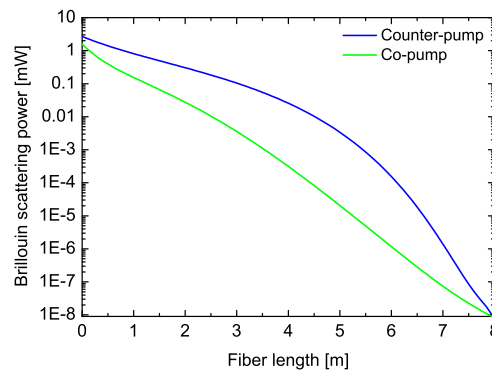


**Figure 6.12:** Simulated Brillouin scattering power along step-index fiber at 35 W and 92 W of amplifier output power in co- and counter-pumped configuration.

configuration with an exponential signal increase along the fiber most of the Brillouin power is generated in the rear part of the fiber. For the co-pumped configuration the Brillouin power shows an almost constant exponential increase over the entire fiber length.

The approximate solution for the SBS threshold in passive fibers given by Eq. (3.26) for an almost constant signal power distribution results in a threshold power of 29 W for the step-index fiber. This result almost coincides with the SBS threshold of the co-pumped fiber amplifier.

### Photonic crystal fiber

Backward propagating light power from the PCF was detected during amplifier operation. At output power lower than 110 W a linear increase with respect to the amplifier power was observed. Towards higher output power the backward power showed a small deviation

from this linear progression. However, the observed power increase did not result from SBS, where once present a rapid growths of backward power would be expected towards higher amplifier output power. A reason for this effect might be a nonlinear increase of the ASE power induced by a decreased saturation level of the fiber amplifier at higher pump power. This effect was more pronounced in the simulations of the backward propagating

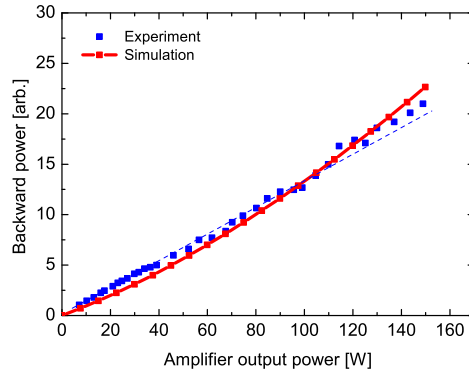


**Figure 6.13:** Experimental and simulated backward power from PCF amplifier with respect the amplifier output power.

light power, where an exponential increase with respect to the amplifier output power over the whole power range was observed (Fig. 6.13). For these simulations the Brillouin gain was set to  $2.4 \cdot 10^{-11}$  m/W as before for the step-index fiber. The simulated Brillouin scattering was well suppressed with only several ten nW compared to the ASE power in the mW range. Depending on the amplifier configuration and fiber design the ASE power increase deviates from a linear progression. This characteristic is mainly attributed to amplifier saturation effects and need to be considered for a detection of SBS in high-power fiber amplifiers by monitoring the backward light power.

### 6.3 Intensity noise

Besides the depletion of signal radiation SBS induces broadband intensity noise of the amplifier output beam in the kHz and MHz frequency range, which is one of the main impairments in narrow-linewidth fiber optical communication systems [22]. For laser applications with low-noise requirements, such as gravitational-wave detectors [12], this effect would also represent the most stringent limitation. Monitoring the fiber amplifier output relative intensity noise (RIN) can also be utilized for a sensitive SBS detection. There



have been many theories about the dynamics of SBS and the associated signal noise:

Since SBS in optical fibers arises from thermal fluctuations, the noise can be attributed to stochastic dynamics in the signal depletion process [59, 82].

A different explanation is the coupling of phase to intensity noise. In the presence of significant SBS gain and power a corresponding loss spectrum appears at the signal frequency (Fig. 6.14). Associated with this gain/loss spectrum is a nonlinear refractive index or phase

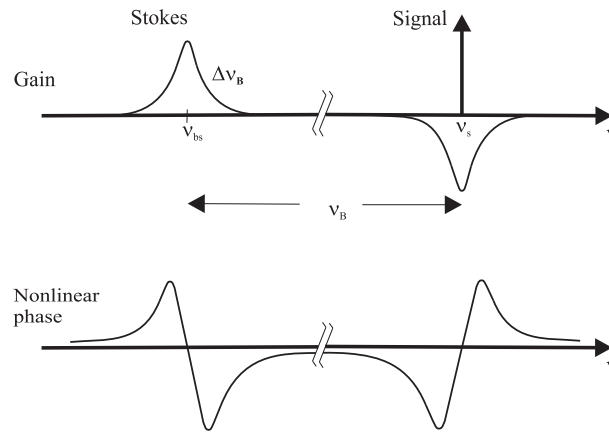


**Figure 6.14:** SBS gain and loss spectrum and the resulting nonlinear phase shift [83].

change, which has been verified experimentally by Loayssae et al. [84] and theoretically described by Peral et al. [85]. As a result phase noise of the laser source is converted to intensity noise. This effect has been verified with signal sources having different intensity and phase noise properties by Zhang et al. [83, 86].

The signal intensity noise has also been attributed to photons that undergo two scattering processes [87]. The first one is stimulated Brillouin scattering that generates backscattered photons at different positions along the fiber and different frequencies distributed over the Brillouin scattering spectrum. The second one is spontaneous anti-Stokes Brillouin scattering that generates photons with frequencies increased by the Brillouin shift. Each scattering process inverts the photon propagation direction. Although the number of these photons is small the interference with the strong seed signal can induce significant intensity noise.

Clear evidence for the onset of SBS is therefore given by the increase of relative intensity noise (RIN) in the MHz frequency range. In the kHz frequency range mainly pump power fluctuations contribute to the amplifier excess noise. At frequencies above the inverse effective lifetime of the ytterbium doped fiber, pump noise is low pass filtered [88]. For a fiber

amplifier system with a sufficient suppression of ASE and the associated noise sources, such as ASE-ASE and ASE-signal beat noise, the amplifier and seed signal noise are basically equivalent. In the frequency range above 6 MHz the NPRO and fiber amplifier output noise was shot noise limited for a detection photocurrent of 3 mA, corresponding to a RIN of -159.7 dB/Hz. This characteristic allows for a sensitive investigation of SBS induced amplifier excess noise.

### Step-index fiber

The RIN of the step-index fiber amplifier output was monitored with a low-noise photodiode connected to an electronic spectrum analyzer (ESA) (Fig. 6.15). The detected beam was attenuated to keep a constant photocurrent of 3 mA. For comparison the RIN of the unamplified NPRO was determined with an identical photocurrent.

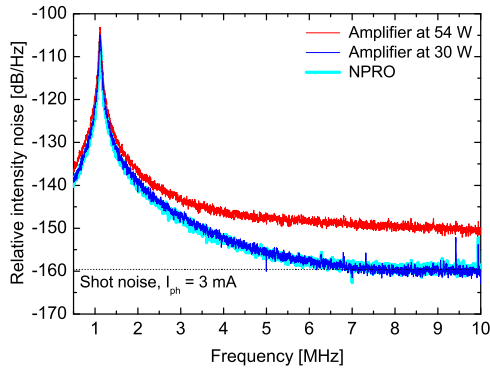


**Figure 6.15:** Relative intensity noise spectrum of the NPRO and counter-pumped step-index fiber amplifier output.

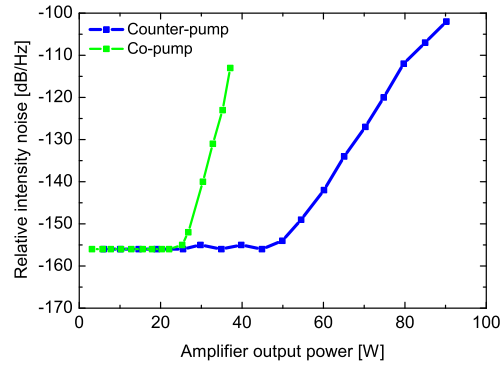


**Figure 6.16:** Relative intensity noise at 5 MHz with respect to the step-index fiber amplifier output power.

An exponential increase of RIN at 5 MHz was observed at amplifier output power larger than 52 W in counter- and 25 W in co-pumped configuration (Fig. 6.16). Compared to the threshold power that have been determined by monitoring the backward light power, SBS induced influences on the amplifier intensity noise appeared at 1.4-1.6 times lower output power. Hence, the detection of RIN of the amplifier output beam can be used for a sensitive detection of SBS.

### Photonic crystal fiber

RIN spectra of the PCF amplifier were recorded in the frequency range from 500 kHz to 10 MHz (Fig. 6.17). For all optical power the photodetector current was kept constant at 3 mA. The fiber amplifier did not show any excess noise in the detected frequency range up to the maximum output power of 148 W, indicating an SBS free operation.

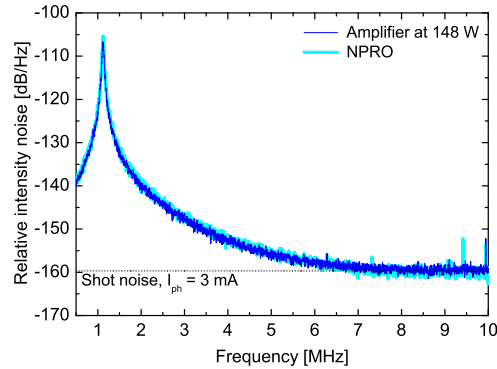


**Figure 6.17:** Relative intensity noise spectrum of the NPRO and PCF amplifier at 148 W of output power.

## 6.4 Optical spectrum

As has been described in Section 3.1 the Brillouin frequency shift in a fused silica fiber generated by a narrow-linewidth signal at 1064 nm is in the range of  $\nu_B \approx 16.2$  GHz, corresponding to a wavelength shift of  $\approx 0.06$  nm. Such a wavelength shift can be detected with an optical spectrum analyzer (OSA) and the growth of Brillouin scattering in backward propagating light from a fiber amplifier can be investigated. The detection sensitivity is restricted to optical noise from ASE and the resolution of the OSA.

### Step-index fiber

Optical spectra of backward propagating light from the step-index fiber amplifier showed a peak at 1064.12 nm resulting from Rayleigh-scattered and back-reflected seed radiation (Fig. 6.18). For high signal intensities a second peak evolved shifted by approximately 0.06 nm at 1064.18 nm. In counter-pumped configuration the detection limit for Brillouin scattered radiation was at approximately 40 W of amplifier output power and at 12-13 W

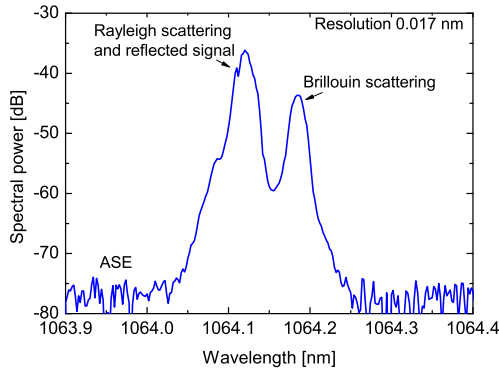


**Figure 6.18:** Optical spectrum of backwards reflected, Rayleigh and Brillouin scattered light from step-index fiber amplifier.

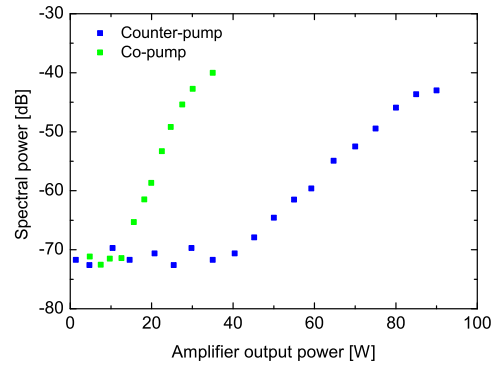


**Figure 6.19:** Spectral power at Brillouin wavelength with respect to the step-index fiber amplifier output power.

for the co-pumped fiber amplifier. At larger amplifier output power an exponential increase of the spectral power at the Brillouin frequency was observed (Fig. 6.19).

A minimum effective resolution bandwidth of 0.017 nm was determined at 3 dB of a sample spectrum taken from the NPRO. However, with a signal intensity range of 30-40 dB the resolution is significantly reduced up to 0.1 nm and limits the Brillouin scattering detection sensitivity.

This detection method does not allow for an investigation of the Brillouin spectral shape due to the limited OSA resolution bandwidth. Although sometimes applied to qualitatively analyze SBS influences in different high-power fiber amplifiers no distinction between spontaneous and stimulated Brillouin scattering can be made [29]. For a more accurate Brillouin scattering spectral detection with higher resolution a heterodyne scheme is presented in Section 6.5.

### Photonic crystal fiber

The optical spectra of the backward propagating light were also recorded during amplifier operation with the PCF. Even at maximum amplifier output power of 148 W the optical spectra did not show a significant increase of the spectral power in the wavelength range expected for Brillouin scattering (Fig. 6.20). The same optical spectrum analyzer with an effective resolution bandwidth of 0.017 nm was used for Brillouin scattering detection in the step-index fiber amplifier system. With a similar signal to ASE noise ratio for both

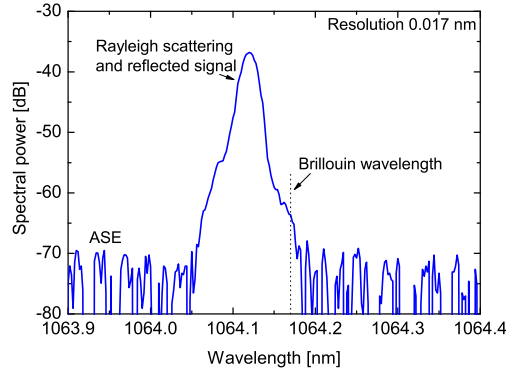


**Figure 6.20:** Optical spectrum of backward propagating light from PCF amplifier at 148 W of output power.

amplifier setups the detection sensitivity for Brillouin scattering was nearly identical. The reason that no Brillouin scattered light was detected in the PCF amplifier system was attributed to the low Brillouin scattering power. Simulations at amplifier output power above the respective limits of detection for the step-index amplifier revealed Brillouin scattering power of  $> 100$  nW. For the PCF amplifier the simulated backscattered light power was still below 100 nW at the maximum amplifier output power of 148 W.

## 6.5 Heterodyne detection

With a heterodyne detection scheme the optical spectrum can be transferred to an electronic signal and more accurately resolved. A similar experimental approach has been applied to detect Brillouin scattering spectra from passive single-mode fibers excited at 1550 nm by Yeniay et al. [89].

### Step-index fiber

Beat signals between Brillouin scattered light from the step-index fiber amplifier and a fraction of the narrow-linewidth NPRO seed radiation were detected with a fast photodetector (Model 1414, New Focus [90]) and an electronic spectrum analyzer (ESA) (E4440A, Agilent [91]). At an amplifier output power of 56 W in counter-pumped configuration a heterodyne signal of the Brillouin spectrum at 16.27 GHz with a spectral width of 19 MHz (FWHM) was observed (Fig. 6.22).

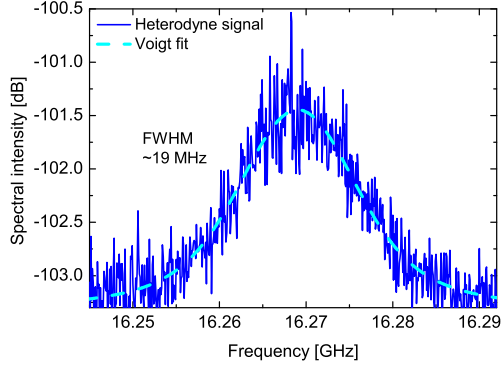


**Figure 6.21:** Direct heterodyne detection of Brillouin scattering spectra from counter-pumped step-index fiber amplifier at 56 W.

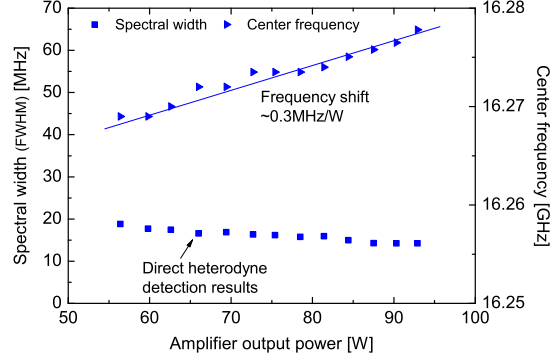


**Figure 6.22:** Determination of Brillouin spectral width with from pump/probe measurements and direct detection.

Towards higher output power the spectra showed a shift of the center frequency by approximately 0.3 MHz per 1 W of launched pump power induced by absorptive heat load (Fig. 6.22). The spectral width (FWHM) decreased from 19 MHz determined at 56 W down to 15 MHz at the maximum amplifier output power of 92 W. Due to intense noise of the photodetector, which was specified with a noise equivalent power of  $30 \text{ pW}/\sqrt{\text{Hz}}$ , the Brillouin scattering spectra could only be detected at relatively high power levels and close to the threshold of SBS.

In order to improve the sensitivity of the heterodyne detection system and enable an investigation in the regime of spontaneous Brillouin scattering different measures have been taken (Fig. 6.23). Backward propagating light from the fiber amplifier was passed through an interference filter (IF) with 10 nm transmission bandwidth at 1064 nm to lower the ASE power on the photodiode. The filtered light was then amplified by a maximum of  $\approx 7 \text{ dB}$  using a second ytterbium doped fiber amplifier ( $300 \mu\text{m}$  cladding and  $5 \mu\text{m}$  core diameter). At these low amplifier gain values and low seed signal saturation no measurable effects on the spectral shape or width of the Brillouin spectra have been detected. In front of the amplifier a Faraday isolator was placed to prevent light coupling back into the main amplifier. With a second NPRO, frequency tuned close to the Brillouin frequency, a heterodyne detection with an InGaAs photodetector with 10 GHz bandwidth and a noise equivalent power of less than  $0.04 \text{ pW}/\sqrt{\text{Hz}}$  (ET-3500, EOT [92]) around 1-2 GHz was performed. The ESA was set to a resolution bandwidth of 200 kHz, sweep time of 50 ms and 100 times averaging.

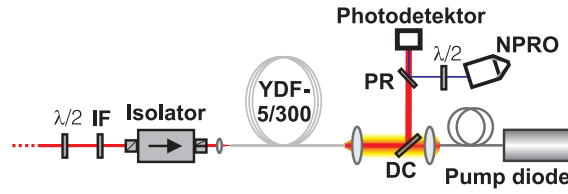


**Figure 6.23:** Heterodyne system for detection of Brillouin scattering spectra. PR partially reflective mirror (R=10%), IF interference filter.

With a specified long term frequency stability of 1 MHz per minute the NPRO did not introduce measurable distortions to the detected spectra. Compared to the Brillouin spectral bandwidth in the MHz range the specified NPRO emission linewidth of 1 kHz per 100 ms is sufficiently narrow to neglect its influence on the detected heterodyne spectra.

The heterodyne detection system using an additional NPRO as a local oscillator allowed for an investigation of Brillouin scattering spectra almost over the entire amplifier power range. Similar to the Brillouin gain spectra that have been detected during pump-and-probe experiments the Brillouin spectra showed a Lorentzian shape at low signal intensities. At an amplifier output power of 5.7 W a bandwidth (FWHM) of 40 MHz was determined with a Lorentzian fit of the heterodyne spectrum (Fig. 6.24). At amplifier output

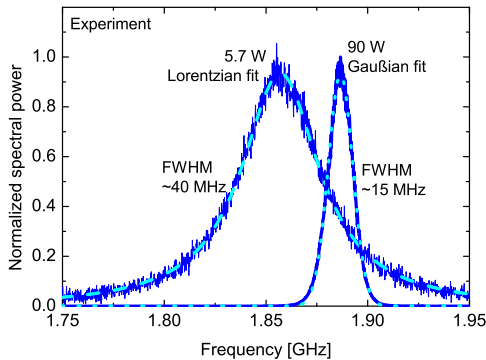


**Figure 6.24:** Heterodyne detection of Brillouin scattering spectra from counter-pumped step-index fiber amplifier.

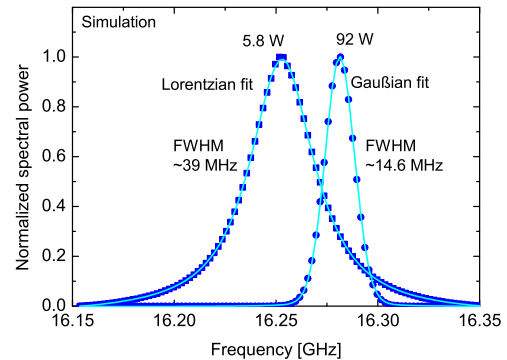


**Figure 6.25:** Simulation of Brillouin scattering spectra from counter-pumped step-index fiber amplifier.

power lower than 3-5 W the ratio between detection noise and heterodyne signal did not allow for an accurate evaluation of the spectral shape anymore. With increasing output power a spectral gain narrowing process was observed starting from 59 MHz bandwidth, detected with the pump-and-probe technique at low signal intensities, down to 15 MHz

for the counter- and 13.5 MHz for co-pumped fiber amplifier configuration at maximum output power (Fig. 6.26).

Simulations of the Brillouin spectra at different output power of the step-index fiber amplifier showed very similar progressions and spectral gain narrowing from Lorentzian to Gaussian shaped profiles (Fig. 6.25 and 6.26). These simulations were carried out with a number  $i = 100$  of spectral Brillouin scattered lines ( $P_{bs_i}$ ) distributed over a frequency range of 200 MHz (calculation linewidth  $\Delta\nu_{bs} = 2$  MHz). This spectral resolution was sufficient to get accurate results for the spectral width and integrated Brillouin power.

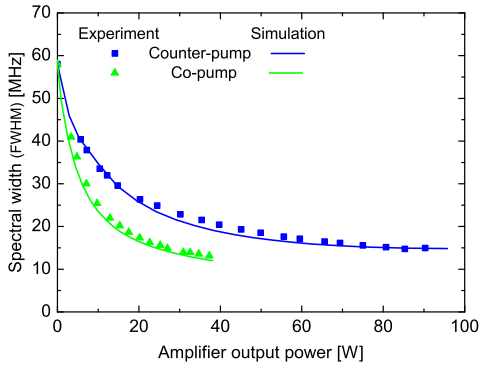


**Figure 6.26:** Experimental and theoretical evolution of Brillouin spectral width with step-index fiber amplifier output power.

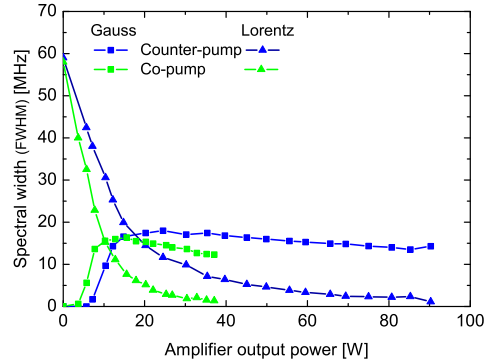


**Figure 6.27:** Gauss and Lorentz contribution to Voigt profile fit of the step-index fiber Brillouin scattering spectra.

At intermediate power levels the spectral width was determined with a Voigt profile fit to the experimentally and theoretically obtained data. Voigt profiles are commonly used in spectroscopy for spectral lines that exhibit two broadening mechanisms with a Gaussian and a Lorentzian profile. Mathematically it represents a convolution of these two profiles. An approximation of the spectral width is given by [93]

$$\Delta\nu_{\text{Voigt}} = 0.5346 \cdot \Delta\nu_{\text{Lor}} + \sqrt{0.2166 \cdot \Delta\nu_{\text{Lor}}^2 + \Delta\nu_{\text{Gau}}^2} \quad (6.1)$$

The observed spectral narrowing process of the Brillouin spectra was accompanied by such a transition from Lorentzian to Gaussian profiles (see Figs. 6.24 and 6.25). At low signal intensities the Brillouin spectra were purely Lorentzian. In the regime of SBS the Lorentzian contribution to the Voigt profile was decreased below one MHz and the spectra became purely Gaussian (Fig. 6.27).

For both amplifier pump configurations a saturation of the spectral narrowing process



was observed, which results from signal depletion induced by SBS. This characteristic represents a transition from spontaneous to pure stimulated Brillouin scattering. Studies on the evolution of Brillouin spectra in passive single-mode fibers published in Ref. [59, 89] show very similar spectral characteristics compared to the one observed here from a high-power step-index fiber amplifier, indicating that spectral distortions induced by thermal gradients are still relatively weak.

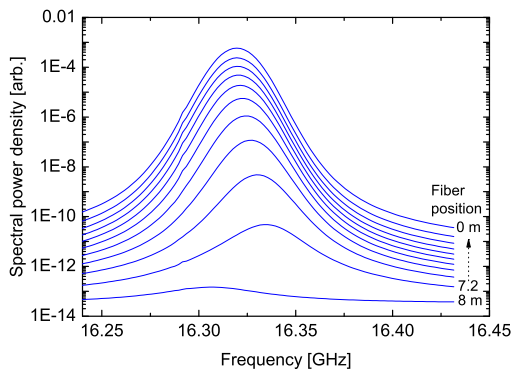


**Figure 6.28:** Simulation of Brillouin spectral evolution along the step-index fiber at 92 W in counter-pumped configuration.

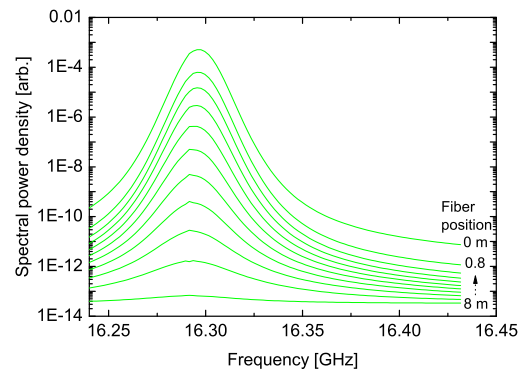


**Figure 6.29:** Simulation of Brillouin spectral evolution along the step-index fiber at 35 W in co-pumped configuration.

Besides the comparison of the simulated Brillouin scattering spectral and power evolution with the obtained experimental results, the rate-equation model allows for an investigation of these characteristics along the entire active fiber and local influences such as fiber temperature gradients can be accurately identified. Simulations of Brillouin spectra of the step-index fiber amplifier at 92 W of output power in counter-pumped and 35 W in co-pumped configuration are shown in Figs. 6.28 and 6.29 for different fiber positions from  $z = 0$ -8 m (0.8 m step size).

As has been discussed in Section 6.2 (Fig. 6.11), in co-pumped configuration the temperature induced frequency shifts are relatively small and the Brillouin scattering spectrum evolves basically at a constant center frequency over the entire fiber length (Fig. 6.29).

At a higher pump power of 125 W in counter-pumped configuration the simulated Brillouin spectra show a significant frequency shift up to 16.33 GHz in the rear part of the fiber at  $z = 7.2$  m (Fig. 6.28). With decreasing fiber core temperatures at  $z < 7.2$  m the center frequency is down shifted to 16.32 GHz. At sections where the fiber was effectively cooled with a copper holder ( $z = 7.85$ -8 m), the center frequency of the Brillouin spectrum remains at 16.31 GHz.

### Photonic crystal fiber

Heterodyne spectra of Brillouin scattered light were also recorded during operation of the PCF amplifier (Fig. 6.30). Compared to the step-index fiber amplifier a different evolution of the Brillouin scattering spectra was observed. As a result of lower Brillouin scattering

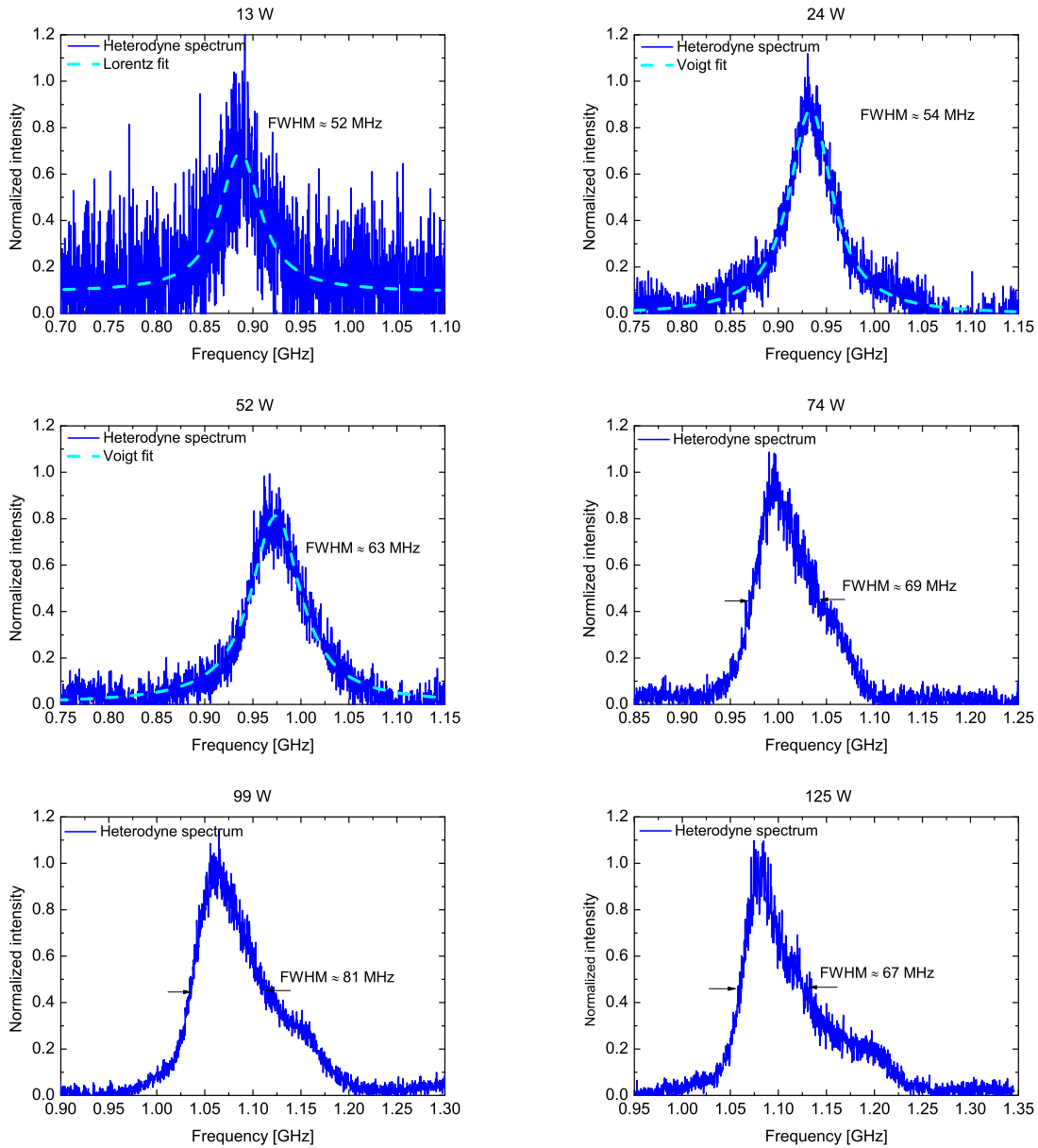


**Figure 6.30:** Brillouin scattering spectra from PCF amplifier at different output power.

power levels the detection limit of the heterodyne system was at approximately 13 W of amplifier output power. At this power a Lorentzian shaped Brillouin spectrum with a width (FWHM) of 52 MHz was recorded. This is a slight reduction compared to the

width of the spontaneous gain profile of 56 MHz. The second Brillouin gain peak that was observed with the pump-and-probe technique was apparently significantly suppressed compared to the main peak and could not be resolved with the heterodyne system. Already at 24 W of amplifier output power the pump light induced temperature gradients and the associated Brillouin frequency shift started to broaden the spectra. At power levels above 70 W an additional deformation of the spectral shape towards higher frequencies was observed.

The simulations of the Brillouin scattering spectral evolution and the temperature distribution along the PCF show the origin of these deformations (Fig. 6.31 and 6.32). In the

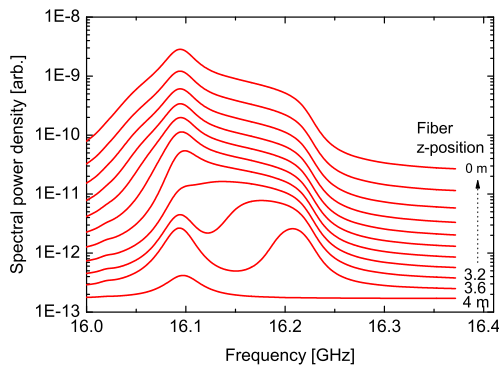


**Figure 6.31:** Simulated evolution of Brillouin scattering spectrum along the PCF amplifier at 148 W of output power.

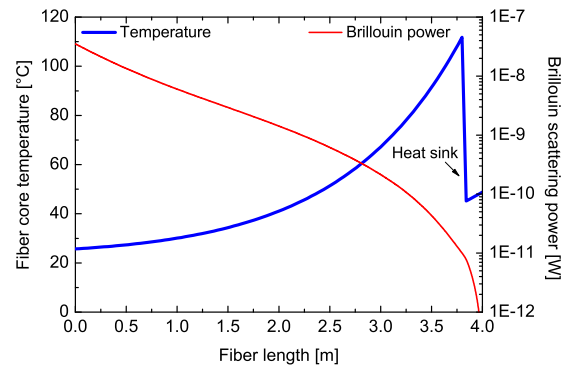


**Figure 6.32:** Simulated temperature and Brillouin power distribution along the PCF amplifier at 148 W of output power.

rear part ( $z = 3.85\text{--}4\text{ m}$ ) the PCF was effectively cooled with a V-grooved copper holder and stayed in the range of  $50^\circ\text{C}$ . Even though the cooled fiber section was only 15 cm long, the frequency components of the Brillouin scattered light generated in this section at  $\approx 16.1\text{ GHz}$  contribute the major part to the total Brillouin scattered power. In the region behind the copper holder ( $z < 3.85\text{ m}$ ), where no active cooling was applied the temperature rises above  $100^\circ\text{C}$  and frequency components shifted by more than 100 MHz around 16.2 GHz are generated.

To illustrate the effect of the cooled section on the Brillouin spectra, simulations with and without a cooled fiber section at 148 W of output power are plotted in Fig. 6.33 together with the experimental results obtained from heterodyne detection. As a result of cooling and a small temperature gradient the main Brillouin peak showed only little deformations even at high power levels. An uncooled fiber would have resulted in a much broader and more homogeneous Brillouin spectrum.

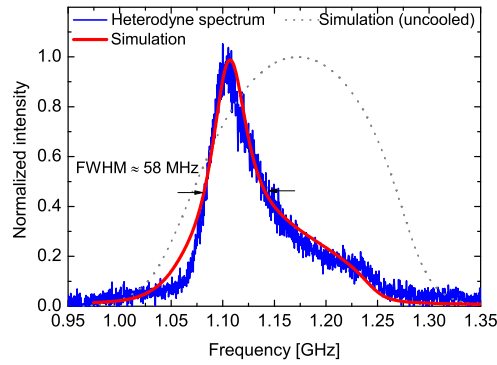


**Figure 6.33:** Simulation and experimental detection of Brillouin scattering spectrum of PCF amplifier at 148 W of output power.

In Fig. 6.34 the simulated spectral evolution of the Brillouin scattering spectra with respect to the amplifier output power is plotted. A number of  $i = 100$  spectral lines was used, corresponding to a calculation resolution of  $\Delta\nu_{\text{bs}} = 5$  MHz. Similar to the experimental heterodyne detection, the Brillouin spectra showed a temperature induced spectral broadening towards higher frequency at amplifier output power larger than 60 W. The main Brillouin peak is shifted from approximately 16 GHz up to 16.07 GHz. This frequency shift is due to the temperature increase to  $\approx 50^\circ\text{C}$  in the cooled fiber end section at maximum pump power.

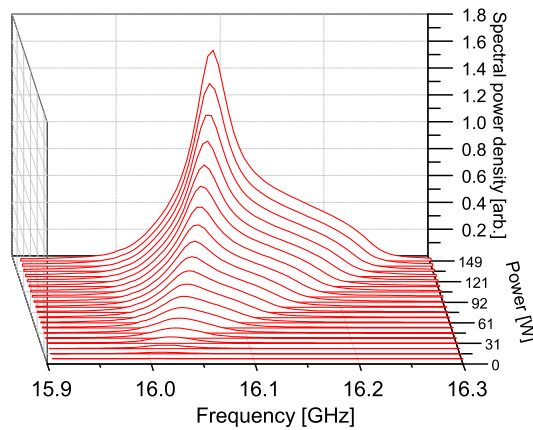


**Figure 6.34:** Simulated Brillouin scattering spectra with respect to PCF amplifier output power. Calculation resolution  $\Delta\nu_{\text{bs}} = 5$  MHz.

---

In counter-pumped configuration the PCF amplifier can theoretically be operated below the SBS threshold at higher power level owing to the short fiber length of only 4 m and strong pump induced temperature gradients along the fiber that broaden the Brillouin scattering spectra and lower the effective Brillouin gain. However, without an active cooling arrangement over the entire fiber length the peak temperature will rise above 200°C at launched pump power larger than 350 W, where thermal effects such as refractive index variations, re-absorption and stress will start to degrade the amplifier performance and at a certain point damage the fiber [55]. With an active cooling of the fiber with a heat transfer coefficient of  $h = 500\text{-}1000\text{ W/m}^2\text{K}$  the fiber core temperature would be effectively reduced and still an SBS free operation with several hundred watts of output power is possible. The pump cladding with a relatively small diameter of 225  $\mu\text{m}$ , but large numerical aperture of 0.62 will finally limit the maximum pump power that can be launched into the PCF.



## 7. SBS suppression

For an SBS free narrow-linewidth signal propagation and amplification through optical fibers different suppression techniques besides the previously described pump light induced temperature gradients can be applied. In this chapter considerations on possible advances for the suppression of SBS in high-power fiber amplifiers are presented.

The shape and center frequency of Brillouin spectra and the peak Brillouin gain can be manipulated by using different doping materials, inhomogeneous doping distributions [32], fiber designs that support multiple acoustic modes [89] and external influences such as applied temperature and strain variations [94, 95]. Taking advantage of these influences, techniques have been developed to control SBS first in passive single-mode fibers and later in active LMA fibers. A variation of the Brillouin scattering center frequency along the fiber effectively lowers the overall Brillouin gain and is the most prominent approach to increase the SBS threshold power. For two suppression schemes comprising an active temperature and strain variation along the fiber experimental and theoretical investigations are presented in this chapter.

Obviously large fiber cores also reduce the signal intensities mitigating optical nonlinearities and enable a further scaling to higher output power. Novel fiber designs allow for large mode field diameters with maintained single transverse-mode operation. For one particular large-core active fiber numerical simulations are presented in this chapter to demonstrate the theoretical capability of such fiber amplifier systems to be operated with more to 1 kW of output power with well suppressed SBS.

## 7.1 Strain

One way to influence the acoustic velocity and thus the Brillouin frequency shift in fused silica glasses is to apply compressive or tensile strain. The acoustic velocity can be expressed by

$$v_a = \sqrt{\frac{E(1 - \kappa)}{(1 + \kappa)(1 - 2\kappa)\rho_0}} \quad (7.1)$$

where  $\rho_0$  is the material density and  $E$  the Young's modulus

$$E = \frac{\sigma}{\epsilon} = \frac{F/A_0}{\Delta L/L} \quad (7.2)$$

defined by the ratio of mechanical stress  $\sigma$  and the strain  $\epsilon$  [95].  $F$  is the mechanical force,  $A_0$  the original cross-sectional area and  $\Delta L/L$  is the relative elongation or compression. Poisson's ratio  $\kappa$  defines the ratio of transverse  $\epsilon_x$  and axial  $\epsilon_y$  strain with opposite negative and positive signs for axial tension and axial compression.

$$\kappa = -\frac{\epsilon_x}{\epsilon_y} \quad (7.3)$$

In the past there have been many publications on the application of strain in passive single-mode fibers to actively suppress SBS in telecommunication networks. With a special strain holding unit Yoshizawa et al. [96, 97] achieved a broadening of the Brillouin scattering gain spectrum from 50 MHz to 400 MHz and a resulting SBS threshold suppression of more than 7 dB.

Investigations on different strain distributions along the fiber with stair-ramp and triangular-periodic forms were performed by Chavez Boggio et al. [98] and resulted in up to 8 dB suppression of SBS. A frequency shift of the Brillouin spectrum with respect to the relative mechanical elongation of the fiber was determined to be 464 MHz/%. Even larger values have been reported by Niklès et al. [42] with 594.1 MHz/%.

In high-power amplifiers with rare-earth doped LMA fibers the suppression of SBS by applying strain turns out to be more difficult due to the size of the fibers and a significantly larger sensitivity of the fiber cores to macro-bending induced propagation losses. Lately, reports on the application of compressive strain on ytterbium doped LMA fibers showed remarkable results with 190 W of amplifier output power, however the authors did not mention the amplifier conversion efficiency [99].



### Investigations on SBS suppression by strain variation

For the investigation of strain influences on the SBS threshold in high-power fiber amplifiers experiments were performed. Similar to the experimental setup presented in Ref. [95] a section of the active fiber was coiled and clamped on a split metal spool separated by thread rods (Fig. 7.1). With two screw nuts the distance could be increased resulting in an elongation of the fiber in this section. For these experiments a different step-index fiber was used with a  $10\ \mu\text{m}$  core and  $400\ \mu\text{m}$  cladding diameter and a length of 25 m (PLMA-YDF-10/400, Nufern [53]). Four fiber windings were placed on the two spool pieces, which had a radius of 10 cm and were separated by 20 cm.

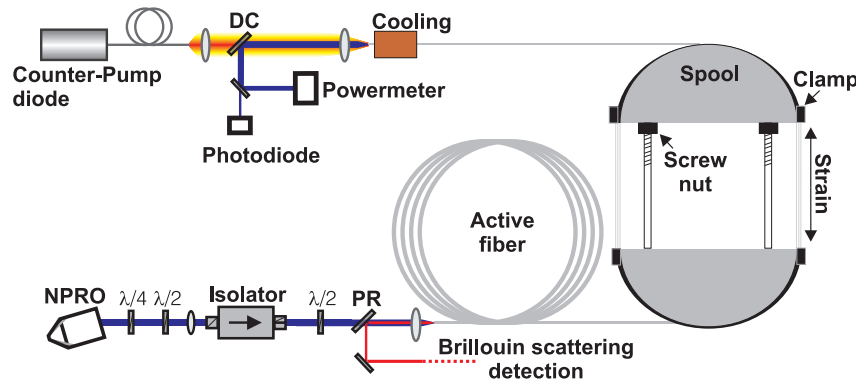


**Figure 7.1:** Experimental setup of the fiber amplifier with separated spools for a variable longitudinal strain.

First the fiber amplifier was operated without applying strain while heterodyne spectra of the Brillouin scattering, backward propagating light power and the amplifier relative intensity noise (RIN) at 5 MHz were detected (Fig. 7.2).

A rapid exponential increase of the backward power was observed at 9 W of amplifier output power indicating the onset of SBS. The amplifier RIN stayed constant around  $-156\ \text{dB/Hz}$  up to an amplifier output power of 7 W. At larger output power the RIN increased exponentially induced by SBS. Close to the SBS threshold at an amplifier output power of 5 W a Gaussian shaped Brillouin profile with a spectral width (FWHM) of 16 MHz was determined with the heterodyne detection system (Fig. 7.3).

The tension on the fiber sections was then increased by turning the screw nuts clockwise by  $360^\circ$  corresponding to an elongation of approximately 1 mm. This tensile strain resulted in a deformation of the Brillouin scattering spectra detected again at 5 W of amplifier output power. The main peak detected at 1.5 GHz was broadened to a width of  $\approx 21\ \text{MHz}$  most

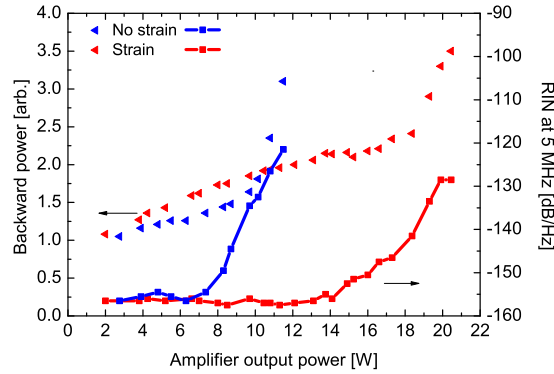


**Figure 7.2:** SBS thresholds of PLMA-YDF-10/400 step-index fiber with and without strain.

likely due to an overall decreased Brillouin gain and power. Additional frequency components were observed with lower intensities, homogeneously distributed up to 1.625 GHz. According to Ref. [42] a Brillouin frequency shift of  $594.1 \text{ MHz}/\epsilon$  is induced in single-mode fibers by tensile strain, where  $\epsilon = \Delta L/L$  is the fiber relative elongation in per cent. An estimate of the step-index fiber elongation resulted in a maximum elongation value of 0.2% (0.4 mm of 20 cm) with a frequency shift of 125 MHz. The homogeneously broadened Brillouin spectrum indicates that different parts of the active fiber were lengthened by different magnitudes.

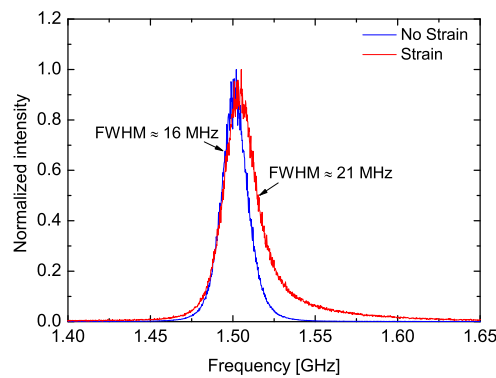


**Figure 7.3:** Heterodyne spectra of PLMA-YDF-10/400 step-index fiber amplifier at 5 W with and without strain.

With such a tensile strain applied to different sections of the step-index fiber the SBS threshold was increased by approximately 2 dB up to 18 W of amplifier output power, where the backward power started rising exponentially again (Fig. 7.2). The Brillouin intensity noise threshold was suppressed to an output power of 14 W.

These experiments show that tensile strain can be applied to effectively reduce parasitic effects of SBS in high-power fiber amplifier systems. However, a sophisticated mechanical fixture for the active fiber would need to be developed in order to get a long term stable amplifier setup. Especially in standard double-clad fibers, where pump light is guided with an outer polymer coating, any mechanical damage might seriously degrade the amplifier performance and long term stability. This concept is further limited by the maximum fiber elongation, which was found to be in the range of 0.8% or 1% for single-mode fibers [42, 98].

## 7.2 Temperature

Comprehensive studies on acoustic attenuation and the Brillouin frequency shift were carried out by Pine [94] for bulk fused quartz glasses and later by Niklès et al. [42] and Le Floch et al. [60] for optical fibers at temperatures ranging from 1.4-370 K. At room temperatures a linear temperature tuning coefficient  $c_f$  for the center Brillouin scattering frequency of 1.36 MHz/K was determined in fused silica fibers for a signal wavelength of 1300 nm.

Additionally, the Brillouin linewidth is influenced by temperature changes, but with a lower coefficient of  $c_b \approx -0.16$  MHz/K in the range of 300 K [42]. Slightly smaller coefficients have been determined by Kurashima et al. [100] with -0.1 MHz/K and -0.12 MHz/K for two different single-mode fibers and a signal wavelength of 1320 nm.

Investigations on the active SBS suppression in single-mode fibers by applying different temperature distributions along the fiber were carried out by Hansryd et al. [101]. With a stairway-shaped temperature distribution generated from eight differently heated fiber spools an 8 dB suppression of SBS was achieved with a Brillouin spectrum broadened from about 50 MHz to 200 MHz.

A similar approach was followed by Machewirth et al. [102] to actively suppress the SBS threshold in an all-fiber high-power amplifier system. By heating half of a 6.5 m long ytterbium doped fiber up to 80°C and leaving the rest cooled around 20°C, an output power of 177 W was achieved in co-pumped configuration, whereas only 60 W were possible without heating the fiber.

## Investigations on SBS suppression by temperature variation

In order to investigate the suppression of SBS in high-power fiber amplifiers by applying temperature gradients the amplifier setup was modified by coiling a 2 m long section of the step-index fiber (PLMA-YDF-20/400) characterized in Chapter 6 on a metal spool that was placed on a hot plate (Fig. 7.4).

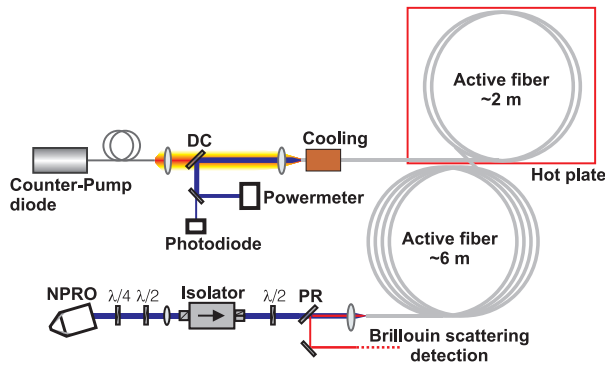


**Figure 7.4:** Experimental setup of step-index fiber amplifier with 2 m heated fiber. DC dichroic, PR partially reflective mirror.

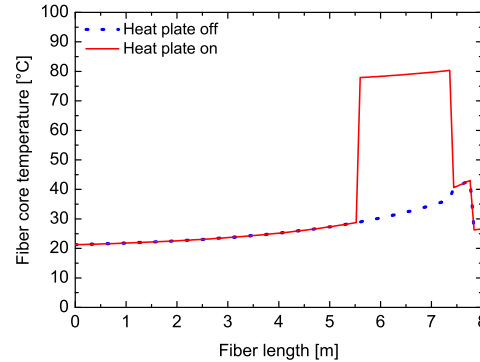


**Figure 7.5:** Simulation of temperature along step-index fiber core corresponding to experiment with hot plate off and at 85°C.

Only little deformations on the Brillouin spectra induced by absorbed pump light have been observed without actively heating the fiber and consequently the effect on the SBS threshold was relatively weak. Simulated temperature distributions along the active fiber for this experimental configuration with no heat applied and at a hot plate temperature of 85°C are plotted in (Fig. 7.5).

These investigations were carried out for the step-index fiber amplifier in counter-pumped configuration only. At a fixed amplifier output power of 70 W the hot plate temperature was slowly increased and the Brillouin scattering spectra were detected with the heterodyne system. At hot plate temperatures below 30°C only one peak was observed around 1.29 GHz. Towards higher temperatures a second peak evolved reaching a peak-to-peak separation of  $\approx 113$  MHz at a hot plate temperature of 85°C (Fig. 7.6).

Numerical simulations of the Brillouin scattering spectra for the step-index fiber amplifier operated at 70 W of output power and a heated fiber section showed good agreement with the experimentally detected spectra (Fig. 7.6). However, the length of the heated fiber section needed to be adjusted to 1.9 m in order to match the ratio between the measured Brillouin peak intensities. The theoretical external temperature increase in this section

needed to be set to  $69^\circ\text{C}$  to obtain an equivalent peak-to-peak separation of 113 MHz. This difference between the experimental hot plate temperature of  $85^\circ\text{C}$  and a theoretical value of  $69^\circ\text{C}$  was attributed to the thermal contact and resistance between the heated metal spool and the amplifier fiber. Both experimentally determined Brillouin peaks showed a slightly different spectrum towards higher frequencies. This characteristic originated from fiber sections between the cooled copper holder at the pump input end of the fiber and the heated spool and between both fiber spools (see Fig. 7.4 and 7.5). In these regions the active fiber was only cooled by convection to air, resulting in larger fiber core temperatures.

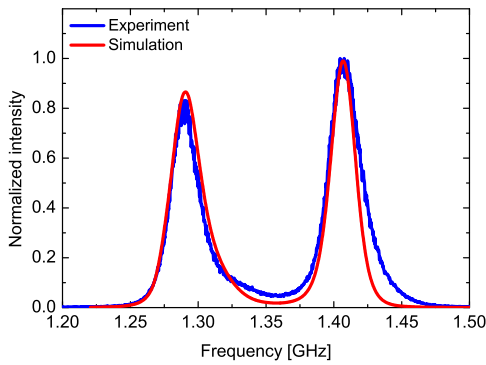


**Figure 7.6:** Experimental and calculated Brillouin spectra from step-index fiber amplifier at 70 W and hot plate at  $85^\circ\text{C}$ .

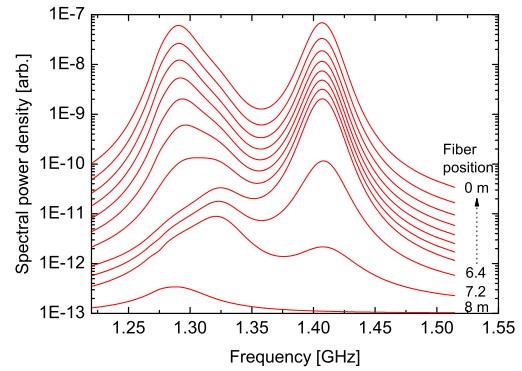


**Figure 7.7:** Simulated evolution of Brillouin spectrum over step-index fiber length at 70 W and hot plate at  $85^\circ\text{C}$ .

The simulated evolution of the Brillouin spectra over the fiber length shown in Fig. 7.7 illustrates the origin and peak intensities of the two main peaks. In the cooled fiber region close to  $z = 8$  m the Brillouin spectrum evolves around 1.29 GHz. In the heated fiber section ( $z = 5.6$ -7.5 m) the peak around 1.42 GHz starts to rise rapidly until at fiber positions where no heat is applied ( $z < 5.6$  m), these frequency components are only further enhanced by residual fiber amplifier laser gain. In this range the 1.29 GHz peak again experiences strong Brillouin gain. The integral of the Brillouin scattering output spectrum at  $z = 0$  m resulted in a Brillouin power of  $0.51 \mu\text{W}$ . For comparison, with no external heat source a Brillouin power of  $70 \mu\text{W}$  was simulated at the same amplifier output power of 70 W.

The temperature dependent Brillouin frequency shift  $c_f$  was determined to be  $2.25 \text{ MHz/K}$  by fitting the spectral peak separation with respect to the measured fiber spool temper-

ature (Fig. 7.8). This value has been incorporated in the numerical model for simulations of Brillouin scattering spectra.

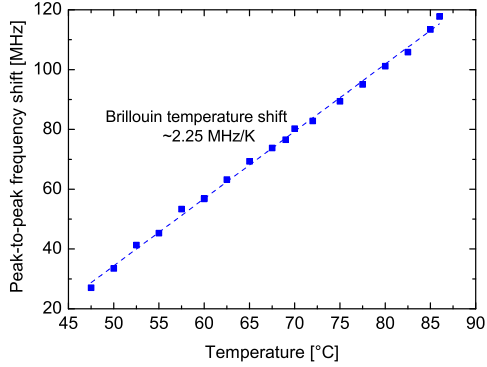


**Figure 7.8:** Separation of two Brillouin scattering peaks from step-index fiber amplifier with respect to hot plate temperature.

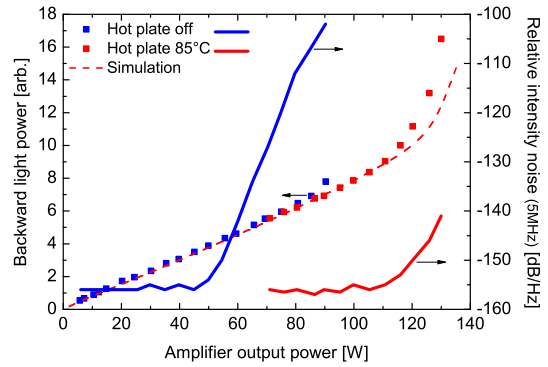


**Figure 7.9:** Backward power and relative intensity noise SBS thresholds of step-index fiber amplifier with hot plate off and at 85°C.

At a hot plate temperature of 85°C the amplifier pump power was increased to investigate the resulting suppression of SBS (Fig. 7.9). The backward propagating light power increased linearly up to an amplifier output power of 115 W and then started to increase exponentially indicating again the onset of SBS. Compared to the previously observed SBS threshold around 85 W with no external fiber temperature gradients applied, the output power could be increased by approximately 1.3 dB. Simulations of the backward power calculated from the sum of ASE and Brillouin scattered light power showed a SBS threshold at a slightly larger amplifier output power of 120 W. Although, the simulated Brillouin scattering spectra were in good agreement with the heterodyne spectra, the complex fiber temperature profile did not allow for an exact theoretical representation of the fiber amplifier arrangement.

Interestingly, the RIN of the amplifier output detected at 5 MHz showed an exponential increase in the same power range around 115 W. With no temperature applied this increase has been detected already at 50 W of amplifier output power, corresponding to a SBS noise threshold suppression of 3.5 dB.

Pump-and-probe measurements of the step-index fiber with heat applied over the whole fiber length have been carried out to verify the Brillouin frequency temperature shift  $c_f$  and determine a value for the Brillouin linewidth change  $c_b$ . With a heterodyne detection during amplifier operation the Brillouin linewidth is increased while heating the fiber due

to a decreased overall Brillouin gain and no information on the temperature dependent linewidth change is gained. However, heating the step-index fiber resulted in distorted spectra measured with the pump-and-probe detection scheme with again a second peak arising from the main Brillouin peak. In the experimental setup approximately 7 m of the fiber were heated and about half a meter stayed unheated to accomplish coupling of the pump and probe beams on either side of the fiber. These unheated fiber ends lead to the undesirable spectral distortions and made a determination of  $c_b$  impossible. Additionally, re-absorption losses at high fiber temperatures significantly decrease the pump-and-probe system sensitivity.

The presented experiments show that external temperature gradients can be applied to effectively suppress SBS. However, in high-power fiber amplifiers with counter-propagating pump and signal light the resulting intrinsic exponential temperature distribution induced by absorbed pump light along the fiber already represents an almost ideal temperature profile to minimize SBS influences.

### 7.3 Glass composition and fiber design

The choice of glass composition, doping and host materials strongly effects Brillouin scattering in optical fibers. Different doping levels of  $\text{GeO}_2$  and F, that are used to adjust the refractive index of the fiber core, were found to change the Brillouin frequency shift in single-mode fibers operated at 1550 nm by -45 MHz/wt.% and -277 MHz/wt.% by Shiraki et al. [103]. Taking advantage of this characteristic a single-mode fiber with non-uniform longitudinal doping distribution was developed resulting in a suppression of SBS by 7 dB. The linewidth of the Brillouin gain spectrum changes with respect to the  $\text{GeO}_2$  by 1.4 MHz/wt.% [42].

Alternatively the shape of the doped fiber core can be designed to minimize the overlap integral of acoustic and optical modes. Typically, the overlap integral of the lowest order modes is close to one in a step-index fiber core. Design concepts for a  $\text{GeO}_2$  fiber core with minimized overlap integral were published by Kobayakov et al. [104] for single-mode fibers. By changing the  $\text{GeO}_2$  doping distribution from a standard step-index to a W-shaped profile, the SBS threshold can be increased by more than 3 dB. For large mode-area (LMA) fibers these concepts are not applicable, due to the low refractive index steps

between core and cladding. By mixing different doping materials, such as  $\text{Al}_2\text{O}_3$  and  $\text{GeO}_2$ , Li et al. [105] managed to change the modal profile of acoustic and optical modes, while maintaining a step-index optical refractive index delta function. This approach can lead to doping distributions that guide the fundamental optical mode but anti-guide any acoustic modes, owing to different material acoustic and optical refractive indices [106].

With an ytterbium doped fiber having a  $30\ \mu\text{m}$  core diameter co-doped with a specific  $\text{Al}_2\text{O}_3/\text{GeO}_2$  distribution, up to 6 dB suppression of SBS was achieved. In a comparative experiment with two 12 m long fibers with the same geometrical parameters, the SBS threshold was observed at 40 W for a standard step-index core and between 150-200 W for the Al/Ge co-doped fiber. With a fiber of the same kind but a larger core diameter of  $39\ \mu\text{m}$ , an amplifier output power of 502 W, non-polarized and with a beam propagation factor  $M^2$  of 1.4 was demonstrated without an onset of SBS [29].

Recently a similar fiber with an acoustically designed step-index core has been demonstrated by Mermelstein et al. [107, 108] with up to 11.2 dB SBS suppression integrated in an all-fiber co-pumped amplifier setup with 194 W of output power with nearly diffraction limited beam quality. The Brillouin peak gain value  $g_{B_0}$  was estimated to be  $1.2 \cdot 10^{-12}$  m/W. With such a low Brillouin gain value fiber amplifier arrangements with output powers in excess of 1 kW may be feasible.

## 7.4 Large-core fibers

Standard LMA step-index fibers with core diameters in the range of  $20\text{-}30\ \mu\text{m}$  with small numerical apertures can be effectively operated with a nearly diffraction limited output by bending the fiber and inducing strong propagation losses for higher-order modes [25]. Larger core diameters would obviously be beneficial in order to reduce optical nonlinearities such as SBS. However, for a maintained good beam quality the bend loss technique becomes less effective and results in modal distortions for larger core diameters and different fiber designs and operational concepts need to be considered [109]. In recent years several approaches have been proposed and implemented.

Gain-guided, index-antiguidded fibers were proposed by Siegman [110] and recently demonstrated with single-mode operation in a  $200\ \mu\text{m}$  core diameter by Sudesh et al. [111]. These fibers exhibit a negative refractive index step and light guidance is achieved



only by strong laser gain in the core region. This novel concept could up to now only be demonstrated in relatively short fibers with a few tens of mm length and an output power of less than 10 W. A challenging task is the coupling of pump radiation in double-clad fiber designs from an outer cladding to the center core region due to the particular refractive index step.

A different approach are chirally-coupled core (CCC) fibers [112]. Helical satellite cores wrapped around the main center core convert higher-order modes from core into helical core modes that can be designed to experience high propagation losses. With a core diameter of  $33\ \mu\text{m}$  the first active ytterbium doped CCC fiber was demonstrated emitting 40 W of output power [113].

The effective mode area can also be increased with an operation of the optical fiber in higher-order modes (HOM). Passive fibers that robustly deliver an  $\text{LP}_{08}$  mode were developed by Mermelstein et al. [114] with a mode area of  $1714\ \mu\text{m}^2$ . In these devices long period fiber gratings couple from single-mode  $\text{LP}_{01}$  to the  $\text{LP}_{08}$  mode and vice versa with a coupling efficiency of 99%. The enlarged mode profile enabled a suppression of SBS by more than 13 dB compared to the fundamental mode operation.

A different design approach are leakage channel fibers, where a number of large holes define a waveguide for the fundamental mode in the optical fiber. Channels between the holes can be engineered to introduce significant higher order mode loss. Laser operation from ytterbium doped leakage channel fibers with effective mode areas of up to  $3160\ \mu\text{m}^2$  was demonstrated by Dong et al. [115] with an output power of 4.5 W and a beam propagation factor  $M^2$  of 1.3.

Photonic crystal fibers (PCF) have gained much attention in recent years owing to remarkable optical properties such as endlessly single-mode light guidance [116] and the ability to be operated with a single transverse-mode in extremely large core fibers with low numerical apertures. Continuous-wave (CW) laser operation with up to 320 W of output power and single-mode output was demonstrated using a PCF with a core diameter of  $60\ \mu\text{m}$  by Limpert et al. [117]. This PCF design with fiber core diameters larger than  $40\ \mu\text{m}$  does not allow for a coiling of the fiber anymore due to strong bend losses also induced for the fundamental mode. The fiber micro-structure is therefore surrounded by a silica cladding with a diameter of 1.5 mm for a mechanical stabilization. These fibers are hence called rod-type fibers with a typical length of only 0.5-1 m. With such a short length rod-type fibers are in general less suitable for high average power applications.

### Simulations on SBS suppression with large-core PCF

Recently a polarization maintaining PCF (DC-400-38-PZ-Yb) capable of delivering high pump power has been introduced by Crystal Fibre [62] with core and cladding diameters of  $38\ \mu\text{m}$  and  $400\ \mu\text{m}$ , respectively (Fig. 7.10).

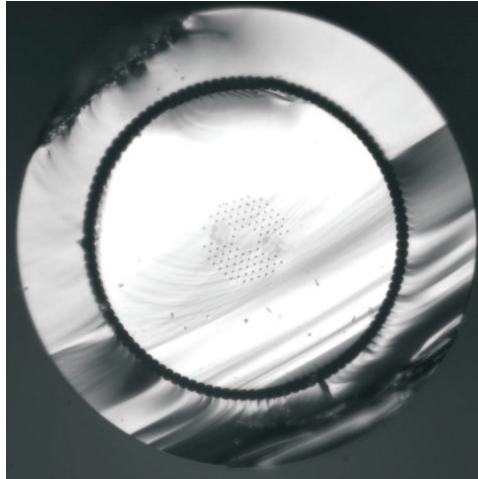


**Figure 7.10:** Microscope picture of the DC-400-38-PZ-Yb photonic crystal fiber [62].

The large cladding diameter with a high numerical aperture of 0.58 enables an efficient coupling of high-power, low brightness pump laser diodes and increases the absorption length to approximately 6 m. On the following pages some simulations on the power scaling of a fiber amplifier system comprising such a large-core PCF are presented.

Applying the numerical model for the simulation of a counter-pumped amplifier with such a PCF reveals that even at an output power of 1 kW the Brillouin scattering power would still be in the microwatt range owing to the large mode field diameter together with an advantageous temperature induced Brillouin spectral broadening (Figs. 7.11 and 7.12).

These simulations were carried out with a seed signal power of 10 W and a maximum launched pump power of 1300 W in counter-pumped configuration. Nowadays, the brightness of commercially available fiber coupled laser diodes allows for such a pump power coupled into the cladding of the PCF. At such pump power levels the fiber cooling would need to be improved compared to the previously presented experiments in order to keep the fiber core at moderate temperatures below  $200^\circ\text{C}$ . With a heat transfer coefficient at the fiber surface of  $h = 500\ \text{W}/\text{m}^2\text{K}$  over the entire fiber length the calculated maximum core temperature stays below  $170^\circ\text{C}$ . Heat transfer coefficients in the range of  $500\ \text{W}/\text{m}^2\text{K}$  are for instance obtained in water-cooled systems with low flow rates. Although air-cladding

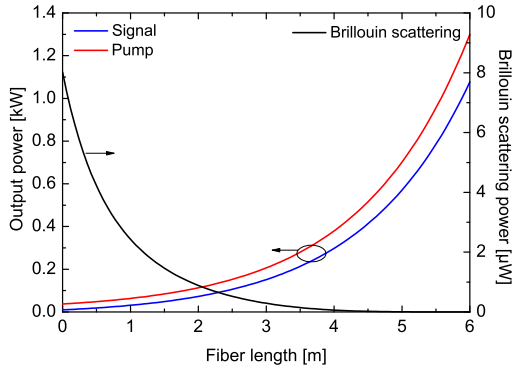


**Figure 7.11:** Simulation of signal, pump and Brillouin scattering power with respect to the DC-400-38-PZ-Yb fiber length.

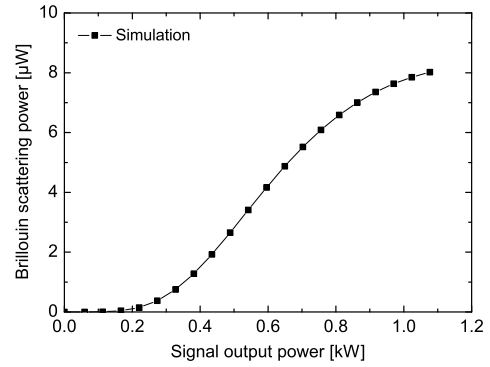


**Figure 7.12:** Simulation of Brillouin scattering power at different amplifier output power of a DC-400-38-PZ-Yb fiber.

fibers can in general handle higher temperature levels compared to polymer coated fibers, experimental work would still need to show proof for a long term stable operation of such an amplifier system.

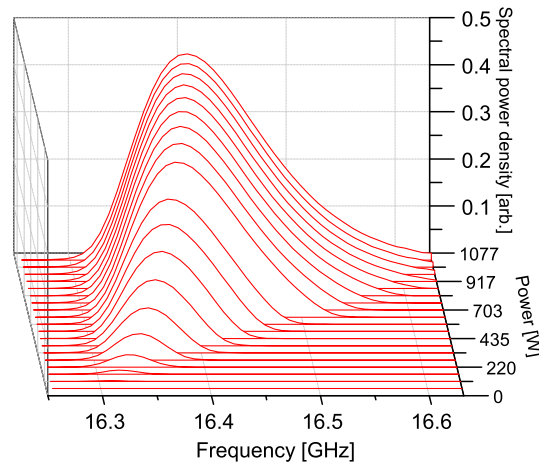


**Figure 7.13:** Simulation of the Brillouin scattering spectral evolution of an amplifier with DC-400-38-PZ-Yb fiber.

A spontaneous Brillouin gain spectrum with a Lorentzian shaped profile, a spectral width (FWHM) of  $\Delta\nu_B = 60$  MHz and a peak gain value of  $g_{B_0} = 2.5 \cdot 10^{-11}$  m/W was assumed. The Brillouin spectral evolution with respect to the fiber amplifier output power is plotted in Figs. 7.13. At maximum output power of 1077 W the simulated spectral width is increased to more than 130 MHz through temperature induced Brillouin frequency shifts and SBS is effectively suppressed.



## 8. Summary

A growing demand for narrow-linewidth laser sources with high output power and excellent beam quality has led to intensified research activities in the field of high-power fiber amplifier systems. In narrow-linewidth fiber optical systems, stimulated Brillouin scattering (SBS) limits the power handling capacity and scaling to higher output power. Although great progress has been made to suppress SBS and more than 400 W of output power with nearly diffraction limited beam quality and a linear polarization have been demonstrated, SBS still represents the most stringent limitation for these laser systems.

The subject of this thesis was the experimental and theoretical investigation of Brillouin scattering and its influences on the high-power fiber amplifier operation. Comprehensive studies on the Brillouin scattering power and spectral evolution in fiber amplifier systems were carried out. A numerical model based on coupled rate-equations was used to theoretically describe and analyze the obtained results.

The experimental basis for these investigations was a single-stage high-power master-oscillator fiber amplifier system operated with a step-index and alternatively a photonic crystal fiber (PCF) both doped with ytterbium ions. A non-planar ring-oscillator with 2 W of output power and an emission linewidth of 1 kHz served as the seed source. Whereas the maximum output power of the step-index fiber amplifier was limited by the onset of SBS to approximately 90 W, the PCF could be operated with an output power of up to 148 W only limited by the available pump power. This result represents a record power level for a narrow-linewidth PCF amplifier. Both amplifier systems showed a very efficient operation with a slope efficiency of more than 76% and excellent beam parameters with nearly diffraction limited beam qualities, an ASE suppression of more than 39 dB and linear polarization with polarization extinction ratios of better than 18 dB.

In high-power fiber amplifier systems the fiber design and length, the amplifier pump configuration and temperature gradients along the fiber greatly influence the threshold characteristics of SBS. With a high-resolution experimental detection of the Brillouin scattering spectral evolution these influences have been comprehensively analyzed for the first time. The SBS threshold was characterized by monitoring the nonlinear increase of backwards propagating light power from the active fiber and the relative intensity noise (RIN) of the output beams. Besides a reduction of fiber length and increase of fiber core size using large mode-area (LMA) fibers, the signal intensity, gain and temperature distributions in amplifiers with counter-propagating signal and pump light effectively mitigate SBS compared to co-pumped configurations. With the numerical model these influences were theoretically simulated with excellent agreement to the experimentally observed characteristics, which allows for a deeper understanding and a good estimate of SBS thresholds for different amplifier systems. The presented investigations demonstrate the potential of ytterbium doped LMA fibers for power scaling of narrow-linewidth laser sources. Fiber amplifier and thermal designs with an efficient SBS suppression can be developed.

Different approaches for a further suppression of SBS have been presented and in some parts studied with the developed experimental and theoretical methods. The most prominent suppression techniques are based on the idea of shifting the Brillouin frequency along the fiber to lower the effective Brillouin gain for each frequency component. Either temperature and strain gradients or varying doping distributions along the fiber can be applied to influence the acoustic velocity of phonons, which contribute to the Brillouin scattering process. Although a change of glass composition and co-doping levels or simply the use of different types of fibers spliced together has been successfully applied in the past to mitigate SBS in passive single-mode fibers, this approach is almost not applicable for active LMA fibers mostly owing to small tolerances in the co-doping levels and concerns about the reliability of such fibers in high-power operation. However, applying temperature and strain gradients by heating and stretching parts of active LMA fibers has been investigated in this work with some success showing a suppression of the SBS threshold of up to 2 dB. In counter-pumped fiber amplifiers temperature gradients induced by absorbed pump light passively increase the SBS threshold by several dB. Although these suppression techniques are limited at some point by the degradation and damage of fibers at certain elongation and temperature levels, amplifier output powers of several hundred Watts can be achieved even with standard LMA fibers.

Most promising and reliable concepts to overcome SBS constraints in high-power amplifiers are novel LMA fiber designs with increased mode-field diameters that can still be operated in fundamental mode. Additionally, doping compositions have been presented that minimize the transversal overlap of the optical and acoustic modes in the fiber core region and lower the Brillouin gain by orders of magnitude. In recent years there has been a rapid improvement in the field of narrow-linewidth fiber amplifier systems for high-power laser applications. With an efficient suppression of SBS by applying special fiber and amplifier design concepts it nowadays looks very promising that the scaling of output power to more than 1 kW can be achieved with excellent beam characteristics.





# Bibliography

- [1] E. Desurvire, *Erbium-Doped Fiber Amplifiers: Principles and Applications* (Wiley-Interscience, 2002).
- [2] T. R. Parker, M. Farhadiroushan, V. A. Handerek, and A. J. Roger, “A fully distributed simultaneous strain and temperature sensor using spontaneous Brillouin backscatter,” *IEEE Photon. Technol. Lett.* **9**, 979–981 (1997).
- [3] D. Culverhouse, F. Farahi, C. N. Pannell, and D. A. Jackson, “Potential of stimulated Brillouin scattering as sensing mechanism for distributed temperature sensor,” *Electron. Lett.* **25**, 913–914 (1989).
- [4] W. D. Phillips, “Laser cooling and trapping of neutral atoms,” *Rev. Mod. Phys.* **70**, 721–741 (1998).
- [5] K. Kobayashi and I. Mito, “Single frequency and tunable laser diodes,” *J. Lightwave Techn.* **6**, 1623–1633 (1988).
- [6] C. Spiegelberg, J. Geng, Y. Hu, Y. Kaneda, S. Jiang, and N. Payghambarian, “Low-noise narrow-linewidth fiber laser at 1550 nm,” *J. Lightwave Techn.* **22**, 57–62 (2004).
- [7] J. J. Zayhowski and A. Mooradian, “Single-frequency microchip Nd lasers,” *Opt. Lett.* **14**, 24–26 (1989).
- [8] T. J. Kane and R. L. Byer, “Monolithic, unidirectional single-mode Nd:YAG ring laser,” *Opt. Lett.* **10**, 65–67 (1985).
- [9] H. Stoehr, F. Mensing, J. Helmcke, and U. Sterr, “Diode laser with 1 Hz linewidth,” *Opt. Lett.* **31**, 736–738 (2006).

- 
- [10] J. Geng, C. Spiegelberg, and S. Jiang, "Narrow linewidth fiber laser for 100-km optical frequency domain reflectometry," *IEEE Photon. Technol. Lett.* **17**, 1827–1829 (2005).
- [11] S. A. Webster, M. Oxborrow, and P. Gill, "Subhertz-linewidth Nd:YAG laser," *Opt. Lett.* **29**, 1497–1499 (2004).
- [12] A. Weinstein, "Advanced LIGO optical configuration and prototyping effort," *Class. Quantum Grav.* **19**, 1575–1584 (2002).
- [13] J. C. Bienfang, C. A. Denman, B. W. Grime, P. D. Hillman, G. T. Moore, and J. M. Telle, "20 W of continuous-wave sodium D<sub>2</sub> resonance radiation from sum-frequency generation with injection-locked lasers," *Opt. Lett.* **28**, 2219–2221 (2003).
- [14] I. Freitag, A. Tünnermann, and H. Welling, "Power scaling of diode-pumped monolithic Nd:YAG lasers to output powers of several watts," *Opt. Commun.* **115**, 511–515 (1994).
- [15] M. Frede, R. Wilhelm, D. Kracht, C. Fallnich, F. Seifert, and B. Willke, "195 W injection-locked single-frequency laser system," *Proc. CLEO* (2005).
- [16] Y. Jeong, J. Nilsson, J. K. Sahu, D. N. Payne, L. M. B. Hickey, and P. W. Turner, "Power scaling of single-frequency ytterbium-doped fiber master-oscillator power-amplifier sources up to 500 W," *IEEE J. Quantum Elect.* **13**, 546–551 (2007).
- [17] S. J. Augst, F. T. Y, and A. Sanchez, "Coherent beam combining and phase noise measurements of ytterbium fiber amplifiers," *Opt. Lett.* **29**, 474–476 (2004).
- [18] H. M. Pask, R. J. Carman, D. C. Hanna, A. C. Tropper, C. J. Mackechnie, P. R. Barber, and J. M. Dawes, "Ytterbium-doped silica fiber lasers: Versatile sources for the 1-1.2  $\mu\text{m}$  region," *IEEE J. Quantum Elect.* **1**, 2–13 (1995).
- [19] IPG Photonics Corp., "IPG Photonics introduces the world's first commercial three kilowatt single mode fiber laser," *Tech. rep.* (2007).
- [20] R. Paschotta, J. Nilsson, A. C. Tropper, and D. C. Hanna, "Ytterbium-doped fiber amplifiers," *IEEE J. Quantum Elect.* **33**, 1049–1056 (1997).

- [21] I. Zawischa, K. Plamann, C. Fallnich, H. Welling, H. Zellmer, and A. Tünnermann, “All-solid-state neodymium-based single-frequency master-oscillator fiber power-amplifier system emitting 5.5 W of radiation at 1064 nm,” *Opt. Lett.* **24**, 469–471 (1999).
- [22] R. G. Smith, “Optical power handling capacity of low loss optical fibres as determined by stimulated Raman and Brillouin scattering,” *Appl. Opt.* **11**, 2489–2494 (1972).
- [23] S. Höfer, A. Liem, J. Limpert, H. Zellmer, A. Tünnermann, S. Unger, S. Jetschke, and H.-R. Müller, “Single-frequency master-oscillator fiber power amplifier system emitting 20 W of power,” *Opt. Lett.* **26**, 1326–1328 (2001).
- [24] A. Liem, J. Limpert, H. Zellmer, and A. Tünnermann, “100-W single-frequency master-oscillator fiber power amplifier,” *Opt. Lett.* **28**, 1537–1539 (2003).
- [25] J. P. Koplow, L. Goldberg, R. P. Moeller, and D. A. V. Kliner, “Single-mode operation of a coiled multimode fiber,” *Opt. Lett.* **25**, 442–444 (2000).
- [26] R. Paschotta, J. Nilsson, P. R. Barber, J. E. Caplen, A. C. Tropper, and D. C. Hanna, “Lifetime quenching in Yb-doped fibres,” *Opt. Commun.* **136**, 375–378 (1997).
- [27] J. J. Koponen, M. J. Söderlund, H. J. Hoffman, and S. K. T. Tammela, “Measuring photodarkening from single-mode ytterbium doped silica fibers,” *Opt. Express* **14**, 11539–11544 (2006).
- [28] Y. Jeong, J. Nilsson, J. K. Sahu, D. B. S. Soh, C. Alegria, P. Dupriez, C. A. Codemard, D. N. Payne, R. Horley, L. M. B. Hickey, L. Wanzcyk, C. E. Chryssou, J. A. Alvarez-Chavez, and P. W. Turner, “Single-frequency, single-mode, plane-polarized ytterbium-doped fiber master oscillator power amplifier source with 264 W of output power,” *Opt. Lett.* **30**, 459–461 (2005).
- [29] S. Gray, A. Liu, D. T. Walton, J. Wang, M.-J. Li, X. Chen, A. B. Ruffin, J. A. DeMeritt, and L. A. Zenteno, “502 Watt, single transverse mode, narrow linewidth, bidirectionally pumped Yb-doped fiber amplifier,” *Opt. Express* **15**, 17044–17050 (2007).
- [30] G. E. Durand and A. S. Pine, “High-resolution low-level Brillouin spectroscopy in solids,” *IEEE J. Quantum Elect.* **QE-4**, 523–528 (1968).

- 
- [31] E. P. Ippen and R. H. Stolen, “Stimulated Brillouin scattering in optical fibers,” *Appl. Phys. Lett.* **21**, 539–540 (1972).
- [32] N. Shibata, R. G. Waarts, and R. P. Braun, “Brillouin-gain spectra for single-mode fibers having pure-silica, GeO<sub>2</sub>-doped, and P<sub>2</sub>O<sub>5</sub>-doped cores,” *Opt. Lett.* **12**, 269–271 (1987).
- [33] R. W. Tkach, A. R. Chraplyvy, and R. M. Derosier, “Spontaneous Brillouin scattering for single-mode optical-fibre characterisation,” *Electron. Lett.* **22**, 1011–1013 (1986).
- [34] R. W. Boyd, *Nonlinear Optics* (Academic Press, 2003).
- [35] R. H. Stolen, E. P. Ippen, and A. R. Tynes, “Raman oscillation in glass optical waveguides,” *Appl. Phys. Lett.* **20**, 62–64 (1972).
- [36] G. P. Agrawal, *Nonlinear Fiber Optics* (Academic Press, 2007).
- [37] L. Brillouin, “Diffusion de la lumière et des rayons x par un corps transparent homogène - influence de l’agitation thermique,” *Ann. Phys. (Paris)* **17**, 88–122 (1922).
- [38] L. I. Mandelstam, “Light scattering by inhomogeneous media,” *Zh. Russ. Fiz-Khim.* **58**, 381 (1926).
- [39] R. S. Krishnan, “Fine structure of the Rayleigh line in amorphous substances,” *Nature* **165**, 933–934 (1950).
- [40] R. Y. Chiao, C. H. Townes, and B. P. Stoicheff, “Stimulated Brillouin scattering and coherent generation of intense hypersonic waves,” *Phys. Rev. Lett.* **12**, 592–595 (1964).
- [41] M. O. van Deventer and A. J. Boot, “Polarization properties of stimulated Brillouin scattering in single-mode fibers,” *J. Lightwave Techn.* **12**, 585–590 (1994).
- [42] M. Niklès, L. Thévenaz, and P. Robert, “Brillouin gain spectrum characterization in single-mode optical fibers,” *J. Lightwave Techn.* **15**, 1842–1851 (1997).
- [43] E. Lichtman and A. A. Friesem, “Stimulated Brillouin scattering excited by a multimode laser in single-mode optical fibers,” *Opt. Commun.* **64**, 544–548 (1987).

- 
- [44] D. Cotter, “Stimulated Brillouin scattering in monomode optical fiber,” *J. Opt. Commun.* **4**, 10–19 (1983).
- [45] C. R. Giles and E. Desurvire, “Modeling erbium-doped fiber amplifiers,” *J. Light-wave Techn.* **9**, 271–283 (1991).
- [46] A. Hardy and R. Oron, “Signal amplification in strongly pumped fiber amplifiers,” *IEEE J. Quantum Elect.* **33**, 307–313 (1997).
- [47] C. N. Pannell, P. S. J. Russell, and T. P. Newson, “Stimulated Brillouin scattering in optical fibers: the effect of optical amplification,” *J. Opt. Soc. Am. B* **10**, 684–690 (1993).
- [48] N. A. Brilliant, “Stimulated Brillouin scattering in a dual-clad fiber amplifier,” *J. Opt. Soc. Am. B* **19**, 2551–2557 (2002).
- [49] V. I. Kovalev and R. G. Harrison, “Suppression of stimulated Brillouin scattering in high-power single-frequency fiber amplifiers,” *Opt. Lett.* **31**, 161–163 (2006).
- [50] A. Liu, “Suppressing stimulated Brillouin scattering in fiber amplifiers using nonuniform fiber and temperature gradient,” *Opt. Express* **15**, 977–984 (2007).
- [51] M. Muendel, “Optimal inner cladding shapes for double-clad fiber lasers,” *Proc. CLEO CTuU2* (1996).
- [52] D. Marcuse, “Loss analysis of single-mode fiber splices,” *Bell Syst. Tech. J.* **56**, 703–718 (1977).
- [53] Nufern Inc., <http://www.nufern.com/>.
- [54] D. E. McCumber, “Einstein relations connecting broadband emission and absorption spectra,” *Phys. Rev.* **136**, 954–957 (1964).
- [55] D. C. Brown and H. J. Hoffman, “Thermal, stress, and thermo-optic effects in high average power double-clad silica fiber lasers,” *IEEE J. Quantum Elect.* **37**, 207–216 (2001).
- [56] Y. Wang, C.-Q. Xu, and H. Po, “Thermal effects in kilowatt fiber lasers,” *IEEE Photon. Technol. Lett.* **16**, 63–65 (2004).

- 
- [57] J. Limpert, T. Schreiber, A. Liem, S. Nolte, and H. Zellmer, “Thermo-optical properties of air-clad photonic crystal fiber lasers in high power operation,” *Opt. Express* **11**, 2982–2990 (2003).
- [58] B. Y. Zel’dovich, N. F. Pilipetsky, and V. V. Shkunov, *Principles of Phase Conjugation* (Springer-Verlag, 1985).
- [59] R. W. Boyd, K. Rzazewski, and P. Narum, “Noise initiation of stimulated Brillouin scattering,” *Physical Review A* **42**, 5514–5521 (1990).
- [60] S. Le Floch and P. Cambon, “Study of Brillouin gain spectrum in standard single-mode optical fiber at low temperatures (1.4–370 K) and high hydrostatic pressures (1–250 bars),” *Opt. Commun.* **219**, 395–410 (2003).
- [61] Innolight GmbH, <http://www.innolight.de/>.
- [62] Crystal Fibre A/S, <http://www.crystal-fibre.com/>.
- [63] Laserline GmbH, <http://www.laserline.de/>.
- [64] LightPath Technologies Inc., <http://www.lightpath.com/>.
- [65] Zemax Development Corp., <http://www.zemax.com/>.
- [66] A. Bjarklev, J. Broeng, S. E. Barkou, T. S. Knudsen, T. S. Sonergaard, T. W. Berg, and M. G. Dyndgaard, “Polarization properties of honeycomb-structured photonic bandgap fibres,” *J. Opt. A: Pure Appl. Opt.* **2**, 584–588 (2000).
- [67] M. D. Nielsen, N. A. Mortensen, M. Albertsen, J. R. Folkenberg, A. Bjarklev, and D. Bonacinni, “Predicting macrobending loss for large-mode area photonic crystal fibers,” *Opt. Express* **12**, 1775–1779 (2004).
- [68] A. E. Siegman, M. W. Sasnett, and T. F. Johnston, “Choice of clip levels for beam width measurements using knife-edge techniques,” *IEEE J. Quantum Elect.* **27**, 1098–1104 (1991).
- [69] J. Limpert, T. Schreiber, S. Nolte, H. Zellmer, and A. Tünnermann, “High-power air-clad large-mode-area photonic crystal fiber laser,” *Opt. Express* **11**, 818–823 (2003).

- [70] A. Mafi and J. V. Moloney, “Beam quality of photonic-crystal fibers,” *J. Lightwave Techn.* **23**, 2267–2270 (2005).
- [71] A. E. Siegman, “New developments in laser resonators,” *Proc. SPIE* **1224**, 2–14 (1990).
- [72] B. Willke, N. Uehara, E. K. Gustafson, R. L. Byer, P. J. King, S. U. Seel, and R. L. Savage, “Spatial and temporal filtering of a 10-W Nd:YAG laser with a Fabry-perot ring-cavity premode cleaner,” *Opt. Lett.* **23**, 1704–1706 (1998).
- [73] P. Kwee, F. Seifert, B. Willke, and K. Danzmann, “Laser beam quality and pointing measurement with an optical resonator,” *Rev. Sci. Instrum.* **78**, 073103–1–10 (2007).
- [74] P. Weßels and C. Fallnich, “Highly sensitive beam quality measurements on large-mode-area fiber amplifiers,” *Opt. Express* **11**, 3346–3351 (2003).
- [75] S. Hädrich, T. Schreiber, T. Pertsch, J. Limpert, T. Peschel, R. Eberhardt, and A. Tünnermann, “Thermo-optical behaviour of rare-earth-doped low-NA fibers in high power operation,” *Opt. Express* **14**, 6091–6097 (2006).
- [76] D. Heiman, D. S. Hamilton, and R. W. Hellwarth, “Brillouin scattering measurements on optical glasses,” *Phys. Rev. B* **19**, 6583–6592 (1979).
- [77] L. Zou, X. Bao, and L. Chen, “Brillouin scattering spectrum in photonic crystal fiber with a partially germanium-doped core,” *Opt. Lett.* **28**, 2022–2024 (2003).
- [78] T. C. E. Jones, “The validity of the single mode optical fibre transfer standard for the calibration of fibres for high power users,” *NPL Report COEM* **10** (1998).
- [79] P. Bayvel and P. M. Radmore, “Solutions of the SBS equations in single mode optical fibres and implications for fibre transmission systems,” *Electron. Lett.* **26**, 434–436 (1990).
- [80] X. P. Mao, R. W. Tkach, A. R. Chraplyvy, R. M. Jopson, and R. M. Derosier, “Stimulated Brillouin threshold dependence on fiber type and uniformity,” *IEEE Photon. Technol. Lett.* **4**, 66–69 (1992).
- [81] R. Oron and A. Hardy, “Rayleigh backscattering and amplified spontaneous emission in high-power ytterbium-doped fiber amplifiers,” *J. Opt. Soc. Am. B* **16**, 695–701 (1999).

- 
- [82] A. L. Gaeta and R. W. Boyd, "Stochastic dynamics of stimulated Brillouin scattering in an optical fiber," *Phys. Rev. A* **44**, 3205–3209 (1991).
- [83] J. Zhang and M. R. Phillips, "Cancellation of intensity noise caused by stimulated Brillouin scattering in an optical fiber transmission system," *Proc. CLEO PDP24* (2005).
- [84] A. Loayssa, D. Benito, and M. J. Garde, "High-resolution measurements of stimulated Brillouin scattering spectra in single-mode fibres," *IEE Proc.-Optoelectronics* **148**, 143–148 (2001).
- [85] A. Peral and A. Yariv, "Degradation of modulation and noise characteristics of semiconductor lasers after propagation in optical fiber due to a phase shift induced by stimulated Brillouin scattering," *IEEE J. Quantum Elect.* **35**, 1185–1195 (1999).
- [86] J. Zhang and M. R. Phillips, "Modeling intensity noise caused by stimulated Brillouin scattering in optical fibers," *Proc. CLEO CMH6* (2005).
- [87] M. Horowitz, A. R. Chraplyvy, R. W. Tkach, and J. L. Zyskind, "Broad-band transmitted intensity noise induced by stokes and anti-stokes brillouin scattering in single-mode fibers," *IEEE Photon. Technol. Lett.* **9**, 124–126 (1997).
- [88] M. Tröbs, P. Weßels, and C. Fallnich, "Power- and frequency-noise characteristics of an Yb-doped fiber amplifier and actuators for stabiliziation," *Opt. Express* **13**, 2224–2235 (2005).
- [89] A. Yeniay, J.-M. Delavaux, and J. Toulouse, "Spontaneous and stimulated Brillouin scattering gain spectra in optical fibers," *J. Lightwave Techn.* **20**, 1425–1432 (2002).
- [90] New Focus Inc., <http://www.newfocus.com/>.
- [91] Agilent Technologies Inc., <http://www.agilent.com/>.
- [92] Electro-Optics Technology Inc., <http://www.eotech.com/>.
- [93] J. J. Olivero and R. L. Longbothum, "Empirical fits to the Voigt line width: A brief review," *J. Quant. Spectrosc. Radiat. Transfer* **17**, 233 (1977).
- [94] A. S. Pine, "Brillouin scattering study of acoustic attenuation in fused quartz," *Phys. Rev.* **185**, 1187–1193 (1969).



- [95] T. Horiguchi, T. Kurashima, and M. Tateda, "Tensile strain dependence of Brillouin frequency shift in silica optical fibers," *IEEE Photon. Technol. Lett.* **1**, 107–108 (1989).
- [96] N. Yoshizawa, T. Horihushi, and T. Kurashima, "Proposal for stimulated Brillouin scattering suppression by fiber cabling," *Electron. Lett.* **27**, 1100–1101 (1991).
- [97] N. Yoshizawa and I. Takeshi, "Stimulated Brillouin scattering suppression by means of applying strain distribution to fiber with cabling," *J. Lightwave Techn.* **11**, 1518–1522 (1993).
- [98] J. M. Chavez Boggio, J. D. Marconi, and H. L. Fragnito, "Experimental and numerical investigation of the SBS-threshold increase in an optical fiber by applying strain distributions," *J. Lightwave Techn.* **23**, 3808–3814 (2005).
- [99] J. E. Rothenberg, P. A. Thielen, M. Wickham, and C. P. Asman, "Suppression of stimulated Brillouin scattering in single-frequency multi-kilowatt fiber amplifiers," *Proc. SPIE* **6873**, 687300–1–7 (2008).
- [100] T. Kurashima, T. Horiguchi, and M. Tateda, "Thermal effects of Brillouin gain spectra in single-mode fibers," *IEEE Photon. Technol. Lett.* **2**, 718–720 (1990).
- [101] J. Hansryd, F. Dross, M. Westlund, P. A. Andrekson, and S. N. Knudsen, "Increase of the SBS threshold in a short highly nonlinear fiber by applying a temperature distribution," *J. Lightwave Techn.* **19**, 1691–1697 (2001).
- [102] D. P. Machewirth, Q. Wang, B. Samson, K. Tankala, M. O'Connor, and M. Alam, "Current developments in high-power monolithic polarization maintaining fiber amplifiers for coherent beam combining applications," *Proc. SPIE* **6453**, 64531F (2007).
- [103] K. Shiraki, M. Ohashi, and M. Tateda, "SBS threshold of a fiber with a Brillouin frequency shift distribution," *J. Lightwave Techn.* **14**, 50–57 (1996).
- [104] A. Kobayakov, S. Kumar, D. Q. Chowdhury, A. B. Ruffin, M. Sauer, and S. R. Bickham, "Design concept for optical fibers with enhanced SBS threshold," *Opt. Express* **13**, 5338–5346 (2005).

- [105] A.-J. Li, X. Chen, J. Wang, S. Gray, A. Liu, J. A. Demeritt, A. B. Ruffin, A. M. Crowley, D. T. Walton, and L. A. Zenteno, “Al/Ge-doped large mode area fiber with high SBS threshold,” *Opt. Express* **15**, 8290–8299 (2007).
- [106] P. D. Dragic, C. H. Liu, G. C. Papen, and A. Galvanauskas, “Optical fiber with an acoustic guiding layer for stimulated Brillouin scattering suppression,” *Proc. CLEO CThZ3* (2005).
- [107] M. D. Mermelstein, K. Brar, M. J. Andrejco, A. D. Yablon, M. Fishteyn, C. Headley, and D. J. DiGiovanni, “All-fiber 194 W single-frequency single-mode Yb-doped master-oscillator power-amplifier,” *Proc. SPIE* **6873**, 68730L–1–6 (2008).
- [108] M. D. Mermelstein, M. J. Andrejco, J. Fini, A. Yablon, C. Headley, and D. J. DiGiovanni, “11.2 SBS gain suppression in a large mode area Yb-doped optical fiber,” *Proc. SPIE* **6873**, 68730N–1–7 (2008).
- [109] J. M. Fini, “Bend-resistant design of conventional and microstructure fibers with very large mode area,” *Opt. Express* **14**, 69–81 (2006).
- [110] A. E. Siegman, “Propagating modes in gain-guided optical fibers,” *J. Opt. Soc. Am. A* **20**, 1617–1628 (2003).
- [111] V. Sudesh, T. McComb, Y. Chen, M. Bass, M. Richardson, J. Ballato, and A. E. Siegman, “Diode-pumped 200  $\mu\text{m}$  diameter core, gain-guided, index-antiguidded single-mode fiber laser,” *Appl. Phys. B* **90**, 369–372 (2008).
- [112] C.-H. Liu, G. Chang, N. Litchinitser, D. Guertin, N. Jacobsen, K. Tankala, and A. Galvanauskas, “Chirally coupled core fibers at 1550-nm and 1064-nm for effectively single-mode core size scaling,” *Proc. CLEO CTuBB3* (2007).
- [113] M. C. Swan, C.-H. Liu, D. Guertin, N. Jacobsen, K. Tankala, and A. Galvanauskas, “33  $\mu\text{m}$  core effectively single-mode chirally-coupled-core fiber laser at 1064-nm,” *Proc. OFC OWU2* (2008).
- [114] M. D. Mermelstein, J. M. Ramachandran, J. M. Fini, and S. Ghalmi, “SBS gain efficiency measurements and modeling in a 1714  $\mu\text{m}$  effective area LP<sub>08</sub> higher-order mode optical fiber,” *Opt. Express* **15**, 15952–15963 (2007).

- 
- [115] L. Dong, J. Li, and X. Peng, “Bend-resistant fundamental mode operation in ytterbium-doped leakage channel fibers with effective areas up to  $3160\mu\text{m}^2$ ,” *Opt. Express* **14**, 11512–11519 (2006).
- [116] T. A. Birks, J. C. Knight, and P. S. J. Russell, “Endlessly single-mode photonic crystal fiber,” *Opt. Lett.* **22**, 961–963 (1997).
- [117] J. Limpert, O. Schmidt, J. Rothhardt, F. Röser, T. Schreiber, A. Tünnermann, S. Ermeneux, P. Yvernault, and F. Salin, “Extended single-mode photonic crystal fiber lasers,” *Opt. Express* **14**, 2715–2720 (2006).



# List of publications

## Journal articles

1. M. J. Lederer, M. Hildebrandt, V. Z. Kolev, B. Luther-Davies, B. Taylor, J. Dawes, P. Dekker, J. Piper, H. H. Tan, C. Jagadish, "Passive mode locking of a self-frequency-doubling Yb:YAl<sub>3</sub>(BO<sub>3</sub>)<sub>4</sub> laser," *Opt. Lett.* **27**, 436-438 (2002).
2. M. Hildebrandt, U. Bünting, U. Kosch, D. Haussmann, T. Levy, M. Krause, O. Müller, U. Bartuch, W. Viöl, "Diode-pumped Yb:KYW thin-disk laser operation with wavelength tuning to small quantum defects," *Opt. Commun.* **259**, 796-798 (2006).
3. M. Hildebrandt, M. Frede, P. Kwee, B. Willke, D. Kracht, "Single-frequency master-oscillator photonic crystal fiber amplifier with 148 W output power," *Opt. Express* **14**, 11071-11076 (2006).
4. M. Hildebrandt, M. Frede, D. Kracht, "Single-frequency Yb:YAG non-planar ring oscillator fiber amplifier source at 1030 nm," *Opt. Commun.* **273**, 260-262 (2007).
5. M. Hildebrandt, M. Frede, D. Kracht, "Narrow-linewidth ytterbium-doped fiber amplifier system with 45 nm tuning range and 133 W of output power," *Opt. Lett.* **32**, 2345-2347 (2007).
6. M. Hildebrandt, S. Büsche, P. Weßels, M. Frede, D. Kracht, "Brillouin scattering spectra in high-power single-frequency fiber amplifiers," *Opt. Express* **16**, 15970-15979 (2008).

## Conference contributions

1. M. J. Lederer, M. Hildebrandt, V. Z. Kolev, B. Luther-Davies, B. Taylor, J. Dawes, P. Dekker, J. Piper, H. H. Tan, C. Jagadish, "Diode-pumped femtosecond Yb:YAl<sub>3</sub>(BO<sub>3</sub>)<sub>4</sub> laser passively mode-locked by an ion-implanted SESAM," Proc. CLEO **1**, 344-345 (Long Beach, 2002).
2. M. J. Lederer, M. Hildebrandt, V. Z. Kolev, B. Luther-Davies, B. Taylor, J. Dawes, P. Dekker, J. Piper, H. H. Tan, C. Jagadish, "Passively mode-locked, self-frequency doubled, diode-pumped Yb:YAl<sub>3</sub>(BO<sub>3</sub>)<sub>4</sub> laser," Proc. Ultrafast Phenomena **71**, 158-160 (Vancouver, 2002).
3. M. Hildebrandt, M. Frede, D. Kracht, I. Freitag, P. Weßels, "Single-frequency fiber amplifier emitting 7.8 W at 1030 nm," Proc. ASSP, MB6 (Incline Village, 2006).
4. M. Hildebrandt, M. Frede, R. Wilhelm, P. Kwee, B. Willke, D. Kracht, "Single-frequency photonic crystal fiber amplifier with 148-W output power," Proc. SPIE **6453**, 64531J-1 (San Jose, 2007).
5. M. Hildebrandt, M. Frede, D. Kracht, "Tunable Single-Frequency External-Cavity Diode Laser Ytterbium-Doped Fiber Amplifier System," Proc. ASSP, ME6 (Vancouver, 2007).
6. S. Büsche, M. Hildebrandt, M. Frede, D. Kracht, "Messung von Emissionsspektren der Brillouin Streuung in Ytterbium dotierten einfrequenzen Faserverstärkern mit 130 W Ausgangsleistung," Verhandlungen der DPG, Q13.5 (Darmstadt, 2008).
7. M. Hildebrandt, S. Büsche, P. Weßels, M. Frede, D. Kracht, "Evolution of SBS gain spectra in high-power single-frequency ytterbium doped fiber amplifiers," Proc. CLEO, CTuB1 (San Jose, 2008).
8. M. Hildebrandt, M. Frede, B. Schulz, D. Kracht, "Lasers for the axion-like particle search," Proc. 4<sup>th</sup> Patras Workshop (Hamburg, 2008).
9. G. Herink, S. Büsche, T. Theeg, M. Hildebrandt, M. Frede, J. Neumann, D. Kracht, "Faserverstärker mit arbiträren und festen Pulsformen im ns- und ps-Bereich," Verhandlungen der DPG, Q12.4 (Hamburg, 2009).

- 
10. T. Meier, K. Danzmann, K. Ehret, M. Frede, M. Hildebrandt, S. Ghazaryan, A. Knabbe, A. Lindner, J. List, N. Meyer, D. Notz, J. Redondo, A. Ringwald, G. Wiedemann, B. Willke, "Resonant light power buildup in ALPS, a "Light shining through a wall"-experiment," Verhandlungen der DPG, T74.5 (München, 2009).
  11. M. Hildebrandt, S. Büsche, P. Wessels, M. Frede, J. Neumann, D. Kracht, "Detection and simulation of thermally induced deformation of Brillouin scattering spectra in a high-power PCF amplifier," Proc. CLEO Europe, CJ1.4 (München, 2009).





# Curriculum Vitae

## Personal data

---

Name: Matthias Hildebrandt  
Date of birth: 19.05.1977  
Place of birth: Hannover, Germany  
Nationality: German  
Marital status: Single

## Education

---

1983 – 1987 Grundschule Steinhude  
1987 – 1989 Orientierungsstufe Steinhude  
1989 – 1994 Hölty-Gymnasium Wunstorf  
1994 – 1997 Wilhelm-Busch Gymnasium Stadthagen  
06/1997 Abitur

## Community service

---

09/1997 – 08/1998 Working with old and extremely handicapped people

## University education

---

1998 – 2002 Applied Laser Technologies at the University of Emden  
09/2000 – 01/2001 University of Hull, England  
03/2001 – 07/2001 Laser Physics Center in Canberra, Australia  
07/10/2002 Diplom Ingenieur (FH) Angewandte Lasertechnik  
“Diodengepumpte Ultrakurzpuls laser auf Festkörperbasis”  
08/2002 – 03/2003 Physics at University of Hannover  
04/2003 – 07/2005 University of Applied Sciences and Arts Göttingen  
06/07/2005 Master of Science in Optical Engineering  
“Yb:KYW Scheibenlaser mit Durchstimmung der Wellenlänge  
zu geringen Quantendefekten”

## Work experience

---

04/2002 – 10/2002 Diploma thesis employee at Highqlaser GmbH, Austria  
04/2004 – 06/2005 Master thesis employee at Vision Lasertechnik GmbH, Göxe  
since 08/2005 Scientific employee at Laser Zentrum Hannover e. V.



# Danksagung

Hiermit möchte ich allen Personen danken, die zum Entstehen und Gelingen dieser Arbeit beigetragen haben.

Meinem Doktorvater, Prof. Uwe Morgner, für die Betreuung und Unterstützung dieser Promotion. Prof. Boris Chichkov und Dr. Benno Willke danke ich für Ihre Bereitschaft zur Begutachtung dieser Arbeit und der Disputation. Für die Ermöglichung und Betreuung meiner Promotion am Laser Zentrum Hannover gilt mein besonderer Dank Dr. Dietmar Kracht und Dr. Maik Frede.

Allen Mitarbeitern der Abteilung Laserentwicklung möchte ich für die große Hilfsbereitschaft und das freundschaftliche Klima, auch neben der Arbeit, herzlich danken.

Meinen Eltern, Margit und Bernd Hildebrandt, meinem Bruder Daniel und meiner Freundin Petra danke ich für ihre große Unterstützung.

Für das Korrekturlesen dieser Arbeit möchte ich mich bei Prof. Uwe Morgner, Dr. Maik Frede und Dr. Dietmar Kracht herzlich bedanken.